



UNIVERSITÄT  
BAYREUTH

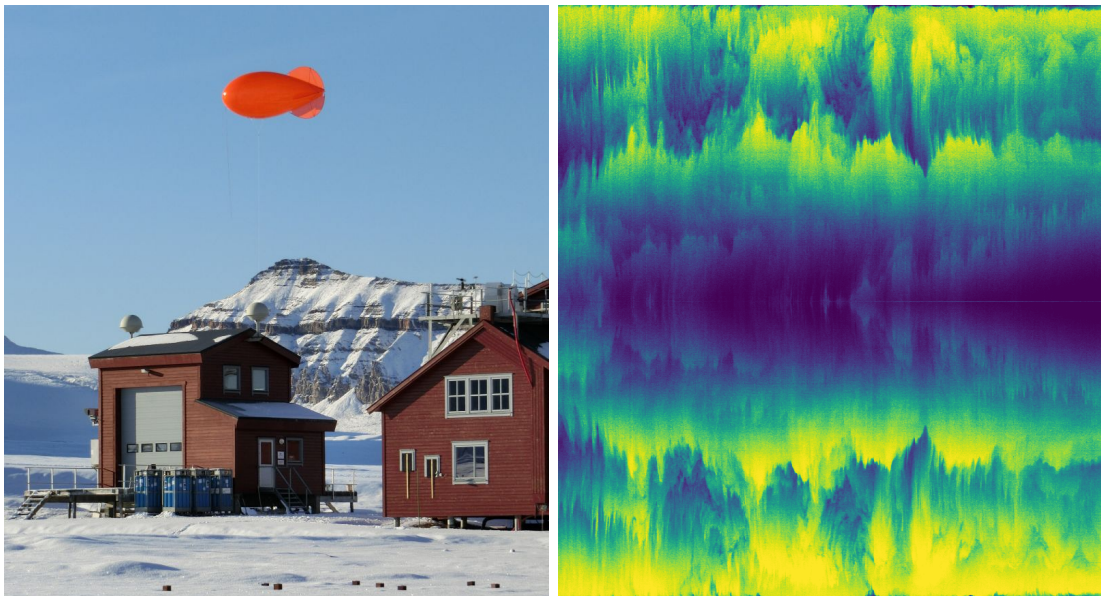
Faculty of Biology, Chemistry and  
Earth Sciences  
Micrometeorology group  
Prof. Dr. Christoph Thomas



---

# Vertical structure of the lower polar troposphere observed in temperature and wind profiles from fiber-optic distributed sensing on a tethered balloon over Ny-Ålesund, Svalbard, the Arctic

---



Master Thesis in Geoecology

**Tobias Linhardt**

Enrollment number: 1345269

February 24, 2021

supervised by:

Prof. Dr. Christoph Thomas

Dr. Wolfgang Babel



## Abstract

Global atmospheric circulation models suffer from large uncertainties under stable conditions in the lower troposphere, which are particularly abundant in the Arctic. Atmospheric dynamics and thermodynamics under such conditions must be understood in detail to improve model parameterizations. Lifted temperature inversions, generated via subsidence, advection or topographically altered flow, are a ubiquitous feature in the lower Arctic troposphere. This thesis aimed at quantifying the variability of dynamics and thermodynamics in the stably-stratified lower troposphere under weak-wind conditions in an area with strong topography and surface heterogeneity. Thereby, forcings and characteristics of observed lifted inversions were studied. Further, the response of the surface-based inversion to variability of airflow at the surface was investigated.

Temperature and wind profiles were recorded *in situ* in Ny-Ålesund, Svalbard, between the surface and up to 800 m elevation, at an unprecedented resolution of  $10^1$  s and  $10^0$  m. These measurements were taken on 6 days in September 2018 with a novel fiber-optic distributed sensing method, where fiber-optic cables were lifted by a tethered balloon. An algorithm based on local static stability was developed and applied to detect lifted inversions and the less stable layers they separated. Thermodynamic profiles were analyzed via multiresolution decomposition, including a vertical length scale of horizontal motions.

Temperature and wind speed variability within the surface-based inversion responded strongly to variations in airflow. Peak temperature variability across fiber-optic profiles was found in the surface-based inversion, which was caused by events of cold-air drainage. Despite distinct stratification, local events of subcritical Richardson numbers in the lowermost 100 m indicated intermittent turbulence generation. Multiple lifted inversions were abundantly observed with typical thickness between 10 m and 100 m and duration of up to several hours. Lifted inversions showed strong wave-like vertical oscillations of up to 200 m within few minutes, which were the main cause of temperature variability in the profiles above the surface inversion. Vertical oscillations of lifted inversions occurred at scales of potential internal gravity waves. Cascade turbulence was indicated in temporal spectra throughout the profile. This turbulence was strongest with occurrence of lifted inversions, where maximum turbulent time scales corresponded to time scales of oscillations of lifted inversions. Deep, long-lived lifted inversions occurred most frequently at weak winds and significant radiative energy loss at the surface. This points to a regional radiative generation of lifted inversions in combination with the mountainous topography influencing local airflow, while no connection of the observed lifted inversions to synoptic subsidence or advection was found.

The presented measurements reveal the fine-scale space–time structure of the lower Arctic troposphere in unprecedented detail and constitute a groundbreaking advance in atmospheric observations. The findings highlight the dominant role of shallow lifted inversions in governing thermodynamic structure and its variability in the lower troposphere in Arctic regions with strong topography.

## Zusammenfassung

Globale atmosphärische Zirkulationsmodelle zeigen große Unsicherheiten unter stabilen Bedingungen in der unteren Troposphäre, welche in der Arktis sehr häufig sind. Ein detailliertes Verständnis der Dynamik und Thermodynamik der Atmosphäre unter solchen Bedingungen ist erforderlich, um Modellparametrisierungen zu verbessern. Gehobene Temperaturinversionen, die unter Einfluss von Advektion, Subsidenz oder topographisch beeinflussten Luftströmungen entstehen, sind ein allgegenwärtiges Phänomen in der unteren arktischen Troposphäre. Diese Masterarbeit beinhaltet eine Quantifizierung der Variabilität von Dynamik und Thermodynamik in der stabil geschichteten unteren Troposphäre unter Schwachwindbedingungen in einem Gebiet mit starkem Relief und hoher Oberflächenheterogenität. Die Eigenschaften und bestimmenden Mechanismen von beobachteten gehobenen Inversionen wurden dabei erforscht. Darüber hinaus wurde die Auswirkung der Variabilität von bodennahen Luftströmungen auf die Bodeninversion untersucht.

Temperatur- und Windprofile wurden *in situ* in Ny-Ålesund, Spitzbergen, zwischen der Oberfläche und 800 m Höhe mit einer nie dagewesenen Auflösung von  $10^1$  s und  $10^0$  m erfasst. Diese Messungen wurden an 6 Tagen im September 2018 mit einer neuartigen räumlich verteilten Glasfasermesstechnik durchgeführt, bei der Glasfaserkabel durch einen Fesselballon angehoben wurden. Ein auf lokaler statischer Stabilität basierender Algorithmus wurde entwickelt und verwendet um gehobene Inversionen und von diesen begrenzte weniger stabile Schichten zu detektieren. Thermodynamische Profile wurden mithilfe von *multiresolution decomposition* einschließlich einer vertikalen Längenskala horizontaler Luftbewegungen analysiert.

Die Variabilität von Temperatur und Windgeschwindigkeit innerhalb der Bodeninversion reagierte stark auf Veränderungen der Luftströmung. Maximale Temperaturvariabilität in den Glasfaserprofilen fand in der Bodeninversion statt, verursacht durch Kaltluftabflüsse. Trotz starker Schichtung wurden lokal subkritische Richardson-Zahlen in den unteren 100 m beobachtet, die intermittente Erzeugung von Turbulenz anzeigten. Mehrfache gehobene Inversionen wurden häufig beobachtet, mit Schichtdicken zwischen 10 m und 100 m und bis zu mehreren Stunden Dauer. Gehobene Inversionen zeigten starke wellenartige vertikale Oszillationen von bis zu 200 m innerhalb weniger Minuten, welche die Hauptursache von Temperaturvariabilität in den Profilen oberhalb der Bodeninversion waren. Vertikale Oszillationen von Bodeninversionen fanden auf Zeitskalen von möglichen internen Schwerewellen statt. Kaskadenturbulenz wurde in zeitlichen Spektren über die gesamten Profile hinweg gefunden. Diese Turbulenz war am stärksten mit Auftreten von gehobenen Inversionen. In diesem Fall entsprach die maximale turbulente Zeitskala der Zeitskala der Oszillationen der gehobenen Inversionen. Mächtige und langlebige gehobene Inversionen waren am häufigsten bei Schwachwind und signifikantem strahlungsgetriebenem Energieverlust an der Oberfläche. Dies deutet auf eine regionale strahlungsbedingte Entstehung der gehobenen Inversionen in Kombination mit dem Einfluss der gebirgigen Topographie auf lokale Luftströmungen hin, während kein Zusammenhang zwischen gehobenen Inversionen und synoptischer Subsidenz oder Advektion gefun-

den wurde.

Die vorgestellten Messungen erfassen die kleinskalige Raum-Zeit-Struktur der unteren arktischen Troposphäre in ungekannter Detailgenauigkeit und stellen einen bahnbrechenden Fortschritt in atmosphärischen Beobachtungen dar. Die gewonnenen Erkenntnisse verdeutlichen die dominierende Rolle, die geringmächtige gehobene Inversionen bei der Bestimmung der thermodynamischen Struktur und deren Variabilität in der unteren Troposphäre in arktischen Regionen mit starkem Relief einnehmen.

# Contents

<b>Abstract</b>	<b>I</b>
<b>Zusammenfassung</b>	<b>II</b>
<b>List of Figures</b>	<b>VI</b>
<b>List of Tables</b>	<b>VIII</b>
<b>List of Abbreviations</b>	<b>IX</b>
<b>1. Introduction</b>	<b>1</b>
1.1. Objectives and hypotheses . . . . .	4
<b>2. Materials and methods</b>	<b>6</b>
2.1. Site description . . . . .	6
2.2. Fiber-optic distributed sensing . . . . .	7
2.2.1. Field deployments . . . . .	8
2.2.2. Calibration . . . . .	11
2.2.3. Determining measurement heights . . . . .	13
2.2.4. Calculating meteorological parameters . . . . .	14
2.3. Ancillary observational systems . . . . .	18
2.4. Detecting sublayers and surface-based inversions . . . . .	19
2.5. Multiresolution decomposition of virtual potential temperatures . . . . .	21
2.5.1. MRD in space and time with one window for entire experiments . . . . .	21
2.5.2. MRD in time with several windows for entire experiments . . . . .	22
2.5.3. MRD in space and time with one window for detected sublayers . . . . .	22
<b>3. Results and discussion</b>	<b>25</b>
3.1. Atmospheric conditions inferred from traditional measurements and models . . . . .	25
3.1.1. Conditions across the measurement campaign . . . . .	25
3.1.2. Synoptic forcing of conditions during fiber-optic experiments . . . . .	29
3.1.3. Conditions during fiber-optic experiments . . . . .	32
3.2. Overview of thermodynamic structure in fiber-optic profiles . . . . .	35
3.3. Detected sublayers and surface-based inversions . . . . .	37
3.4. Variability of the surface-based inversion . . . . .	41
3.4.1. Overview of dynamics . . . . .	42
3.4.2. Influence of wind directions on thermodynamics . . . . .	44
3.4.3. Exemplary course of dynamics on September 21 . . . . .	48
3.5. Phenomena in thermodynamic profiles above the surface-based inversion . . . . .	48
3.5.1. Oscillations of lifted inversions . . . . .	48
3.5.2. Neutral stability events in non-inversion layers . . . . .	50
3.6. Scales observed in fiber-optic profiles of thermodynamics . . . . .	51
3.6.1. Spatial scales in thermodynamic profiles . . . . .	51
3.6.2. Temporal scales in thermodynamic profiles . . . . .	53

3.6.3. Spatial and temporal scales in thermodynamics of sublayers . . . . .	56
3.6.4. Vertical length scales and coupling of horizontal motions . . . . .	58
3.7. Response of the surface-based inversion to varying airflow . . . . .	62
3.8. Conditions influencing lifted inversions and their variability . . . . .	63
3.9. Implications for research on lower Arctic troposphere . . . . .	65
3.10. Implications for future research, lessons learned . . . . .	66
<b>4. Conclusion</b>	<b>69</b>
<b>Acknowledgements</b>	<b>72</b>
<b>References</b>	<b>73</b>
<b>Appendices</b>	<b>80</b>
<b>A. Fiber-optic distributed sensing</b>	<b>80</b>
<b>B. Detecting sublayers</b>	<b>86</b>
<b>C. Multiresolution decomposition</b>	<b>90</b>
<b>D. Additional results</b>	<b>96</b>
<b>Declaration of Authorship</b>	<b>108</b>

## List of Figures

2.1.	Overview map . . . . .	6
2.2.	Data availability . . . . .	8
2.3.	FODS setups used during the campaign . . . . .	9
2.4.	Documentation footage of the fiber-optic setups . . . . .	10
2.5.	Differently calculated measures of thermodynamic structure in fiber-optic profiles	16
2.6.	Illustration of the computation of local static stability . . . . .	16
2.7.	Documentation footage of the SODAR installation . . . . .	19
3.1.	Overview of surface-based atmospheric measurements . . . . .	26
3.2.	Time series of SODAR wind measurements . . . . .	27
3.3.	Wind roses showing synoptic forcing for fiber-optic experiments at 10 m agl . .	28
3.4.	Bulk Richardson number roses showing synoptic forcing for fiber-optic experi- ments at 10 m agl . . . . .	29
3.5.	Geopotential heights at 850 hPa level from NCEP/NCAR reanalysis . . . . .	31
3.6.	Wind roses over the duration of fiber-optic experiments at 10 m agl . . . . .	32
3.7.	Horizontal wind statistics from SODAR for experiment periods in the lowest 250 m agl . . . . .	33
3.8.	Friction velocity roses over the duration of fiber-optic experiments at the EC system . . . . .	34
3.9.	Sensible heat flux roses over the duration of fiber-optic experiments at the EC system . . . . .	35
3.10.	Temporal statistics of virtual potential temperatures from fiber-optic experiments	36
3.11.	Temporal statistics of virtual potential temperatures from 180913 experiment .	37
3.12.	Duration and thickness of detected sublayers . . . . .	39
3.13.	Scatter plots of bulk sublayer characteristics . . . . .	41
3.14.	Temporal statistics of virtual potential temperatures, wind speeds and Richard- son numbers from fiber-optic experiments . . . . .	42
3.15.	Occurrence of subcritical Richardson numbers during 180921 . . . . .	43
3.16.	Rose plots of standard deviation of virtual potential temperature in the SI over the duration of fiber-optic experiments . . . . .	45
3.17.	Instantaneous profiles of fiber-optic temperatures and wind speeds for 3 hours of 180921 . . . . .	46
3.18.	Temporal statistics of virtual potential temperatures, wind speeds and Richard- son numbers from 180921 experiment . . . . .	47
3.19.	Oscillations of inversions layers for selected fiber-optic data . . . . .	49
3.20.	Exemplary instantaneous profiles of virtual potential temperature . . . . .	50
3.21.	Spatial MRD spectra of virtual potential temperatures from fiber-optic experi- ments in static stability classes . . . . .	52
3.22.	Temporal MRD spectra of virtual potential temperatures from fiber-optic ex- periments in height classes . . . . .	54
3.23.	Spectra of MRD of virtual potential temperatures in space and time from fiber- optic experiments for detected sublayers . . . . .	57
3.24.	Probability density of inverse Brunt-Väisälä frequency . . . . .	58

3.25.	Vertical length scales of motions . . . . .	59
A.1.	Differences in fiber temperatures between ascending and descending branch of profile . . . . .	80
A.2.	Estimating step losses of Raman backscatter . . . . .	80
A.3.	Correcting the resistance thermometer temperatures . . . . .	81
A.4.	Removing fiber holder artifacts in the fiber temperatures . . . . .	82
A.5.	Defining the start, top and end of the fiber section within the atmospheric profile . . . . .	82
A.6.	FFT spectrum of tether sonde pressure . . . . .	83
A.7.	Defining the relationship between distance along fiber from ground of FireFOX and IceFOX via temporal correlations of fiber temperatures . . . . .	84
A.8.	Spatial MRD spectra of fiber temperatures for neutral stability . . . . .	85
B.1.	Sublayer detection, step 1: Spatial merging . . . . .	86
B.2.	Sublayer detection, step 2: Temporal merging . . . . .	87
B.3.	Sublayer detection, step 3: Removing short-lived layers . . . . .	87
B.4.	Sublayer detection, step 4: Final merging of layers in space and time . . . . .	88
B.5.	Sublayer detection, step 5: Renaming final layers . . . . .	88
B.6.	Histogram of local static stability . . . . .	89
C.1.	Exemplary multiresolution decomposition of an artificial time series . . . . .	90
C.2.	Variance spectrum of a multiresolution decomposition of an artificial data series . . . . .	91
C.3.	Example for calculation of vertical scales of motions via correlation decay . . . . .	92
C.4.	Subsampling sublayers for MRD calculation, step 1 . . . . .	93
C.5.	Subsampling sublayers for MRD calculation, step 2 . . . . .	93
C.6.	Subsampling sublayers for MRD calculation, step 3 . . . . .	94
C.7.	Subsampling sublayers for MRD calculation, results for 180913 . . . . .	94
C.8.	Padding approach for MRD in space on sublayers . . . . .	95
D.1.	Defining strong-wind and weak-wind regimes . . . . .	96
D.2.	Wind roses of surface-based recordings . . . . .	97
D.3.	Horizontal wind statistics from SODAR recordings . . . . .	97
D.4.	Instantaneous profiles of fiber-optic temperatures and wind speeds for 180916 . . . . .	98
D.5.	Instantaneous profiles of fiber-optic temperatures and wind speeds for 180918 . . . . .	99
D.6.	Instantaneous profiles of fiber-optic temperatures and wind speeds for 180921 . . . . .	100
D.7.	Instantaneous profiles of fiber-optic temperatures for 180910 . . . . .	101
D.8.	Instantaneous profiles of fiber-optic temperatures for 180911 . . . . .	102
D.9.	Instantaneous profiles of fiber-optic temperatures and SODAR wind for 180913 . . . . .	103
D.10.	Instantaneous profiles of fiber-optic temperatures and SODAR wind for 180916 . . . . .	104
D.11.	Instantaneous profiles of fiber-optic temperatures and SODAR wind for 180918 . . . . .	105
D.12.	Instantaneous profiles of fiber-optic temperatures and SODAR wind for 180921 . . . . .	106
D.13.	Wind profiles from radiosoundings during fiber-optic experiments . . . . .	107

## List of Tables

2.1.	Set and corrected heating rates of the heat pulse unit . . . . .	18
3.1.	NCEP/NCAR reanalysis data at 850 hPa level . . . . .	30
3.2.	Bulk statistics of sublayer detection . . . . .	38
A.1.	Parameters used for step loss correction . . . . .	81
A.2.	Manually defined relationships between distance along fiber from ground of Fire- FOX and IceFOX . . . . .	83

## List of Abbreviations

Abbreviation	Unit	Explanation
180910		IceFOX on September 10, 2018
180911		IceFOX on September 11, 2018
180913		IceFOX on September 13, 2018
180916		FireFOX on September 16, 2018
180918		Combined IceFOX and FireFOX on September 18, 2018
180921		Combined IceFOX and FireFOX on September 21, 2018
ABL		Atmospheric boundary layer
af		along fiber
agl		above ground level
asl		above sea level
AWIPEV		Shared research station of French and German polar institutes in Ny-Ålesund
BLR		Boundary layer regime; defined by flow and dynamic stability at the surface
BSRN		Baseline surface radiation network; radiation monitoring, here referring to Ny-Ålesund station
$C$	-	Calibration parameter of DTS instrument
EC		Eddy Covariance
$d_f$	m af	Distance from ground along fiber
$d_{tf}$	m	Distance between top of fiber and tethersonde
$D^2, D_{\theta_v}^2$	-, $K^2$	Power of MRD variance spectra
DTS		Distributed temperature sensing
$e$	-	Eulerian number
$E$	hPa	vapor pressure of air
FireFOX		FLYFOX setup with parallel unheated and heated fibers for recording wind speed profiles
FLYFOX		FLYing Fiber-Optic eXperiment; fibers are lifted by a tethered balloon
FLYFOX-A		FLYFOX in the Arctic, name of campaign presented in this thesis
FODS		Fiber-optic distributed sensing
$h$	m agl	Height above ground level
$h_f$	m agl	Height of fiber
$h_{SI}$	m agl	Height of the surface-based inversion
$h_{ts}$	m agl	Height of tethersonde
HPU		Heat pulse unit (for heating the fibers)
$I_{\downarrow}, I_{\uparrow}$	$W m^{-2}$	Atmospheric and terrestrial longwave radiation, respectively
IceFOX		FLYFOX setup with two parallel unheated fibers for recording temperature profiles
IL		Inversion layer, yielded by the layer detection algorithm
$K_{\downarrow}, K_{\uparrow}$	$W m^{-2}$	Global radiation and reflected shortwave radiation, respectively

Abbreviation	Unit	Explanation
$L_b$	m	Length of vertical blocks for $LSS$ calculation
$LD$	s	Layer duration
$l_f$	m af	Length of a fiber branch
LI		Lifted (temperature) inversion
LIDAR		Light detection and ranging
$LSS$	$K m^{-1}$	Local static stability, calculated from block differences
LTR		Lower troposphere regime; defined by thermal structure and dynamics
$L_v$	m	Vertical length scale of horizontal structures, estimated via correlation decay of $\theta_v$ between measurement bins, for MRD modes
$m$	-	MRD mode
$M$	-	Highest MRD mode
$n_{IL}$	-	Mean number of ILs in the column in instantaneous profiles
NIL		Non-inversion layer, yielded by the layer detection algorithm
MRD		Multiresolution decomposition
MOST		Monin-Obukhov similarity theory
NCEP/NCAR reanalysis		Global reanalysis data set by the National Center for Environmental Prediction and the National Center for Atmospheric Research
$N_{BV}$	$s^{-1}$	Brunt-Väisälä frequency
NOAA		National Oceanic and Atmospheric Administration
NSE		Neutral stability event
$p$	hPa	air pressure
$P_S, P_{As}$	W	Power of Raman Stokes and Antistokes, respectively
$Q_H$	$W m^{-2}$	Turbulent sensible heat flux
$Q_E$	$W m^{-2}$	Turbulent latent heat flux
$Q_S^*$	$W m^{-2}$	Net radiation
RADAR		Radio detection and ranging
$R$	-	Pearson correlation coefficient
$Ri$	-	Simplified gradient Richardson number
$Ri_b$	-	Bulk Richardson number
SBL		Stable boundary layer (surface-based)
SI		Surface-based (temperature) inversion
SODAR		Sound detection and ranging
SS		Stainless steel, used for coating of the actively heated fibers
$S$		Sample of sublayer for MRD; subscript letters: d=dyadic, s=spatial, t=temporal
$t$	s	time
$T_f, T_{f,a}, T_{f,d}$	K	Fiber temperature; for ascending and descending fiber branch, respectively
$t_{IGW}$	s	Minimum event scale (half period length) of internal gravity waves
$T_w, T_c$	$^{\circ}C$	Reference temperatures from resistance thermometers in warm and cold baths, respectively

Abbreviation	Unit	Explanation
$U$	$\text{m s}^{-1}$	Horizontal wind speed
$u$	$\text{m s}^{-1}$	Zonal wind speed
$u_*$	$\text{m s}^{-1}$	Friction velocity
$v$	$\text{m s}^{-1}$	Meridional wind speed
$x_I$	-	Ratio of temperature inversions in the data
$x_{I,h}$	-	Ratio of temperature inversions at a measurement height in time
$x_{I,t}$	-	Ratio of temperature inversions in an instantaneous atmospheric profile
$x_{IL}$	-	Ratio of inversion layers in the data
$x_{I,IL}, x_{NI,NIL}$	-	Ratio of inversion and non-inversion bins, respectively, that were integrated into the corresponding sublayer category by the layer detection
$x_{S,As}$	-	log ratio of power of Raman Stokes to Antistokes ( $\ln\left(\frac{P_S}{P_{As}}\right)$ )
$x_{SI}$	-	Ratio of profiles containing a surface-based inversion
$z$	m af	location along fiber
$\Delta\alpha$	$\text{m}^{-1}$	Differential attenuation of Raman Stokes and Antistokes
$\gamma$	K	energy shift between original photon and scattered Raman photon
$\Theta_v, \theta_v$	K, °C	Virtual potential air temperature; wavelet-filtered if not noted otherwise
$\sigma_{\theta_v,SI}$	K	$\sigma_{\theta_v}$ between surface and median $h_{SI}$
$\kappa_L$	-	Poisson constant
$\phi$	-	Time or space series MRD is performed on



---

## 1. Introduction

The correct implementation of the atmospheric boundary layer (ABL) in the Arctic into weather and climate models is crucial for global atmospheric modeling: Since stable boundary layers (SBLs) are insufficiently parameterized in large-scale atmospheric models (Hunt et al., 1996; Poulos and Burns, 2003), their frequent and widespread occurrence in the Arctic is a major cause of uncertainty in global circulation models (Holtstlag et al., 2013). Describing the lower Arctic troposphere is further complicated by the common presence of lifted temperature inversions (LIs) (Busch et al., 1982) which add complexity to the atmospheric structure.

For a better understanding of the processes in the lower Arctic troposphere, it is necessary to capture atmospheric thermodynamic and dynamic conditions at sufficient spatiotemporal resolution to explore the fine-scale structure and variability. This includes capturing typical time scales of dominating motions, particularly buoyancy-driven gravity waves, and resolving space scales of few meters, which are typical for small LIs and turbulent layers (Gossard et al., 1985; Muschinski and Wode, 1998). There are three currently established approaches for measuring the vertical structure of the ABL:

- (1) Towers enable measurements at manually defined spatial resolution close to the surface. High density of devices is costly though and towers rarely reach far above the surface layer.
- (2) Vertical *in-situ* profiling, e.g. via radiosondes, aircrafts or drones, provides snapshots of atmospheric profiles, but often suffers from high spatial uncertainty of several meters and cannot capture individual motions even at a high launching frequency because they follow varying trajectories inducing large spatial uncertainty.
- (3) Remote sensing via radio detection and ranging (RADAR), light detection and ranging (LIDAR) or sound detection and ranging (SODAR) enables the recording of spatially distributed time series. For SBL observations of the three-dimensional wind field, SODAR allows the highest resolutions at several minutes and several meters and the lowest altitudes of meaningful remote sensing data at 10 m to 20 m (Kallistratova et al., 2018). Combined with a radio antenna, a radio-acoustic sounding system (RASS) is created, which enables the additional recording of temperatures. At its highest resolution SODAR can display the thermal turbulence structure through the temperature structure parameter at scales down to 2 m and 1 s (Argentini et al., 2012). SODAR has therefore already been successfully used to measure mixing-layer height, surface-based and LIs, gravity waves, wave-breaking and thermal turbulence (e.g. Cheung, 1991; Emeis et al., 2004; Petenko et al., 2012, 2019; Lyulyukin et al., 2019; Viana et al., 2012). However, direct translation of acoustic backscatter to thermal structure of the atmosphere is complicated by the variability of echo strength at the SODAR site (Anderson, 2003).

None of the presented techniques is capable of recording continuous spatiotemporal profiles of temperatures or wind speeds in the lower troposphere, neither at vertical scale of small LIs, nor at time scales of small gravity waves. What is more, this can neither be achieved by combining the mentioned recording methods because of their varying time and space scales, leading to a persistent gap in spatiotemporal resolution of measurements in the lower atmosphere, and precluding the display of the fine-scale space-time structure of the ABL and the lower free atmosphere. Here, a novel method of recording high-resolution temperature and wind profiles in the lower troposphere, which uses fiber-optic distributed sensing and a tethered balloon, serves as a promising new approach to solve this dilemma. This method has already been successfully

employed by Keller et al. (2011). A similar setup using an unmanned aircraft instead of a tethered balloon was used to investigate the morning transition from SBL to convective boundary layer (Higgins et al., 2018). This distributed sensing method holds the potential to reveal the full fine-scale space–time structure of temperatures and winds in the lower atmosphere and enables tracking air motions in space and time.

Since radiative surface cooling is the dominating process generating SBLs (Mahrt, 2014), they are typically found during the night in lower latitudes. Classical theory divides the nocturnal ABL into SBL, residual layer and capping inversion (Stull, 1988). Here, the residual layer is the leftover of the convective layer from the previous day and will be incorporated into the newly developing convective layer of the following day if the capping inversion will become the entrainment zone. While typical ABL heights in the mid-latitudes range between 1 km and 2 km, SBL thickness may be less than 10 m under very stable conditions (Smedman, 1988).

The classical conceptualization of diurnal variability of the ABL with a nocturnal SBL can not generally be applied to Arctic regions where SBLs may last for more than one diurnal cycle. These so-called long-lived SBLs can exist for months or the entire duration of the polar night, precluding the existence of residual layer and capping inversion as parts of the ABL. Even in very long-lived SBLs however, there are still frequent changes in the boundary layer regimes (Baas et al., 2019). The surface-based inversion (SI) can even be frequently eroded in mid-winter (Kahl, 1990). Under very stable conditions the entire boundary layer can be restricted to the lowest meters or tens of meters of the atmosphere, without any definable residual layer above. Long-lived SBLs, observed as surface-based temperature inversions, are most common in winter when they are predominantly caused by radiative energy loss from the surface (Busch et al., 1982).

Above the SBL, LIs are typically found in the free Arctic troposphere with maximum occurrence around summer and significant abundance in spring and autumn (Serreze et al., 1992; Wetzal and Brümmer, 2011). Due to observational restrictions, these LIs are commonly defined with a minimum depth of 100 m (Kahl, 1990). However, far thinner inversions are abundantly observed with remote sensing. High-resolution aircraft data showed that they can even exist on a submeter scale (Muschinski and Wode, 1998). Main processes causing LIs are large-scale subsidence or heat advection, with both processes often forcing the formation of accompanying clouds (Busch et al., 1982; Wetzal and Brümmer, 2011). Topography can also act as a generation mechanism for LIs via katabatic winds (Emeis et al., 2007; Vihma et al., 2011). LIs have been observed in the lower arctic troposphere under very stable surface conditions over flat (Cheung, 1991; Anderson, 2003) and mountainous (Vihma et al., 2011; Maturilli and Kayser, 2017) terrain and sea ice (Palo et al., 2017). In areas with distinct relief, multiple LIs were also found at lower latitudes (Emeis et al., 2007). Radiosoundings confirmed the existence of LIs in the entire troposphere and above (Dalaudier et al., 1994). This fine-scale structure of the lower Arctic troposphere additionally shows considerable temporal variability which is likely due to horizontal advection of a spatially heterogeneous atmospheric structure (Anderson, 2003).

Motions in the stably-stratified atmosphere have been most exhaustively studied for the surface layer. In this lowest part of the ABL turbulent transport is commonly described by Monin-Obukhov similarity theory (MOST, Monin and Obukhov, 1954) which accounts for the effects of variations in dynamic stability. The theory builds on Kolmogorov similarity theory which states that turbulent energy cascades from larger to smaller scales down to energy dissipation. MOST correctly parameterizes turbulence in a weakly stable boundary layer which occurs with

---

substantial airflow or cloud cover and shows a relatively prototypical structure with continuous turbulence decreasing with height; however, within the very stable boundary layer, which occurs at low wind speeds and strong stratification, coupling becomes weak and intermittent and does not follow similarity theory (Grachev et al., 2005; Galperin et al., 2007; Mahrt, 2014). Weakly and very stable conditions can thus be distinguished by a critical Richardson number marking the collapse of Kolmogorov turbulence, which is defined between 0.2 and 0.25 (Miles, 1961; Howard, 1961; Grachev et al., 2013). Subcritical Richardson numbers can be found even under very stable conditions though, due to the large spatial heterogeneity in a SBL (Mahrt, 1987). Other authors have proposed a minimum wind speed threshold for sustaining continuous turbulence (Sun et al., 2012; van de Wiel et al., 2012). However, there are many ways to categorize SBL regimes, each more or less simplifying true conditions (Mahrt, 2014). Turbulence can be defined as intermittent if it varies distinctly across time or space; in the very stable boundary layer this typically means dominant very weak turbulence and occasional formation of distinct turbulence (Mahrt, 2014). These mixing events with significant turbulence can be generated by mechanisms such as gravity waves (Fritts et al., 2009), spatial variability of turbulent quantities (Muschinski et al., 2004) and downward transport of shear (Mahrt and Vickers, 2002). The latter is often caused by low-level jets, which are wind maxima often reaching supergeostrophic speeds that commonly form at the top of SBLs and separate them from the residual layer (e.g. Andreas et al., 2000). Gravity waves are produced by various processes, such as vertical displacement of horizontal flow by topography, convection or density currents, or are generated from shear instabilities (Sun et al., 2015).

Even in the seemingly quiescent periods between mixing events, finite turbulence prevails (Acevedo et al., 2007), which is intermittent and shows strong anisotropy with flat, pancake-like perturbations (Fritts et al., 2009). Weak turbulence under very stable conditions can persist within the lowermost decameters of the SBL (Petenko et al., 2019). This turbulence is at least partly generated by submeso-scale motions, which are defined as nonturbulent motions smaller than meso-gamma scale, i.e., 2 km which typically exhibit a pancake-like structure with small vertical scales (Mahrt et al., 2009, 2013; Mahrt, 2014; Vercauteren and Klein, 2015). They encompass various types, including wave-like structures such as small gravity waves (e.g. Sun et al., 2004), meandering motions or two-dimensional modes (Anfossi et al., 2005), microfronts, generated by drainage flows, and ramps (Belušić and Mahrt, 2012). Analyses of the spatial structure of submeso-scale and meso-scale motions have been focusing on horizontal scales and neglecting vertical scales due to technical restrictions (Belušić and Mahrt, 2008; Mahrt et al., 2009). Such studies have revealed that Taylor’s hypothesis of frozen turbulence, which assumes that temporal and space scales of motions are connected via the mean horizontal wind speed (Taylor, 1938), is invalid under stable conditions where horizontal space scales can strongly exceed the expected values (e.g. Mahrt et al., 2009; Thomas, 2011; Higgins et al., 2012; Cheng et al., 2017).

Above the ABL, airflow variability is strongly governed by gravity waves due to dominant stable conditions (Sun et al., 2015). Gravity waves can propagate horizontally along steep changes of density, i.e., LIs, or propagate vertically in a sufficiently thick stable layer (Stull, 1988). Horizontal propagation of gravity waves along LIs and other wavelike motions has been associated with the generation of observed turbulent layers of several meters depth adjacent to LIs (Gossard et al., 1985; Muschinski and Wode, 1998; Chimonas, 1999; Sun et al., 2015).

In this study, the spatiotemporal structure of the lower troposphere was investigated over Ny-

Ålesund, Svalbard, which is characterized by a complex mountainous topography around a fjord, and by a great variety of closely collocated surfaces, including inland ice and glaciers, snow-free and snow-covered sparsely vegetated soil, and open water surfaces of the fjord and the open sea. Turbulent and nonturbulent motions near the surface are considerably impacted by properties of the underlying surface, such as roughness, heat transfer, evapotranspiration and topography (Stull, 1988). Consequently, the pronounced surface heterogeneity causes large differences in ABL characteristics: The surface layer above fjord surfaces is mostly unstable throughout the year (Kilpeläinen and Sjöblom, 2010), while frequent katabatic winds from glaciers are associated with very stable stratification at the surface, especially with snow cover and little or no solar radiation (Jocher et al., 2012; Maturilli et al., 2013). Since Ny-Ålesund is surrounded by such heterogeneous surfaces, properties of the surface layer can vary substantially with wind direction, especially in winter, when the surface temperatures show the highest spatial variability. Channeling of mountain winds and land-sea breeze circulation along valleys and fjords generates very characteristic airflow conditions (Beine et al., 2001; Esau and Repina, 2012; Maturilli et al., 2013). The combined effect of these local and regional circulations in the complex landscape and large-scale advection and subsidence creates a typical multi-layered pattern above Ny-Ålesund, with LIs occurring within channeled flow and above (Vihma et al., 2011; Maturilli and Kayser, 2017).

### 1.1. Objectives and hypotheses

The overarching goal of this thesis was the characterization of the fine-scale space–time structure of the lower troposphere above Ny-Ålesund, Svalbard, with a focus on stable, weak-wind conditions. To this aim, temperature and wind profiles were recorded at unprecedentedly high resolution, using the earlier proposed combination of distributed fiber-optic sensing and tethered balloon, termed FLYFOX (FLYing Fiber-Optic eXperiment). The implementations in Ny-Ålesund were named FLYFOX-A, where A stands for Arctic. The data gained in the FLYFOX-A campaign were utilized to answer the following research questions:

- The vertical structure of the atmosphere was investigated for the presence of SIs and LIs separating sublayers with weakly stable to near-neutral conditions. Here, a multi-layered atmospheric structure was expected to be frequently found.
- Variability in thermodynamic profiles was studied across spatial and temporal scales. SIs and LIs likely dominated thermodynamic variability, specifically on scales of potential gravity waves.
- The response of the SI to variability in airflow and footprints was examined, where the heterogeneous landscape and topography surrounding Ny-Ålesund was anticipated to lead to distinct patterns in airflow, temperatures and fluxes, particularly associated with local katabatic winds.
- Atmospheric conditions impacting the presence and variability of LIs were investigated, where synoptic advection and subsidence, and regional radiative surface cooling combined with topographical effects were expected to be the governing processes. Meteorological

conditions at the surface were anticipated to show little or no connection to the occurrence and properties of LIs due to strong decoupling of the SI from the air above.

## 2. Materials and methods

### 2.1. Site description

All measurements referred to in this study were taken on the southern edge of Ny-Ålesund, Svalbard (village center at 78.9233 °N, 11.9208 °E), which has been a major center for Arctic research since 1966. Ny-Ålesund lies on the northern shore of Brøgger peninsula on Spitsbergen, the main island of the Svalbard archipelago. It is located between Kongsfjorden to the north and the mountains of Brøgger peninsula to the south which reach heights of more than 1000 m (Fig. 2.1). The site is characterized by Arctic tundra with very sparse vegetation and high abundance of glaciers. In the period between 1993 and 2011 temperatures ranged between -17.0 °C and -3.8 °C in January and 4.6 °C and 6.9 °C in July (Maturilli et al., 2013). The high latitude leads to long periods of polar night and polar day which last from October 24 to February 18, and April 18 to August 24, respectively (Maturilli et al., 2013). The measurement campaign analyzed in this thesis was carried out from September 10 to September 21, 2018, falling within the short transitional period of daily sunrise and sunset. September has been described as the Svalbard autumn (Westermann et al., 2009). During September temperatures fall significantly due to decreasing insolation, but snow cover typically does not persist before October (Maturilli et al., 2013). At the start of the campaign no snow cover was present around Ny-Ålesund. After snowfall on September 15, 2018, snow cover persisted until the end of measurements.

The local surface wind field in Ny-Ålesund is strongly affected by topography and surface

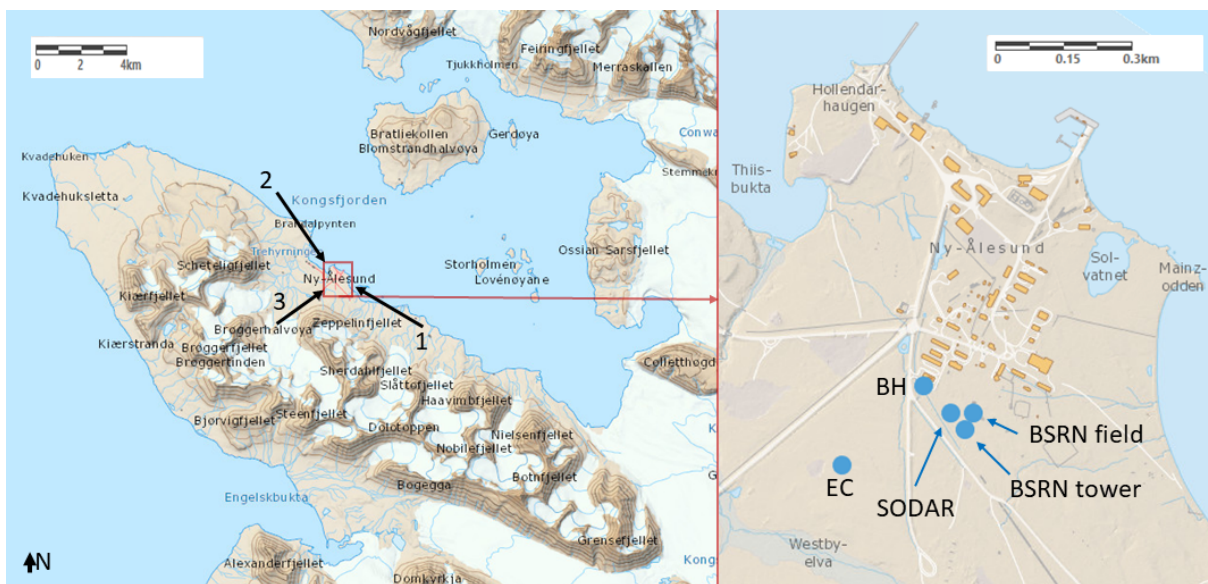


**Figure 2.1** Map of the Brøgger peninsula and Kongsfjorden on Spitsbergen, Svalbard. Dominant wind directions are denoted by black arrows with (1) channeled southeasterly winds from the inland ice, (2) channeled northwesterly winds from the ocean and (3) katabatic outflow from the Brøgger valley and glaciers. Research sites discussed in this thesis around Ny-Ålesund are shown in the inset map, including AWIPEV Balloon House (BH), Eddy Covariance station (EC), SODAR and Baseline Surface Radiation Network (BSRN). Topographic maps were taken from <https://svalbardkartet.npolar.no/> on October 16, 2020, as courtesy of the Norwegian Polar Institute.

heterogeneity, which leads to a high spatial variability of airflow, but also to channeling effects and katabatic flows associated with dominant wind directions (e.g. Beine et al., 2001; Argentini et al., 2003; Maturilli et al., 2013; Schulz, 2017): Channeling of airflow along Kongsfjorden occurs between the surface and 300 m agl to 500 m agl (Esau and Repina, 2012; Maturilli and Kayser, 2017), and leads to dominant easterly and southeasterly winds in Ny-Ålesund (see Fig. 2.1) throughout the year, with stronger winds than from any other direction. The dominance of east and southeast winds is caused by the combined effects of a land breeze from the mainland of Spitsbergen, and katabatic flow from the inland ice, particularly from Kongsvegen glacier 10 km to the east of Ny-Ålesund (Beine et al., 2001; Esau and Repina, 2012; Maturilli and Kayser, 2017). Being generated by horizontal pressure and temperature gradients, this land–sea breeze circulation is strengthened by the mountainous terrain in the area (Kilpeläinen et al., 2011). Increased force of southeast winds between September and May is caused by larger difference in surface temperatures between the snow- and ice-covered land and the open sea during these months. Between June and August, wind channeling commonly generates additional winds from north or northwest, i.e., from the open sea, due to a sea breeze caused by temperature differences between warmer land and cooler water in the snow-free season (Maturilli et al., 2013). Without strong synoptic forcing, katabatic outflow from the closely collocated Brøggerbreen glaciers induces southwesterly winds close to the surface outside of the snow-free season.

## 2.2. Fiber-optic distributed sensing

Fiber-optic distributed sensing (FODS) is an approach to recording physical parameters such as temperature and humidity along fiber-optic cables by means of sending laser pulses through the fiber-optic cables and recording the backscattered light (Thomas and Selker, 2021). The greatest advantages of FODS are the instantaneous *in-situ* measurement of physical parameters along fiber transects which can reach several kilometers in length, and the high resolution in time and space.

Raman backscattering of laser light can be used for distributed temperature sensing (DTS) along fiber-optic cables (Selker et al., 2006; Tyler et al., 2009). The DTS technique was introduced into atmospheric science by Thomas et al. (2012) who successfully used it to study small-scale structures in the surface layer. Sayde et al. (2015) found that DTS enables recording wind speed normal to fibers via the parallel installation of heated and unheated fibers. DTS has since been used in numerous publications within atmospheric sciences (e.g. Keller et al., 2011; Zeeman et al., 2015; Pfister et al., 2017; Sigmund et al., 2017; Pfister et al., 2019; Lapo et al., 2020).

The measurement principle of DTS is based on the dependence of Raman scattering on temperature: Inelastic Raman scattering generates scattered photons with lower or higher frequency than the incident photons which are referred to as Stokes and Anti-Stokes, respectively. The natural logarithm of the ratio of spectral power of Anti-Stokes  $P_{As}$  and of Stokes  $P_S$  is directly proportional to fiber temperature  $T_f$  at location along the fiber  $z$  and at time  $t$ :

$$T_f(z, t) \propto \ln \left( \frac{P_{As}(z, t)}{P_S(z, t)} \right). \quad (2.1)$$

$P_S$  and  $P_{As}$  are unequally extinguished due to their differing wavelengths as they propagate through the fiber. This effect is called differential attenuation, and is typically defined as a

fiber-specific extinction per length along fiber  $\Delta\alpha$  which is assumed to be constant for the entire fiber in implementations of DTS (e.g. Hausner et al., 2011). For the calculation of  $T_f$  from  $\ln\left(\frac{P_{As}(z,t)}{P_S(z,t)}\right)$  the value of  $\Delta\alpha$  is a crucial parameter, along with  $\gamma$  and  $C$ , which are parameters specific for the laser and sensor. These three parameters are therefore contained in the full calibration equation

$$T_f(z, t) = \frac{\gamma}{\ln\left(\frac{P_S(z,t)}{P_{As}(z,t)}\right) + C - \Delta\alpha z}. \quad (2.2)$$

Fiber temperatures  $T_f$  can be inferred after determining  $\Delta\alpha$ ,  $\gamma$  and  $C$  through a full matrix inversion of Eq. (2.2), which requires three calibration sections along the fiber where temperatures are known.

### 2.2.1. Field deployments

Fiber-optic cables were carried by a tethered balloon up to maximum heights between 100 m and 800 m, creating a recording sensor for atmospheric profiles at high spatial and temporal resolution. The tethered balloon (replica of *TTB series*, *Vaisala, Helsinki, Finland*) had a volume of 9 m<sup>3</sup> and a payload of 3 kg which could be lifted up to 1500 m asl. An electrical winch (*TTW111*, *Vaisala*) was used to release the tether. All flights were launched from the

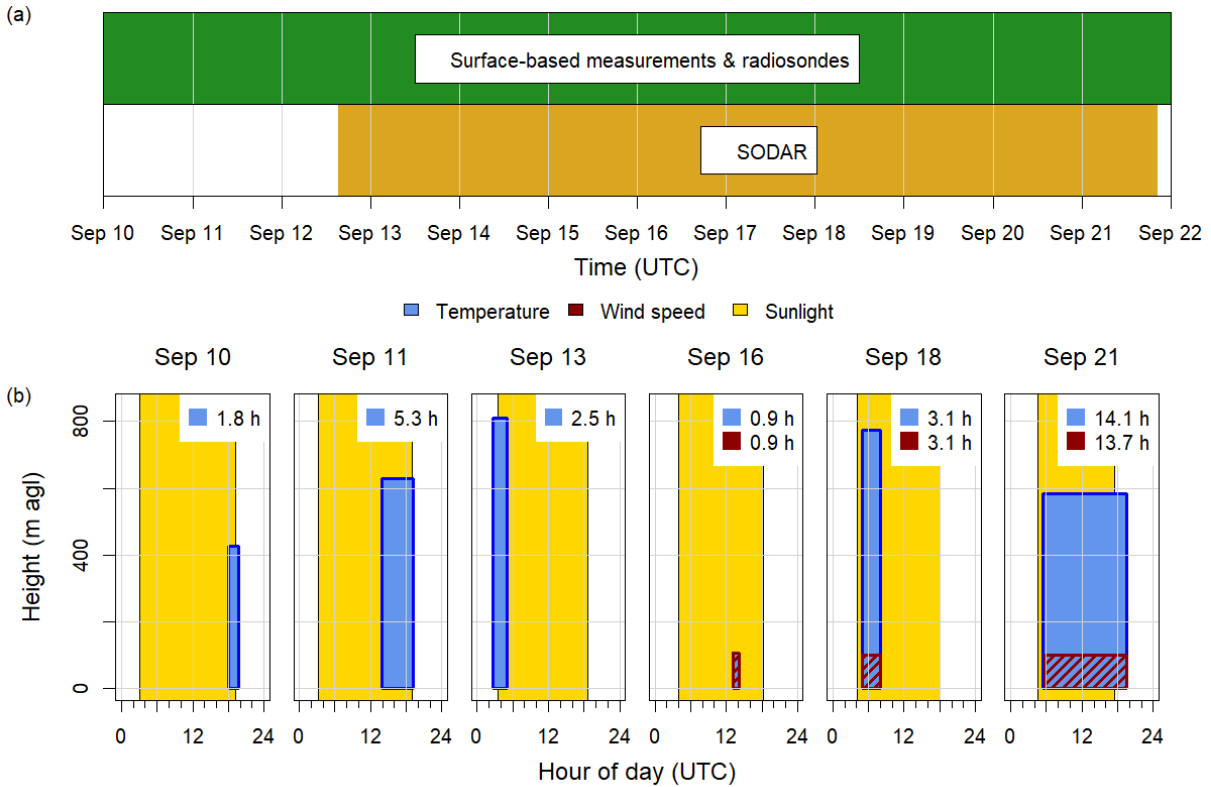


**Figure 2.2** (a) Data availability of reference measurements across the entire measurement period. (b) Spatial and temporal extent of FODS data for all six experiments, including duration (h) and presence of sunlight without sky view factor.

western platform of AWIPEV balloon house (78.92322 °N, 11.92317 °E, 15.7 m asl).

The DTS device used in the FLYFOX-A campaign (*XT-DTS, Silixa, Elstree, UK*) yielded a spatial sampling resolution of 0.25 m. This resulted in a physical resolution of 0.5 m, since neighboring bins along the fiber are not statistically independent from one another. Temporal resolution of the recorded data was 10 s or 20 s.

The experimental setup for measuring air temperatures was named IceFOX, for unheated fiber-optic experiment, while horizontal wind speeds along with air temperatures were measured with the FireFOX setup (heated fiber-optic experiment). The fiber-optic experiments were named after the date of their execution, e.g. 180910 for the experiment on September 10, 2018. IceFOX alone was deployed for 180910, 180911 and 180913, FireFOX alone for 180916, and a combination of both was used for 180918 and 180921 (Fig. 2.2). The implementation of varying setups across the campaign result from their consecutive development and trial. Since FLYFOX could only be launched at weak winds, sufficient daylight and without scheduled flights at the Ny-Ålesund airport, only six experiments with greatly varying flight duration were realized. Of these flights, 180913, 180918 and 180921 were deliberately started early in the day to capture very stable conditions.

For the IceFOX setup (Fig. 2.3a), individual cables contained a fiber-optic cable with a diameter of 50  $\mu\text{m}$  which was tightly-buffered in a PVC coating with outer diameter of 0.9 mm (*AFL, Duncan, SC, USA*). A twisted-pair cable was used, i.e., two individual cables were intertwined, where individual cable lengths were approximately 1 km. Both fiber-optic cables were spliced together at one end, creating a continuous fiber of 2 km length. The entire twisted-pair cable was placed on a plastic spool (Fig. 2.4f). Around 2 m of the end of the twisted-pair cable with the splice were coiled onto a plastic spool (Fig. 2.4b), serving as top of the measurement

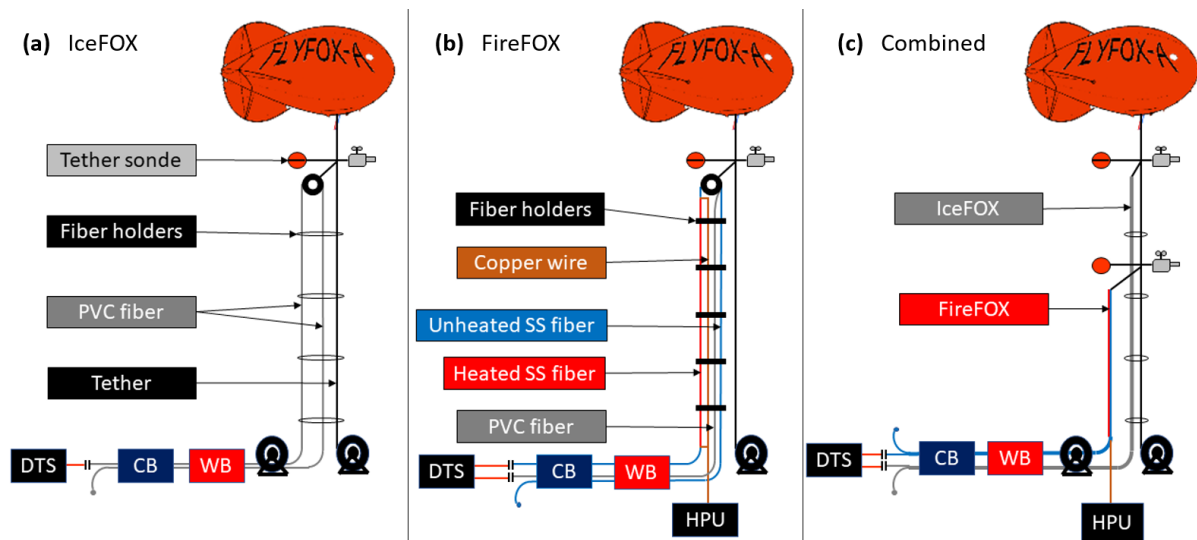


**Figure 2.3** FODS setups used during the campaign “FLYFOX-A” (Flying fiber-optic experiment in the Arctic), showing PVC- and stainless-steel-coated (SS) cables, distributed temperature sensing device (DTS), cold (CB) and warm (WB) calibration baths, and heat pulse unit (HPU) for heating SS-coated cables. (a) IceFOX setup (unheated fiber-optic experiment) for measuring air temperatures, (b) FireFOX setup (heated fiber-optic experiment) for measuring air temperatures and horizontal wind speeds, and (c) combination of (a) and (b).

profile. During the ascent of the balloon a tether sonde (*TTS111*, *Vaisala*, *Helsinki*, *Finland*) was attached to the tether 0.7 m above the plastic spool (Fig. 2.4d). Then the twisted-pair cable was loosely fixed to the tether every 40 m af to 60 m af on average with cable holders consisting of wire (Fig. 2.4c).

Two thermally insulated water baths were used for the calibration of temperatures from Raman backscatter intensities. The cold bath was filled with crushed ice to keep temperatures at around 0 °C. In the warm bath (Fig. 2.4e) an aquarium heater kept temperatures at around 20 °C for all experiments except 180910 where it was set to 30 °C. Uniform temperatures inside the baths were ensured by aquarium pumps with attached perforated hoses to mechanically mix the water baths by continuous stirring. Water temperatures in the baths were measured by one Pt100 thermometer per bath with an accuracy of at least  $\pm 0.1$  K which served as the reference for the FODS measurements within the baths. After lifting the tethered balloon up to maximum height, between 6 m and 13 m of the lower end of the twisted-pair cable were placed in each of the baths, yielding two separate sections of fiber-optic cable in each calibration bath (Fig. 2.3).

All experiments were conducted in a single-ended fiber configuration, i.e., only one fiber-optic

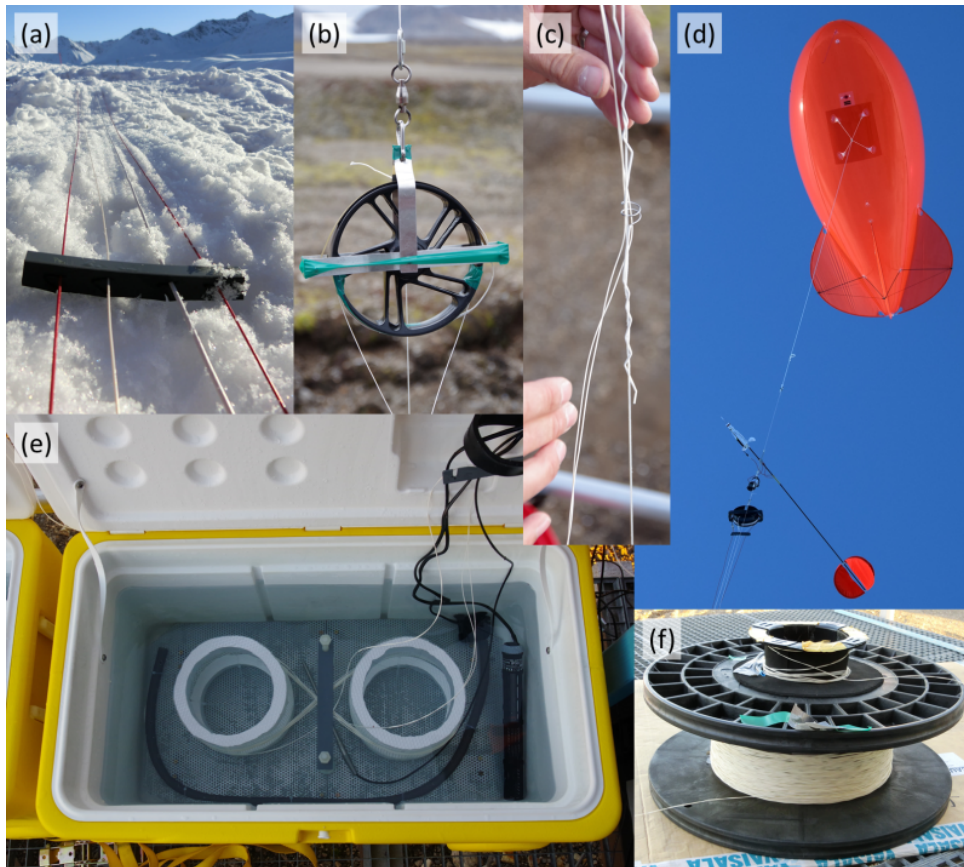


**Figure 2.4** Documentation footage of the fiber-optic setups. (a) FireFOX cables with red stainless-steel-coated cables, thin white PVC-coated cable and thick white copper wire, tied together by black silicon clamps, (b) top spool of IceFOX setup, (c) cable holders of IceFOX setup, (d) tethered balloon, tether sonde and top of FireFOX setup with spool and cables, (e) warm calibration bath containing PVC-coated cable, aquarium heater and aquarium pump, (f) ground-based cable spool of IceFOX setup.

cable at the end of the twisted-pair cable was connected to the DTS device. The single-ended configuration resulted in light pulses traversing the fiber-optic cables upward to the top of the profile and then downward again. The two fiber profiles were thus named ascending and descending branches of the profile. IceFOX experiments reached maximum fiber heights between 400 and 800 m above ground level (agl), and lasted for 1 hour to 14 hours (Fig. 2.2b). A very similar setup was successfully employed by Keller et al. (2011) who used it to estimate the height of the nocturnal boundary layer.

The FireFOX setup (Fig. 2.3b) was based on a fiber-optic cable with a diameter of 50  $\mu\text{m}$  which was loosely buffered in a gel and coated with stainless steel (SS) and red PVC sheathing, resulting in a total outer diameter of 1.25 mm for the complete cable (*BRUGG GROUP, Brugg, Switzerland*). Only around 300 m of cable were used, since its relatively large weight and the complicated setup of the experiment precluded lifting a longer cable into the air. The central 4 m of the cable were coiled around a plastic spool (Fig. 2.4d at the bottom), resembling the spool at the top of IceFOX. A length of 113 m of cable between this center and both ends of the cable were chosen as ascending and descending branches, respectively. The ascending branch was connected at its bottom and top to a copper wire which was attached to a heat pulse unit (HPU, *Heat Pulse Control system, Silixa, Elstree, UK*) for resistively heating this fiber branch. The set and corrected heating rates are discussed in 2.2.4. Temperature differences between heated ascending and unheated descending fiber branch could then be used to calculate fiber-normal, i.e. horizontal wind speeds (Sayde et al., 2015, see 2.2.4). Together with a reference cable of the same making as individual cables from IceFOX, the two SS-coated branches and the copper wire were aligned and fixated ca. every 8 m with cable holders made of silicon (Fig. 2.4a). Cable sections close to the lower end of the reference cable and to the two ends of the SS-coated cable were placed in the calibration baths as explained for IceFOX. The lower end of the reference cable and the end of the SS-coated cable corresponding to the ascending heated branch were each connected to the DTS device, creating two single-ended fiber configurations. The three FireFOX experiments were restricted in maximum flight height to around 100 m and were running between 1 hour and 14 hours long.

For 180918 and 180921, IceFOX and FireFOX were launched together (Fig. 2.3c), increasing data availability for these days and slightly altering the experiments since ascending branches of both IceFOX fiber and FireFOX SS-coated fiber were connected to the DTS device while the PVC-coated reference fiber of FireFOX was not used.

### 2.2.2. Calibration

Fiber temperatures were calibrated by performing a full matrix inversion of Eq. (2.2), where three of the four available reference bath sections were used to determine the instrument- and fiber-specific parameters  $\Delta\alpha$ ,  $\gamma$  and  $C$ . Calibration of fiber-optic data was performed using the pyfocs software developed in the Micrometeorology group at the University of Bayreuth (Lapo and Freundorfer, 2020). I used the fiber sections in the cold and warm bath adjacent to the DTS device and in the cold bath behind the descending fiber branch for calibrating the temperatures. These sections were chosen to yield best calibration quality because temperatures in the cold bath were closer to the ambient air than in the warm bath, and because sections close to the DTS device showed highest signal-to-noise ratios.

However, the assumption of a constant differential attenuation  $\Delta\alpha$  across the fiber-optic cable is not valid because the splices in the fiber-optic cable induced persistent changes in differential attenuation behind the splice. Since the matrix inversion cannot account for a varying differential attenuation, this adds to the uncertainty in fiber temperatures where values of the ascending fiber branch exceeded the ones of the descending branch by 0.3 to 0.6 K close to the surface, while both branches showed equal fiber temperatures at the top of the profile (see Fig. A.1).

The fiber splices also caused step losses  $\Delta x_{S,As}$ , which were corrected following the approach of Hausner and Kobs (2016) with some modifications (see Fig. A.2):

$$\Delta x_{S,As} = x_{S,As}(z_1) - x_{S,As}(z_2) - [\Delta\alpha_1(z_{splice} - z_1) + \Delta\alpha_2(z_2 - z_{splice})], \quad (2.3)$$

where  $x_{S,As}$  is the log ratio of Raman Stokes to Antistokes  $\ln\left(\frac{P_S}{P_{As}}\right)$  averaged over experiment duration,  $z_1$  and  $z_2$  are the locations along the fiber in front of and behind the step-loss-affected section of the fiber, respectively,  $z_{splice}$  is the location of the splice along the fiber, defined as mean of  $z_1$  and  $z_2$ , and  $\Delta\alpha_1$  and  $\Delta\alpha_2$  are the differential attenuations in front of and behind  $z_{splice}$ . In this study two different  $\Delta\alpha$  values were used, estimated with linear regressions of  $x_{S,As}(z)$  for fiber sections of 20 m length in front of and behind the step-loss-affected sections to account for the change in differential attenuation at the splices discussed above. Employing the more complicated approach of step loss correction with two  $\Delta\alpha$  values was justified, as it yielded step losses reduced significantly by 7 % to 33 % relative to the original version by Hausner and Kobs (2016). All parameters of the step loss correction can be found in Tab. A.1.

Since the twisted-pair cable broke during its descent after 180913, two additional splices were made there before recording 180918 and 180921. These splices showed in  $x_{S,As}$  from 180918 and were corrected with Eq. (2.3) as explained before. For 180921  $x_{S,As}$  was not observably affected by the splices, so no correction was performed there.

Electrical induction into the reference baths by leakage from the SS-coated cables caused the resistance thermometer data in the reference baths to show large artificial short-time variability and long-time mean offsets from the true values which increased over time as more water diffused into the protective PVC sheathing of the SS-coated cables. To obtain meaningful fiber temperatures a multi-step reference temperature correction was applied (see Fig. A.3): The difference  $\Delta T_{wc}$  between temperatures in warm bath  $T_w$  and cold bath  $T_c$  were calculated because both showed similar long-time mean offsets

$$\Delta T_{wc}(t) = T_w(t) - T_c(t). \quad (2.4)$$

$\Delta T_{wc}$  was then low-pass filtered to remove the short-time variability using a threshold of 502 s and the BIOR5.5 set of biorthogonal wavelets which have been shown to be appropriate for filtering because of their accurate localization in frequency (Thomas and Foken, 2005). A constant value of -0.05 °C was assigned to the cold bath ( $T_{c,corr}$ ) throughout the time series because this was a typical value in the ice-filled cold bath for the experiments without usage of SS-coated cable. The corrected warm bath temperature ( $T_{w,corr}$ ) was then computed as

$$T_{w,corr}(t) = \Delta T_{wc,filtered}(t) - T_{c,corr}. \quad (2.5)$$

To ensure comparability of temporal variability in fiber temperatures between the three experiments affected by these artifacts and the experiments without usage of SS-coated cable,  $T_w$  and  $T_c$  was low-pass filtered directly with the same settings for the last three experiments.

The dark colored clamps which held the cables of the FireFOX device together, as well as entangling of cables, caused distinct location-specific artifacts in the fiber temperatures by absorption of solar radiation. These artifacts were detected as spatially consistent maxima or minima in both the heated and unheated branches of all experiments, and as peaks in the corresponding temporal standard deviations, and fiber temperatures containing such artifacts were discarded. This process was performed for each experiment and fiber branch separately, as the impact of individual clamps on the data varied, resulting in the removal of 25 % to 47 % of the FireFOX profile (see Fig. A.4 for example).

### 2.2.3. Determining measurement heights

To extract the locations of the atmospheric profiles along the fiber, cables were touched by hand at the lowermost point of the profiles which induced clearly discernible temperature pulses there. Under the assumption that the top of the profile was located in the center of the extracted profile along the fiber, the profile was divided into ascending and descending branches with equal numbers of measurement bins forming pairs corresponding to the same height above ground level. In Fig. A.5 the described selection approach is viewed for one experiment where the mean temperatures within a distance of 2.5 m from the splice at the top of the profile were erroneous due to the combined effects of the splice and radiation absorption by the spool. This artifact-prone section of the fiber was found for all experiments and was therefore discarded from the fiber profile in all cases.

The maximum profile height depends on the interaction of aerodynamic lifting forces by the tethered balloon and wind forces on the balloon and tether, causing horizontal displacement of the balloon and reducing its height. Consequently, maximum profile heights varied over time along with wind speed which necessitated a time-dependent profile height estimation.

The top of the fiber-optic profile was closely collocated with the tethersonde which therefore served as a reference device for the maximum height of the fiber. However, there was significant scatter in the atmospheric pressure and the derived altitude data recorded by the tethersondes. While still on the ground, recorded tethersonde altitude showed changes of more than 4 m within 10 s. I therefore used the same wavelet filter as in 2.2.2 to remove this artificial variability on small time scales. A FFT spectrum of the variability of barometric pressure, taken from a period where the tethersonde was at ground level, revealed that any time scale of less than 12.57 s, corresponding to one of the discrete decomposition levels of the wavelet filter, contained only white noise (Fig. A.6). This time scale was chosen as a threshold for the low-pass filtering of atmospheric pressure and altitude.

The spatial dimension of the IceFOX fiber branches, distance from ground along fiber ( $d_f$ ), was converted to height above ground level ( $h_f$ ) with a linear equation which was possible because the twisted-pair cable was fixed to the tether which was under tension and therefore straight:

$$h_f(t) = d_f \cdot \frac{h_{ts}(t) - d_{tf}}{l_f}, \quad (2.6)$$

with filtered height of tethersonde above ground level  $h_{ts}$ , distance between tether sonde and fiber profile top  $d_{tf} = 0.7$  m, total length of one fiber branch  $l_f$ . For two experiments,  $(h_{ts} - d_{tf})$  exceeded  $l_f$  by up to 2 m and 3 m, respectively, which probably resulted from a miscalculation

of height by the internal tether sonde height calculation and was corrected by multiplying  $h_f$  by a correction factor of 0.9956 and 0.9965, respectively, in these cases. The tether sonde recording stopped due to low batteries for the final 35 % or 5 hours of the 180921 experiment, so  $h_{ts}$  for this period was set to the mean  $h_{ts}$  from the previous 9 hours. There are minor height estimate uncertainties due to distances of around 50 m between the cable fixations causing the twisted-pair cable to be pulled away from the tether by the wind in a quasi-parabolic shape.

A more complicated height correction was applied to the FireFOX profiles because of the non-linear shape of the cables, which hung almost vertically in the air close to the balloon, but became almost horizontal close to the surface. Several approaches of polynomial and logarithmic fitting were tested for deriving the relationship  $h_f(d_f)$  for FireFOX, but none of the trials yielded relationships which traced the shape of FireFOX accurately, as judged by visual inspection. Instead of fitting the relationship with a function temporal correlations between unheated FireFOX and IceFOX temperatures were computed. The pairs of  $d_f$  with highest correlations between the setups were used to manually define a simplified relationship  $d_{f,\text{IceFOX}}(d_{f,\text{FireFOX}})$  with several arbitrarily chosen linear functions for all  $d_{f,\text{FireFOX}}$  (see Fig. A.7 for example). This approach was applied for 180918 and 180921. Since there was no IceFOX deployment for 180916, the relationship was taken from 180918 which showed a similar shape of the FireFOX (see Tab. A.2 for all  $d_f$  relationships). With these simplified functions  $d_{f,\text{FireFOX}}$  was converted to corresponding  $d_{f,\text{IceFOX}}$  which was then used to calculate  $h_{f,\text{FireFOX}}$  with Eq. (2.6). The major cause for height uncertainties of this method of correcting heights is that the actual relationship between  $d_{f,\text{FireFOX}}$  and  $d_{f,\text{IceFOX}}$  varies over time as the maximum profile height changes and the shape of the FireFOX is modified in response to wind variability. This height uncertainty is particularly large close to the surface, where altering lengths of fiber run nearly horizontally.

To generate an equal-spaced vertical space dimension over the experiment,  $T_f$  was linearly interpolated in space to a vertical dimension with a regular step of 0.25 m, starting at 0 m agl and reaching to the profile top.

#### 2.2.4. Calculating meteorological parameters

Unheated fiber temperatures  $T_f$ , from IceFOX data if available, were converted into virtual potential temperatures, while the combined heated and unheated fibers from the FIREFOX experiments provided raw data for computing horizontal wind speeds. Both parameters were then used for estimating Richardson number, an estimator of dynamic stability (see pg. 17).

Virtual potential temperatures  $\theta_{v,\text{unfiltered}}$  from FODS temperatures  $T_f$  were calculated as

$$\theta_{v,\text{unfiltered}} = \left(1 + 0.38 \frac{E}{p}\right) \cdot 0.5(T_{f,a} + T_{f,d}) \cdot \left(\frac{p_0}{p}\right)^{\kappa_L}, \quad (2.7)$$

with Poisson constant  $\kappa_L = \frac{2}{7}$ , reference pressure  $p_0 = 1000$  hPa. Barometric air pressure  $p$  and vapor pressure  $E$  were linearly interpolated in space between tether sonde and BSRN tower measurements. This was justified for  $p$  because the hypsometric equation shows a nearly linear relationship between height and pressure in the lowest 1000 m of the atmosphere. Interpolating  $E$  in space is a strong simplification, but it was unavoidable, since there were no other humidity measurements available at sufficient temporal resolution. Profiles of  $E$  via radiosoundings were only available at intervals of 6 hours. Fiber temperatures of ascending ( $T_{f,a}$ ) and descending

( $T_{f,d}$ ) branches were averaged to reduce the measurement error. As there was no IceFOX deployment for 180916  $\theta_{v,\text{unfiltered}}$  was computed using the unheated temperatures of the descending branch of the SS-coated cable.

The instrument noise of the FODS data was removed from  $\theta_{v,\text{unfiltered}}$  via spatial low-pass filtering with a wavelet filter to avoid interpreting artificial length scales and variability as true features. To estimate the scales influenced by noise, fiber-optic temperature profiles with neutral stability were selected, which were expected to contain little true spatial temperature variability at small scales and thus help displaying unphysical variability. These data were taken from 180910, which was the only experiment showing near-neutral stability over several hundreds of meters for a sufficient period of time. Variance spectra from multi-resolution decomposition (see 2.5) in space of these data showed a distinct peak in spectral power between scales of 0.5 m and 1 m, with increased power up to 4 m relative to larger scales (Fig. A.8). Scales of up to 1 m were interpreted as instrument noise, and the scale range up to 4 m might still have been influenced by noise to some degree, though physical features are probably detectable there. This interpretation lines up with investigations by Thomas et al. (2012) who estimated minimum resolvable eddy scales at weak winds to range between scales of less than a meter and few meters. For the removal of scales of 1 m or less, the BIOR5.5 set of biorthogonal wavelet filters (see 2.2.2) was used as spatial low-pass filter of  $\theta_{v,\text{unfiltered}}$ , with the closest larger discrete length scale of 1.57 m as threshold. The result of this filtering process is shown as an exemplary  $\theta_v$  profile in Fig. 2.5a.

At original spatial resolution of 0.25 m, the virtual potential temperature gradient  $\frac{\partial\theta_v}{\partial h}$  was not calculated as  $\frac{\Delta\theta_v}{\Delta h}$  from wavelet-filtered  $\theta_v$ , but as a spatially smoothed local static stability  $LSS$  from  $\theta_{v,\text{unfiltered}}$ . The algorithm for the detection of sublayers (see 2.4) was based on  $LSS$ , which was calculated for each measurement height  $h$  as

$$LSS(h) = \frac{\langle\theta_{v,\text{unfiltered}}[h, h + l_b]\rangle - \langle\theta_{v,\text{unfiltered}}[h - l_b, h]\rangle}{l_b}, \quad (2.8)$$

where  $\langle\rangle$  denotes spatial averages, which were calculated on  $\theta_{v,\text{unfiltered}}$  over blocks of data above and below  $h$ , respectively, with block length  $l_b = 10$  m defining the vertical extent of these blocks (Fig. 2.6). Local static stability  $LSS$  was thus computed via block average differences at a spatial data resolution of 0.25 m, but with a physical resolution of 10 m. This approach was chosen instead of using  $\frac{\Delta\theta_v}{\Delta h}$  to infer the larger-scale stratification of the atmosphere by filtering out the small-scale temperature variability, especially that caused by instrument noise. Block length  $l_b = 10$  m was chosen as a compromise between capturing shallow temperature inversions close to the surface and deeper inversions further aloft with the sublayer detection algorithm. The selected  $l_b$  made a detection of temperature inversions thinner than 10 m improbable, and resulted in the lower and upper 10 m of the FODS profile being excluded from the calculation of  $LSS$ .

The difference between  $LSS$  and  $\frac{\Delta\theta_v}{\Delta h}$  becomes evident in the fiber-optic profile shown in Fig. 2.5b, where at near-neutral  $LSS$  between 20 m agl and 80 m agl  $\frac{\Delta\theta_v}{\Delta h}$  still showed small-scale variability with values reaching  $\pm 0.08$  K m<sup>-1</sup>. The very constant space scale of the positive and negative peaks in  $\frac{\Delta\theta_v}{\Delta h}$  was artificially induced by wavelet filtering and was close to the filter threshold scale of 1.57 m. Since spatial variability in temperature at scales smaller than 4 m may have been influenced by instrument noise (see Fig. A.8), a substantial part of the observed

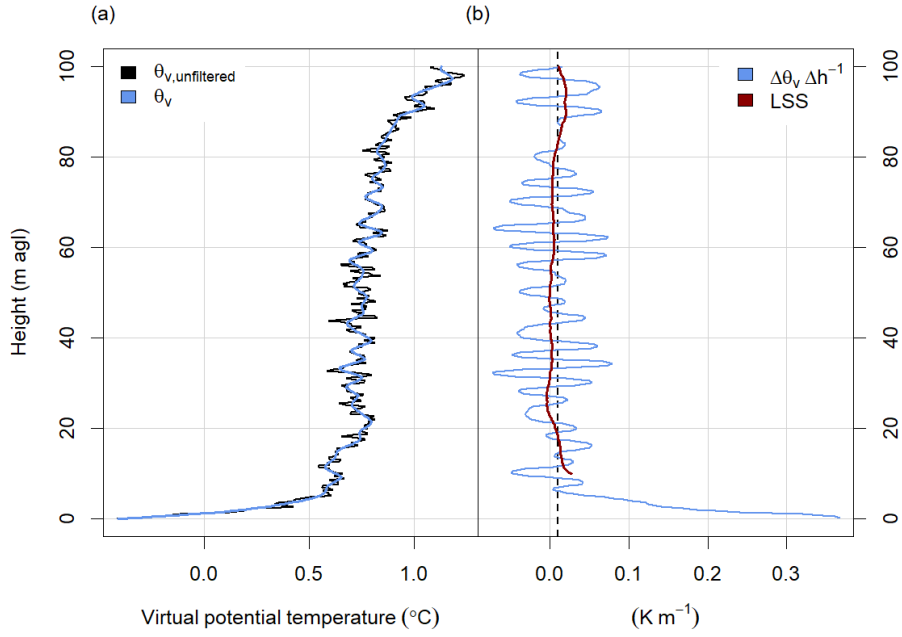


**Figure 2.5** Differently calculated measures of thermodynamic structure in an exemplary instantaneous fiber-optic profile at 03:59:00 UTC on September 13, with a temporal and spatial resolution of 10 s and 0.25 m, respectively. (a) shows unfiltered ( $\theta_{v,\text{unfiltered}}$ ) and wavelet-filtered ( $\theta_v$ ) virtual potential temperature. (b) displays change in  $\theta_v$  with height, as  $\Delta\theta_v \Delta h^{-1}$ , and as local static stability  $LSS$  calculated from block differences in  $\theta_{v,\text{unfiltered}}$  with Eq. (2.8). Vertical broken line marks  $0.01 \text{ K m}^{-1}$ , the defined minimum  $LSS$  of an inversion.

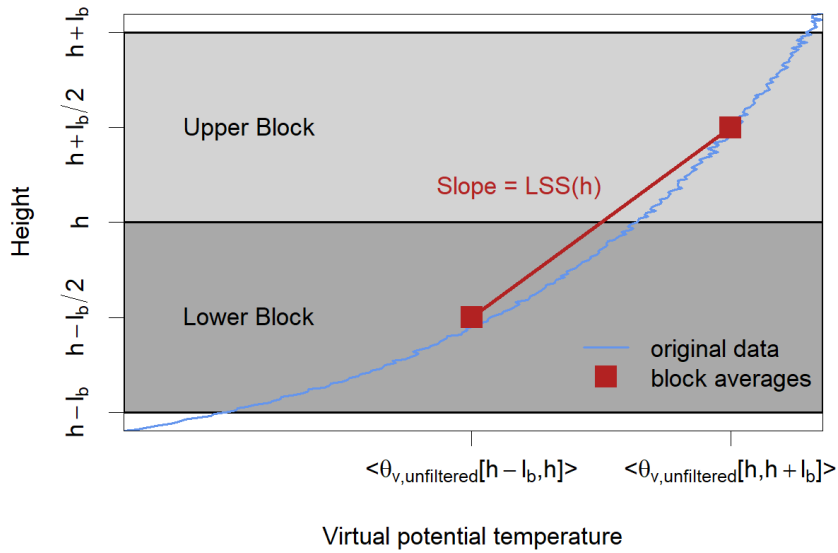


**Figure 2.6** Conceptual illustration of the computation of local static stability  $LSS$  at height  $h$ , using block-averaged differences of virtual potential temperature  $\theta_{v,\text{unfiltered}}$ . Vertical extent of lower and upper block is defined by block length  $l_b$  which was set to 10 m. Spatial averages of  $\theta_{v,\text{unfiltered}}$  within blocks are indicated by  $\langle \rangle$ . Estimate of  $LSS(h)$  is visible as slope of the red line.

spatial variability of  $\frac{\Delta\theta_v}{\Delta h}$  may have been artificial. This supports my choice not to use  $\frac{\Delta\theta_v}{\Delta h}$ , but  $LSS$  for sublayer detection, which may have led to a coarser resolution, but ensured the physical meaningfulness of the detected sublayers.

Brunt-Väisälä frequency  $N_{BV}$  is a measure of static stability defining the natural frequency of vertical oscillations of air parcels under stable conditions after vertical displacement, where  $N_{BV}$  increases with static stability. This type of buoyancy oscillation of air parcels is named internal gravity wave (IGW). In this study  $N_{BV}$  was a valuable measure because it also equals the maximum possible frequency of these IGWs in a stably-stratified fluid.  $N_{BV}^2$  was calculated as

$$N_{BV}^2 = g \cdot \Theta_v \cdot LSS, \quad (2.9)$$

with gravity acceleration  $g = 9.81 \text{ m s}^{-2}$ .  $N_{BV}$  averages over time ( $\overline{N_{BV}}$ ) were computed with

$$\overline{N_{BV}} = \sqrt{\overline{N_{BV}^2}}. \quad (2.10)$$

The minimum event scale  $t_{IGW}$  of IGWs equals half their period length and can therefore be calculated following Collineau and Brunet (1993) from  $N_{BV}$  as

$$t_{IGW} = (2 \cdot N_{BV})^{-1}. \quad (2.11)$$

Absolute differences in fiber temperatures of FireFOX experiments between heated and unheated branches are negatively correlated to the fiber-normal wind speed (Sayde et al., 2015). Horizontal wind speeds  $U$  were calculated from FireFOX data, using this relationship with a simplification of the approach by Sayde et al. (2015): Since unheated fibers were of identical make, albedo and emissivity did not differ between them, so shortwave and incoming longwave radiation were neglected in energy balance computations. Longwave radiative energy loss needed to be considered because of the temperature differences between heated and unheated fibers. Convective heat flux from the unheated fiber was neglected as well, since temperatures of the unheated fiber were assumed to equal the temperature of the surrounding air.

The HPU power output was higher than chosen in the settings which led to distinct underestimation of the wind speeds. This issue was solved by selecting a height subsample of the FireFOX profile with high data availability due to fewer artifacts from the cable holders, and adjusting the heating rate until calculated wind speeds in the FireFOX subsample matched those of the SODAR (see Tab. 2.1). Resulting  $U$  values were block-averaged to 5 m resolution due to the large height uncertainty of the FireFOX cables.

The Richardson number is a well-established parameter to assess dynamic stability in the atmosphere, where negative, near-zero and positive values describe unstable, neutral and stable conditions, respectively. The combined  $\theta_v$  and  $U$  profiles of the last three FODS experiments enabled the calculation of a simplified local gradient Richardson number  $Ri$  without information on the wind directional shear as

$$Ri = \frac{g}{\Theta_v} \cdot \frac{\frac{\partial\theta_v}{\partial h}}{\left(\frac{\partial U}{\partial h}\right)^2}. \quad (2.12)$$

Due to the large height uncertainty in the data caused by the complicated height correction of the FireFOX data and the consequently error-prone matching with  $\theta_v$  from IceFOX, I calculated  $Ri$  with a spatial resolution of 5 m instead of 0.25 m.

**Table 2.1** Set and corrected heating rates of the heat pulse unit for the three FireFOX experiments. Correction was done via calibrating fiber-optic wind speeds with SODAR wind speeds. For the 180918 experiment heating rate was changed during recording.

Experiment	Set heating rate (W m <sup>-1</sup> )	Corrected heating rate (W m <sup>-1</sup> )
180916	2.7	4.5
180918 (1)	2.7	4.7
180918 (2)	1.8	3.1
180921	2.7	6.2

Measurements from the BSRN tower were used for the calculation of bulk Richardson number in the surface layer as

$$Ri_b = \frac{g}{\Theta_v} \cdot \frac{\Delta\Theta_v \cdot \Delta h}{(\Delta u)^2 + (\Delta v)^2}, \quad (2.13)$$

with vertical separation of measurements  $\Delta h$ , zonal wind  $u$  and meridional wind  $v$ . Very low wind speeds and wind speed shear caused a frequent occurrence of very high absolute values in both  $Ri$  and  $Ri_b$ . In such cases, Richardson numbers below -30 and above 30 were set to -30 and 30, respectively, to simplify calculation of statistics. In this work, I defined the critical  $Ri$  or  $Ri_b$  as 0.25 (Miles, 1961; Howard, 1961; Grachev et al., 2013), i.e., every Richardson number below and above this value is referred to as “subcritical” and “supercritical”, respectively.

### 2.3. Ancillary observational systems

Several measurements apart from the tethersonde data were used to provide a reference and larger context for the FODS data. An important data source was the closely collocated *Baseline Surface Radiation Network* (BSRN, 78.92261 °N, 11.92740 °E, 15.21 m asl at pressure probe of BSRN field), a combination of standard meteorological measurements on the BSRN tower in 2 m and 10 m agl (Maturilli, 2019a), radiation data in the BSRN field (Maturilli, 2019b) and cloud base height data (Maturilli, 2019c). Radiosondes were launched at the AWIPEV balloon house every 6 hours during the measurement campaign, in the course of the “Year of Polar Prediction”, organized by the World Meteorological Organization. These radiosoundings served as additional reference for the fiber-optic data (Maturilli, 2019d).

An Eddy-Covariance (EC) system was located approximately 300 m south of the balloon house (78.92142 °N, 11.91416 °E, 27 m asl). 3-D wind as well as water vapor and carbon dioxide concentrations were recorded at 20 Hz, using an ultrasonic anemometer (*CSAT3*, *Campbell Scientific*, *Logan, UT, USA*) and an infrared gas analyzer (*LI-7500(A)*, *LI-COR*, *Lincoln, NE, USA*). Data from the same installation have been used in other publications referenced in this thesis (Jocher et al., 2012, 2015). Turbulent fluxes were calculated via the EC method including several correction routines as described in Thomas et al. (2009). For EC processing a perturbation time scale of 410 s was used, which has been identified to be the largest time scale of undisturbed equilibrium turbulence in power spectra of the vertical wind speed. Winds from 150 ° to 270 ° were shown to be related to artificial positive sensible heat fluxes, which have been attributed to external gravity wave activity (Jocher et al., 2015). During fiber-optic exper-

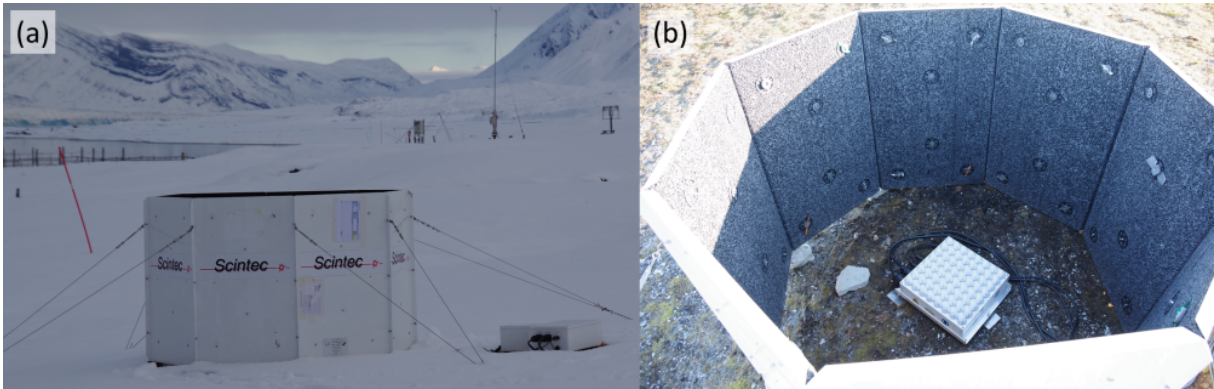


**Figure 2.7** Documentation footage of the SODAR installation. (a) Sound shield, (b) antenna array.

iments, most positive sensible heat fluxes related to these directions showed corresponding air pressure variability resembling the observations by Jocher et al. (2012), with several unphysical spikes. EC data showing positive sensible heat flux from these directions were therefore omitted from the analysis. The same was done for data with horizontal rotation angle magnitudes of more than  $5^\circ$ . 21 % and 6 % of data were excluded due to artifact-prone sensible heat flux and large rotation angles, respectively, between September 9 and September 22. This amounted to a total exclusion of 25 % of data in this period, of which 61 % corresponded to snow-covered conditions, which were continually present after September 15.

A *Sound Detection And Ranging* (SODAR) system (*SFAS*, *Scintec*, *Rottenburg*, *Germany*) was installed around 100 m south-east of the balloon house ( $78.92246^\circ\text{N}$ ,  $11.92494^\circ\text{E}$ , Fig. 2.7) on September 12, 2018, which recorded 3-D wind data in the lowest 400 m of the atmosphere until the end of the campaign (Fig.2.2a) with a resolution of 5 m and 10 min to 15 min. There was a considerable amount of untrustworthy or missing data in the upper part of the profiles, so only the lowest 250 m agl were taken into account. The lower end of the profile was also affected by erroneous and missing data due to ground clutter in heights of up to 15 m agl. This effect caused such unrealistic data in the lowest measurement height at 10 m agl that measurements at this height were excluded.

Synoptic forcing of the local observations was inferred from NCEP/NCAR reanalysis data (Kalnay et al., 1996), accessed through the NOAA/ESRL Physical Sciences Laboratory, Boulder, Colorado, on their website at <http://psl.noaa.gov/> Daily averages of these reanalysis data were examined at 850 hPa level which is more appropriate for investigating the synoptic forcing than the 500 hPa level for polar areas (e.g. Schulz, 2017).

## 2.4. Detecting sublayers and surface-based inversions

The temporal course of  $LSS$  across the vertical profile was used to detect “stable” and “non-stable” sublayers within the IceFOX profiles, using the following sublayer detection algorithm:

1. A threshold  $LSS_{crit} = 0.01 \text{ K m}^{-1}$  was set. Any  $LSS > LSS_{crit}$  was defined as “stable”, and any  $LSS < LSS_{crit}$  as “non-stable”.

2. Stable sections in instantaneous profiles were merged in space for each time step, and the same was done for non-stable sections (see Fig. B.1).
3. Spatially merged stable and non-stable sections in instantaneous profiles were temporally merged forward in time to create preliminary layers: Beginning with the second time step of the time series, each section was merged with the most abundant section of the same stability category at the previous time step and within the same height range. If no such section was available, no temporal merging was applied (see Fig. B.2).
4. Beginning with non-stable layers, any layer with a duration  $LD < 5$  min was included in the best-matching neighboring layer after the following scheme, where a neighboring layer was defined as a layer “touching” the spatiotemporal boundaries of the observed layer: Only neighboring layers with  $LD > LD_{crit}$  were used in this step. Neighboring layers in the same stability category as the observed layer were preferentially chosen, if available. The observed layer was included in the neighboring layer that fulfilled these requirements and showed the longest  $LD$ . If no such neighboring layer was present the observed layer was skipped by the algorithm and tried to be matched to a neighboring layer again in another iteration. This process was repeated until there were no layers left with  $LD < LD_{crit}$  (see Fig. B.3).
5. For the final merging step layers were ordered by (1.) stability classification, placing non-stable layers before stable layers, and (2.) earliest occurrence of layer in time, in descending order. Following this order, each layer was assigned to the neighboring layer (see previous step) in the same stability category with the earliest occurrence in time. If no such layer existed no merging was done (see Fig. B.4).
6. Final detected layers were named with integer numbers so that the magnitude shows the order of appearance of the layers through the course of the experiment and the sign shows the stability category, with negative and positive numbers specifying non-stable and stable layers, respectively (see Fig. B.5).

$LSS_{crit} = 0.01 \text{ K m}^{-1}$  was chosen as a compromise between (1.) capturing temporally consistent ILs in the upper part of the profiles which requires a low positive  $LSS_{crit}$  and (2.) avoiding large parts of the profiles from being detected as a single IL, which would require a larger  $LSS_{crit}$ . Further,  $LSS > 0.01 \text{ K m}^{-1}$  clearly deviated from a Gaussian distribution of  $LSS$  for all experiments, suggesting that  $LSS > 0.01 \text{ K m}^{-1}$  represented stably-stratified conditions, as opposed to neutral or unstable conditions (example see Fig. B.6).

Any  $LSS > 0.01 \text{ K m}^{-1}$  corresponds to an increase in dry-bulb air temperature with height. Thus, corresponding profile sections defined as “stable” can simultaneously be viewed as dry-bulb temperature inversions in the atmosphere. From here, “stable” and “non-stable” sublayers detected in this thesis are therefore named inversion layers (IL) and non-inversion layers (NIL), respectively.

The arbitrary  $LD_{crit}$  frequently caused layers with  $LD < 5$  min to be merged with layers of the opposed stability category. This effect resulted in the incorporation of 7 % to 60 % of  $LSS > 0.01 \text{ K m}^{-1}$  into NILs, and of 1 % to 7 % of  $LSS < 0.01 \text{ K m}^{-1}$  into ILs.

The surface-based temperature inversion (SI) was detected using  $LSS$  data in instantaneous fiber-optic profiles and defined as the height range between the surface and the height  $h_{SI}$  of the SI. A SI was only detected if the lowermost  $LSS$  value was higher than  $0.01 \text{ K m}^{-1}$ , i.e., showed a temperature inversion. In these cases, the height of the lowermost measurement bin in the fiber profile with  $LSS < 0.01 \text{ K m}^{-1}$  was defined as  $h_{SI}$ . Since the lowermost available  $LSS$  value was located at 10 m agl due to computational reasons, any SI with a lower thickness than 10 m could not be detected with this method. Further, the unavailability of  $LSS$  below 10 m agl posed the risk of missing a shallow layer without temperature inversion beneath a temperature inversion at 10 m agl. This was however regarded unlikely because under stable conditions temperature increase with height is typically strongest close to the surface, which was mostly confirmed in  $\frac{\Delta\theta_v}{\Delta h}$  in the fiber-optic data. The SI defined using this method was a placeholder for the SBL which was not explicitly discussed in this thesis.

## 2.5. Multiresolution decomposition of virtual potential temperatures

Time and space scales in the atmospheric profiles were investigated via multiresolution decomposition (MRD, e.g. Howell and Mahrt, 1997; Vickers and Mahrt, 2003; Thomas, 2011) of virtual potential temperatures. MRD is a simple wavelet decomposition using unweighted averages as basis. An MRD successively decomposes a regular time or space series  $\phi$  into subrecords of dyadic length  $n = 2^m$ , with decomposition mode  $m = 1, 2, \dots, M$ , and total number of decomposition modes  $M$ . A series decomposed by the algorithm therefore must have a total length of  $2^M$ . For each  $m$  the decomposed series from the previous modes is averaged over subrecords. These averages are subtracted from the series before it is passed to the next mode (see Fig. C.1). The MRD results can be used to calculate variance  $D_{\phi_m}^2$  for each  $m$  as

$$D_{\phi_m}^2 = \frac{1}{2^{M-m}} \sum_1^{2^{M-m}} \phi_m^2, \quad (2.14)$$

yielding variance spectra of  $\phi$ .

As a local transform, MRD captures aperiodic events, which are not revealed by transform methods focused on periodicity such as the Fast Fourier Transform. This ability makes MRD more appropriate for the aperiodic, highly variable atmospheric structures typical for very stable conditions. Furthermore, all modes are statistically independent and the orthogonal decomposition satisfies Reynolds averaging on all scales (Thomas, 2011). The algorithm used here was successfully validated against previous implementations of MRD (e.g. Mahrt et al., 2009; Thomas, 2011), and correctly detected event scales (half-period lengths) in an artificial sinusoidal time series (Fig. C.2).

### 2.5.1. MRD in space and time with one window for entire experiments

Time and space scales in the atmospheric profiles were assessed using MRD on virtual potential temperatures over entire spatial and temporal extents of the experiments. Since MRD input should not contain missing values, the profiles were cut off at the greatest measurement height with full data availability for individual flights. Missing values in the remaining data were linearly interpolated in space which was only necessary for 180916 where artifacts from cable

holders made an exclusion of sections of several meters length necessary (see 2.2.2). For spatial and temporal MRD, data were resampled by linear interpolation to the closest larger dyadic length in space and time, respectively, as the MRD requires dyadic data lengths and thereby the loss of more values by reducing the data to a dyadic length was avoided.

Spatial MRD was prone to attributing temperature variability to the temperature increase with height, especially at large space scales. This problem could not be mitigated via linear detrending of instantaneous temperature profiles in space before decomposition, because detrending across such a large height range would have induced artificial scales into the decomposed temperatures.

### 2.5.2. MRD in time with several windows for entire experiments

Vertical length scales of motions and coupling within the atmospheric profiles were investigated using MRD in time similar to the one described in 2.5.1. The difference to the previous MRD was that no resampling of data to dyadic lengths was done, but data were divided into time windows of a dyadic length of 640 s instead, shifted across the time series at 600 s block length. This resulted in an overlap of 6.3 % between the windows which did not cause observable violation of statistical independence of the windows. In each window the time series were decomposed for each measurement bin. The MRD window length of 640 s was chosen to capture motions at smaller time scales than those generating large  $\theta_v$  variability through oscillations of LIs, which typically were 600 s or larger (see 3.5.1).

This MRD configuration enabled the calculation of two-point correlations for all decomposition modes which served as an estimate of the level of agreement between measurement bins in the profiles. The two-point correlation

$$R_{\phi,ij} = \frac{\overline{\phi'_i \phi'_j}}{\sigma_{\phi_i} \sigma_{\phi_j}} \quad (2.15)$$

is the Pearson correlation coefficient between the time series  $\phi_i$  and  $\phi_j$  of any two measurement bins within the profile for any decomposition mode.

Correlation decay of  $R_{\phi,ij}$  with separation distance between measurement heights can be used to define an arbitrary vertical length scale  $L_v$  analogous to the horizontal length scale described by Mahrt et al. (2009). The closest heights both above and beneath each measurement bin with a correlation lower than  $1/e$  were selected and their vertical distance was defined as  $L_v$ . An example for this method is shown in Fig. C.3. This approach was employed for all modes and yielded  $L_v$  values for each height where  $R_{\phi,ij} < 1/e$  was reached within the measurement profile above the investigated height. If the correlation did not fall below  $1/e$  above the surface,  $L_v$  was computed with the surface as lower boundary because atmospheric motions are physically restricted by the surface. In this work, I did not use or discuss other vertical length scales defined using temperature (e.g. Sorbjan and Balsley, 2008; Mahrt et al., 2012).

### 2.5.3. MRD in space and time with one window for detected sublayers

Samples of virtual potential temperatures representing individual detected sublayers (see 2.4) were decomposed in time and space into multiresolution modes. Several sampling techniques were tested for their applicability and the quality of their results.

One sampling approach was based on restructuring the data by creating a new data matrix for each layer with duration and maximum thickness of the sublayer as dimensional extents. In this matrix the  $\theta_v$  time series at the mean height of a layer was placed at the center of the space dimension, and the other measurements belonging to the sublayer were grouped above and below this “height”. Thus, this approach generated layer samples which fluctuated in height. This technique required additional layer classification before creation of the restructured matrices: (1) Sublayers enclosed within other sublayers of the opposing stability category were integrated in these outer sublayers and (2) Vertically and temporally continuous samples of the resulting sublayers spanning the entire layer duration were selected, i.e., parts of sublayers not connected in space to the main part of the sublayers were discarded. These steps helped to create a meaningful average layer height without large variation for the restructured matrices. While this sampling method allowed the computation of meaningful spatial MRD spectra, it distinctly changed the temporal signals by inducing new time scales caused by strong height oscillations of the subsample, and by removing large time scales due to the centering of the mean layer heights.

Using constant measurement heights for the sublayer sampling avoids the above problems which is why the following approach was chosen for the MRD calculations:

1. A sublayer sample ( $S$ ) of  $\theta_v$  spanning the maximum vertical extent and the duration of a sublayer was selected.
2. For each space bin within  $S$ , layer contributions over the temporal extent of  $S$  were calculated. Layer contribution is the ratio of data in  $S$  belonging to the layer. The spatial range where layer contributions above average occurred was selected as spatial subsample  $S_{s1}$  (Fig. C.4a).
3. For each time bin within  $S_{s1}$ , layer contributions over the spatial extent of  $S_{s1}$  were calculated. The temporal range where layer contributions above average occurred was used for spatiotemporal subsample  $S_{s1,t1}$  (Fig. C.4b-c).
4. If at least one of the average layer contributions of the previous two steps was below 0.5, these steps were repeated on subsample  $S_{s1,t1}$  as a second iteration, creating the subsample  $S_{s2,t2}$  (Fig. C.5).
5. A spatial subsample  $S_{sd,t}$  yielding the closest smaller dyadic data length in space was selected from the returned spatiotemporal subsample of the previous steps to enable MRD in space. The space window with the highest layer contribution was chosen (Fig. C.6a).
6. The final spatiotemporal subsample  $S_{sd,td}$  yielding the closest smaller dyadic data length in time was selected from  $S_{sd,t}$  to enable MRD in time. The time window with the highest layer contribution was chosen (Fig. C.6b).

The resulting subsamples of sublayers of this routine are exemplarily shown for 180913 in Fig. C.7.

Virtual potential temperatures of  $S_{sd,td}$  were decomposed into their respective temporal and spatial multiresolution modes without further resampling. An approach of padding  $S_{sd,td}$  for the spatial MRD was tested: Data within  $S_{sd,td}$ , but outside the spatial extent of the detected layer for individual time steps were discarded. Gaps were filled by (1.) linear spatial interpolation,

(2.) mirroring data in temperature and space, and (3.) zero-padding, i.e., assigning the closest available measurement in space to missing data (Fig. C.8). Since this padding approach did neither improve nor significantly change the resulting spatial spectra, no padding was used in the results.

---

## 3. Results and discussion

### 3.1. Atmospheric conditions inferred from traditional measurements and models

Results from traditional measurement techniques employed in the measurement campaign are presented and discussed in this section, including data from the BSRN tower and field, the EC station, SODAR, tethersondes and radiosondes (Fig. 2.1). Further, large-scale atmospheric conditions were inferred from NCEP/NCAR global circulation model reanalysis data (Kalnay et al., 1996). These measurements and model results are shown here to provide context for fiber-optic data which are the basis of a profound analysis of thermodynamic and dynamic structure of the lower troposphere in the later parts of the results and discussion section.

#### 3.1.1. Conditions across the measurement campaign

Here, an overview of the time-resolving data recorded across the campaign is provided. These measurements were taken at the BSRN tower and field, the EC station and by the SODAR.

The measurement campaign was divided into two main periods by the absence and presence of snow cover: On September 15, 2018, Ny-Ålesund received several centimeters of snowfall which remained to the end of the campaign, at dominantly cloud-free conditions. This resulted in the first three balloon launches representing snow-free surface conditions, while the last three flights were launched above a snow-covered surface without cloud cover. This distinct transition in surface conditions coincided with pattern changes for several atmospheric parameters: Surface air temperatures ranged between  $-1\text{ }^{\circ}\text{C}$  and  $6\text{ }^{\circ}\text{C}$  before the snowfall and stayed below  $0\text{ }^{\circ}\text{C}$  afterwards with many cold-air events (Fig. 3.1a). These events corresponded to an increase in strength of the surface-based temperature inversion. The inversion was present almost permanently under snow-covered conditions, while near-neutral stratification was typical during higher solar angles in the previous snow-free period (Fig. 3.1b).

Strong winds were distinguished from weak winds using the hockey stick method by Sun et al. (2012) in this thesis, where the strong-wind regime indicated the presence of significant shear-induced turbulence. Following this method, all winds with  $U > 2.5\text{ m s}^{-1}$  at 2 m agl were defined as strong winds (see Fig. D.1).

For most of the campaign, wind speeds at 2 m agl and 10 m agl did not exceed  $2\text{ m s}^{-1}$  (Fig. 3.1e). The surface wind only exceeded  $2.5\text{ m s}^{-1}$  on three days of the campaign, which coincided with minima in air pressure (Fig. 3.1d), indicating frontal passages. Winds mainly originated from east and southeast during the campaign, with southwest as a second main wind direction (Fig. D.2). The southwest direction was more common at 2 m agl than at 10 m agl and the two main directions were less clearly separated there. At the EC station this southwest lobe was turned more towards south than at the BSRN tower and winds with speeds of less than  $1\text{ m s}^{-1}$  mostly originated from this direction. Strong winds above  $2.5\text{ m s}^{-1}$  arrived almost exclusively from southeast and particularly east, with a maximum at around  $100\text{ }^{\circ}$ . The spread of wind directions became narrower with the beginning of snow cover, mainly covering south-east to south-west, where north-west and east winds were also common before (Fig. 3.1f). During weak-wind periods after September 15 the wind speeds at 2 m agl often exceeded the wind speed at 10 m agl during cold-air events which coincided with southwest winds, a clockwise rotation of the wind at 2 m agl relative to the wind at 10 m agl.

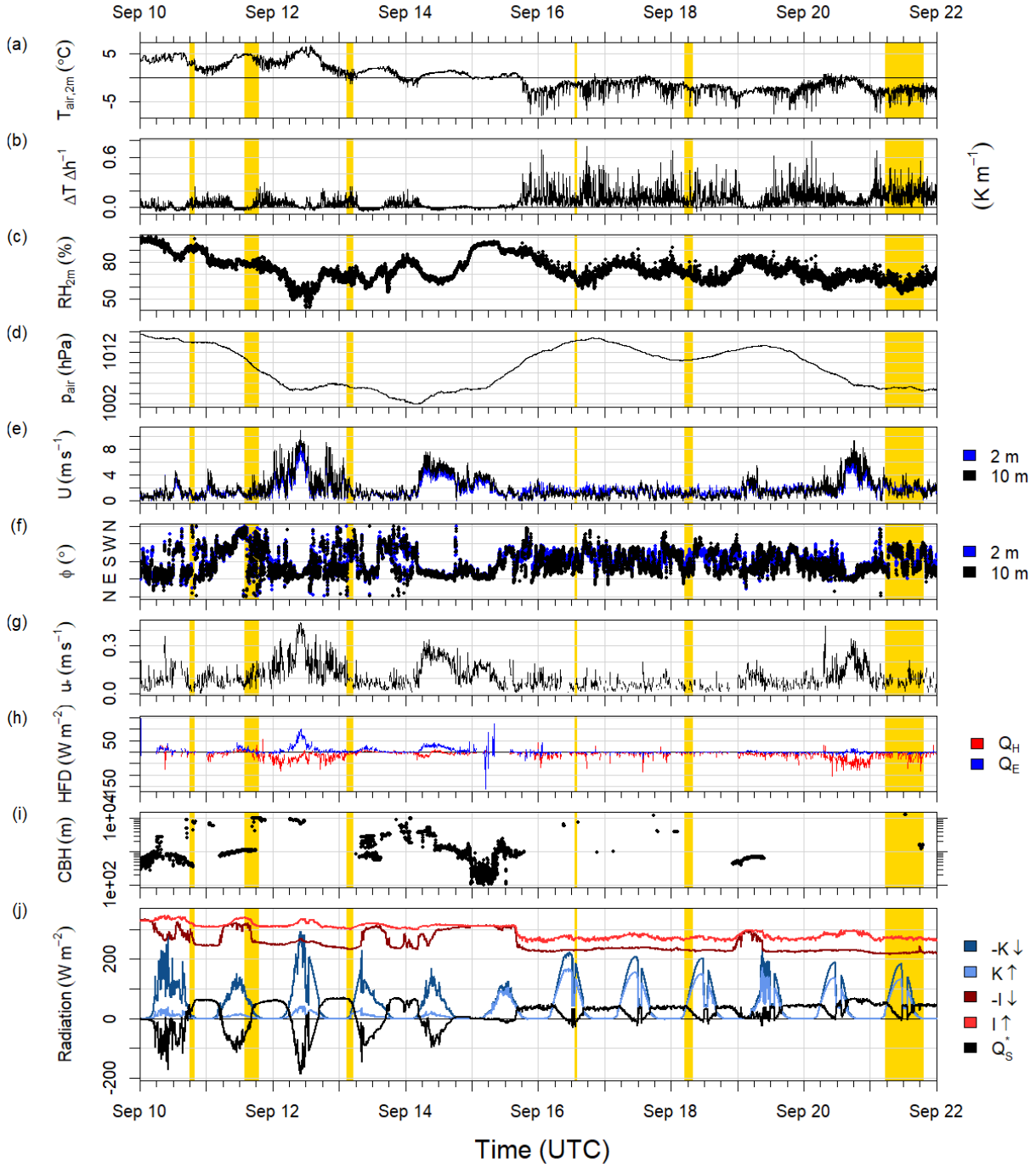


**Figure 3.1** Surface-based atmospheric measurements across the entire measurement campaign. Golden surfaces mark the periods of all six fiber-optic experiments. (a) Air temperature  $T_{air,2m}$  at 2 m agl, (b) temperature gradient  $\Delta T \Delta h^{-1}$  between 2 m and 10 m, (c) relative humidity  $RH_{2m}$  at 2 m agl, (d) air pressure  $p_{air}$  and (e) horizontal wind speed  $U$  and (f) direction  $\phi$  at two heights were recorded on the BSRN tower. (g) Friction velocity  $u_*$  and (h) heat flux densities (HFD) of sensible ( $Q_H$ ) and latent ( $Q_E$ ) heat fluxes were measured by the EC station. (i) Cloud base height (CBH) recorded by the ceilometer at BSRN field. (j) Global radiation  $K\downarrow$ , shortwave reflected radiation  $K\uparrow$ , atmospheric radiation  $I\downarrow$ , terrestrial radiation  $I\uparrow$  and net radiation  $Q_S^*$  were captured by BSRN.

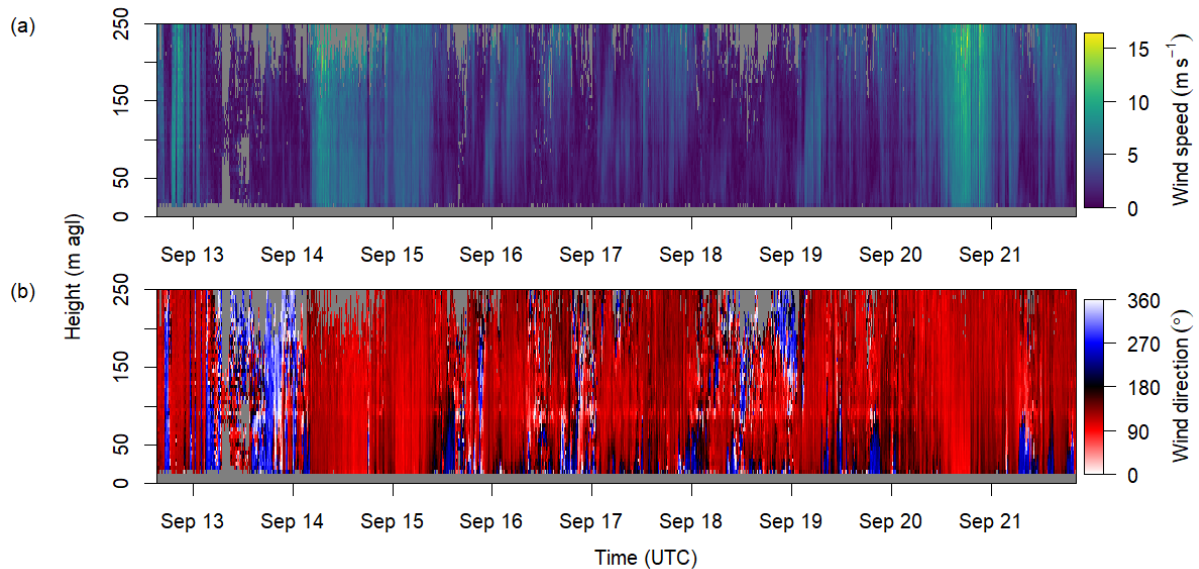


**Figure 3.2** Time series of wind measurements via SODAR across the measurement campaign, with (a) horizontal wind speed, and (b) wind direction.

The wind profiles in the lowest 250 m above Ny-Ålesund showed rather uniformly southeasterly to easterly directions under strong-wind conditions during the campaign, as the SODAR data revealed (Fig. 3.2). At lower wind speeds however, significant structures were observed: After September 15, profiles often showed east and southeast winds at higher levels, but with events of south to southwest winds in the lowest 60 m agl to 90 m agl, turning clockwise towards the surface. Before September 15, uniform northerly winds were observed under weak-wind conditions in the lowest 200 m of the atmosphere. Less than 1 % of winds originated from southwest directions above 60 m agl (see Fig. D.3).

The friction velocity  $u_*$  showed very similar patterns to the horizontal wind speeds, with magnitudes only exceeding  $0.1 \text{ m s}^{-1}$  for longer periods on days with strong winds (Fig. 3.1g). Latent heat flux  $Q_E$  and sensible heat flux  $Q_H$  rarely reached magnitudes higher than  $20 \text{ W m}^{-2}$  which typically corresponded to strong winds and led to downward-directed  $Q_H$  and upward-directed  $Q_E$ . At high  $u_*$ ,  $Q_H$  caused significant energy input at the surface under snow-covered conditions on September 20, where the stable stratification was eroded despite radiative energy loss. Many distinct peaks in  $u_*$ ,  $Q_H$  and  $Q_E$  occurring during several of the cold-air events were removed by the applied despiking method. The peaks in  $Q_E$  on September 15 were caused by snowfall. Slightly cloudy conditions before September 15, and almost cloudless conditions afterwards were reflected in global radiation  $K\downarrow$  and downward longwave radiation  $I\downarrow$  (Fig. 3.1j). With almost no diffuse solar radiation, the shadow cast by Zeppelin mountain south of Ny-Ålesund showed shortly after noon by a strong decrease in  $K\downarrow$ .  $I\downarrow$  dropped significantly on September 15, along with terrestrial radiation  $I\uparrow$ , marking cooler atmosphere and surface temperatures. Before snowfall,  $K\downarrow$  was largely absorbed due to low albedo, leading to significant energy input at the surface at high solar angles, with peak net radiations  $Q_S^*$  of almost  $-200 \text{ W m}^{-2}$ . The high albedo under snow-covered conditions prevented significant energy uptake, leading to an almost

permanently positive  $Q_S^*$  after September 15.

The change in surface parameter patterns, which happened with the start of snow cover, can be attributed to local and regional effects known for this site: Cold-air events under snow-covered conditions can be clearly traced back to density-driven cold-air drainage from south to southwest, often showing higher wind speeds at 2 m agl than at 10 m agl and particularly strong temperature inversions. The increased dominance of southeast winds with onset of snow cover can be traced back to the channeled winds within Kongsfjorden, which are strongest under winter conditions (Maturilli et al., 2013). The SODAR wind statistics shown in Fig. D.3 confirm that the influence of wind channeling in the Brøgger valley ceased above 60 m agl to 90 m agl.

The clear contrasts in the measurements between snow-free and snow-covered conditions constituted an opportunity to investigate the impact of surface forcings on the lower troposphere in the recorded data.

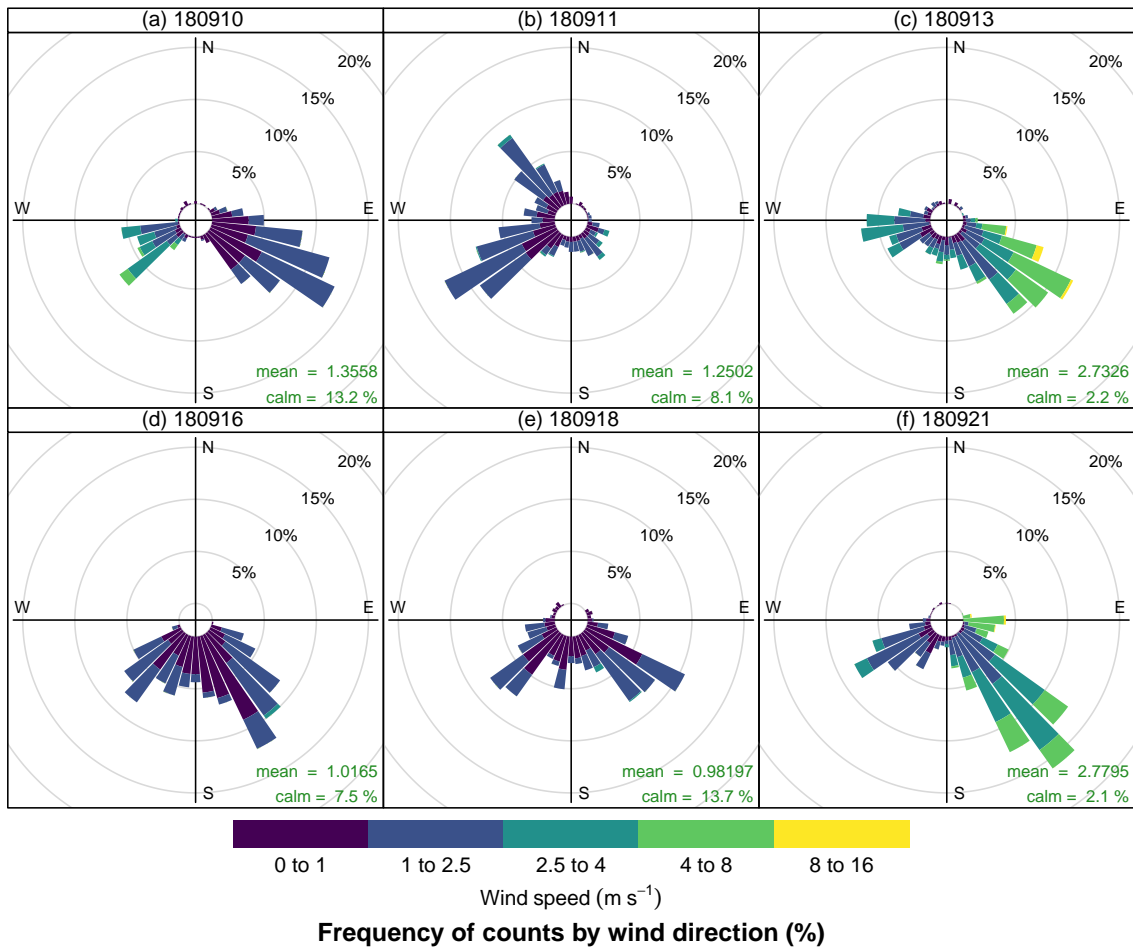


**Figure 3.3** Wind roses of winds at 10 m agl recorded on the BSRN tower for the measurement periods of the six fiber-optic experiments including 12 hours prior to their starts.

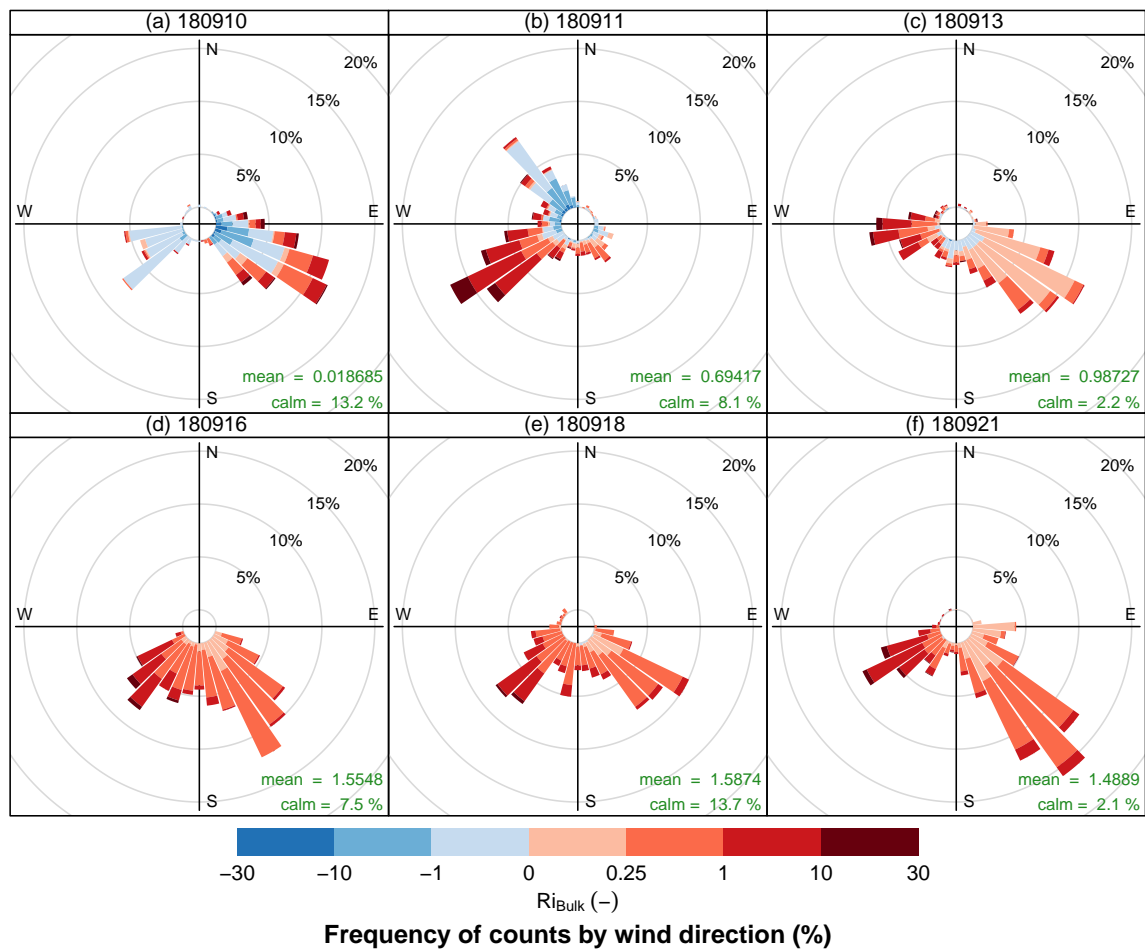


**Figure 3.4** Bulk Richardson number roses calculated with Eq. (2.13), using measurements at 2 m agl and 10 m agl on the BSRN tower for the measurement periods of the six fiber-optic experiments including 12 hours prior to their starts. Wind directions were measured at 10 m agl.

### 3.1.2. Synoptic forcing of conditions during fiber-optic experiments

Different resources were used to determine the synoptic forcing present during fiber-optic experiments, including BSRN tower and SODAR data recorded at the site, and reanalysis data revealing spatial synoptic patterns. This was necessary for the investigation of the impact of synoptic-scale characteristics on the observed vertical structure of the troposphere (see 3.7 and 3.8).

The local forcing of ABL properties on synoptic time scale was inferred from the observation of wind speed, wind direction and  $Ri_b$  in BSRN tower and SODAR data for the experimental periods plus the 12 hours prior to their starting time (Figs. 3.3-3.4). On these time scales, the local wind and dynamic stability differed significantly between the fiber-optic experiments, leading to the definition of four boundary-layer regimes (BLRs) which were later used to test the influence of surface-based forcings on the structure of the lower troposphere. These BLRs serve as an approximation of the local atmospheric conditions on a synoptic time scale, but do

not represent conditions during the fiber-optic experiments, since these experiments only lasted for a fraction of the period used to calculate the BLRs in most cases.

- The synoptic conditions of the 180910 experiment were characterized by strong winds from between 220 ° and 260 ° with neutral dynamic stability, and by more abundant weak winds from 80 ° to 140 ° with dynamic stability varying between unstable and supercritical  $Ri_b$  (Fig. 3.3a, Fig. 3.4a). Though the wind directions resemble those of 180913 and 180921, strongly different wind speeds and stability patterns led to 180910 receiving its own regime, BLR1.
- For 180911 weak winds mostly prevailed on the chosen synoptic time scale, with dominating directions between 230 ° and 260 °, and between 310 ° and 340 °, showing dynamically stable and unstable conditions, respectively (Fig. 3.3b, Fig. 3.4b). Since there was no other experiment with similar conditions, BLR2 was solely assigned to 180911.
- For both 180913 and 180921, strong winds originated from southeast, while weak to strong winds arrived from west and southwest, with directional lobes being around 50 ° wide (Fig. 3.3c,f). While southwest directions carried strongly dynamically stable air masses, the southeast directions showed weaker stability, judging from  $Ri_b$  (Fig. 3.4c,f). 180913 and 180921 were merged into the BLR3 regime owing to their distinct similarity of flow.
- 180916 and 180918 stood out by weak surface winds from between 100 ° and 260 °, with two not entirely separated density maxima around 240 ° and between 120 ° and 150 ° (Fig. 3.3d-e). The atmosphere was mostly dynamically stable at the surface, especially with winds from southwest (Fig. 3.4d-e). So, 180916 and 180918 was assigned to BLR4.

NCEP/NCAR reanalysis data (Kalnay et al., 1996) revealed spatial synoptic patterns surrounding the Svalbard archipelago (Fig. 3.5): On September 10 and 11 high pressure southeast and east of Svalbard, respectively, generated southwest and southeast winds, respectively, at the 850 hPa level, transporting warm air towards the archipelago. September 13 and 21 were characterized by low pressure southeast of Svalbard and significant horizontal pressure gradients, with northwest winds advecting cold air on September 13, and no temperature advection

**Table 3.1** Geopotential height  $h_{geo}$ , air temperature  $T$ , wind speed  $U$  and direction  $\phi$ , and vertical velocity  $\omega$  at 850 hPa level above Ny-Ålesund, partly with anomalies  $A$  relative to 1981-2010, taken from NCEP/NCAR reanalysis data (Kalnay et al., 1996), for the days with fiber-optic experiments.

Date	$h_{geo}$ (m)	$A_{h_{geo}}$ (m)	$T$ (°C)	$A_T$ (K)	$U$ (m s <sup>-1</sup> )	$\phi$	$\omega$ (mPa s <sup>-1</sup> )
Sep 10	1440	40 - 60	2 - 3	6 - 7	5	SW	25 - 50
Sep 11	1400 - 1420	20 - 40	2	6 - 7	3	SE	25
Sep 13	1360	0	-2 - -1	3 - 4	6	NW	25 - 50
Sep 16	1400 - 1420	60	-5 - -4	0	2 - 3	SE	25 - 50
Sep 18	1400 - 1420	40 - 60	-4 - -3	2 - 3	5 - 6	E	25 - 50
Sep 21	1340	0	-8 - -7	0	11 - 13	NE	75 - 100

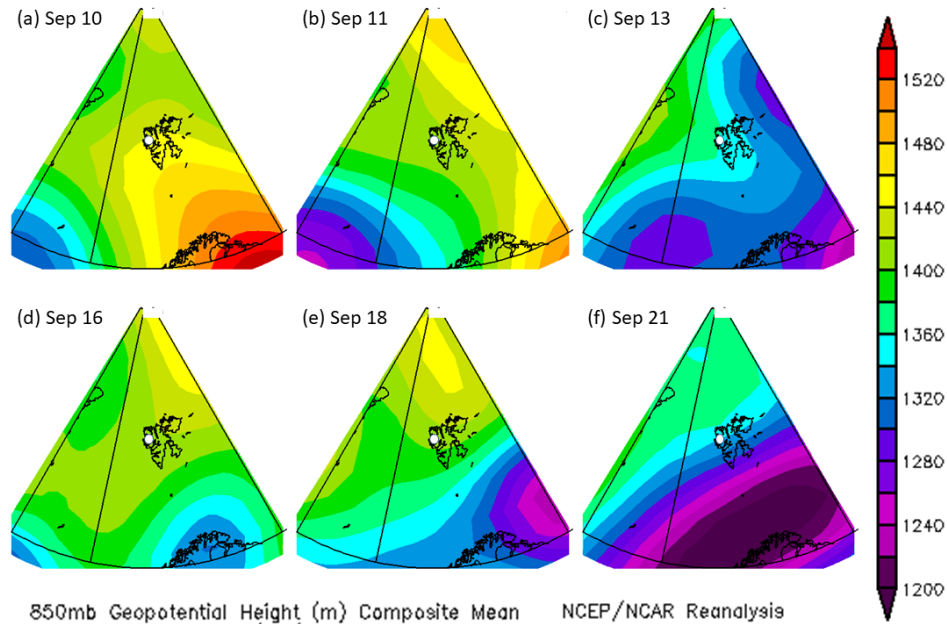


**Figure 3.5** Geopotential heights at 850 hPa level around Svalbard from NCEP/NCAR reanalysis for the days in 2018 with fiber-optic experiments, with the location of Ny-Ålesund marked. Geographical range of plots lies between 69 °N and 89 °N, and between 18 °W and 42 °E. Images were provided by the NOAA/ESRL Physical Sciences Laboratory, Boulder, Colorado, from their Web site at <http://psl.noaa.gov/>.

with northeast winds on September 21. Pressure fell towards southeast on September 16 and 18, leading to southeasterly and easterly winds, respectively, which did not reach more than  $3 \text{ m s}^{-1}$  at 850 hPa on September 16 and did not advect cold or warm air masses. Geopotential height and air temperature at 850 hPa were mostly higher than the reference period 1981-2010 (Tab. 3.1). The synoptic vertical velocity  $\omega$  showed slightly positive values for all days with fiber-optic experiments, indicating the presence of light subsidence.

Connecting the observed flow conditions to these spatial patterns on synoptic scale was only partly possible: The southwest wind on September 10 was present at 850 hPa and at the surface, and the neutral stability at the surface points to the synoptic, not katabatic origin of this airflow. All other wind directions in the BLRs are better explained by local forcings than by the spatial synoptic patterns at 850 hPa level, while mean wind speeds correlated well between reanalysis and BLRs (Pearson correlation = 0.78).

While the synoptic forcing governed wind speed, observed airflow at the site can be defined as autochthonous, as wind directions were strongly governed by surface features, particularly by channeling in Kongsfjorden and the Brøgger valley and katabatic winds strengthened by snow and ice cover (see 3.1.1).

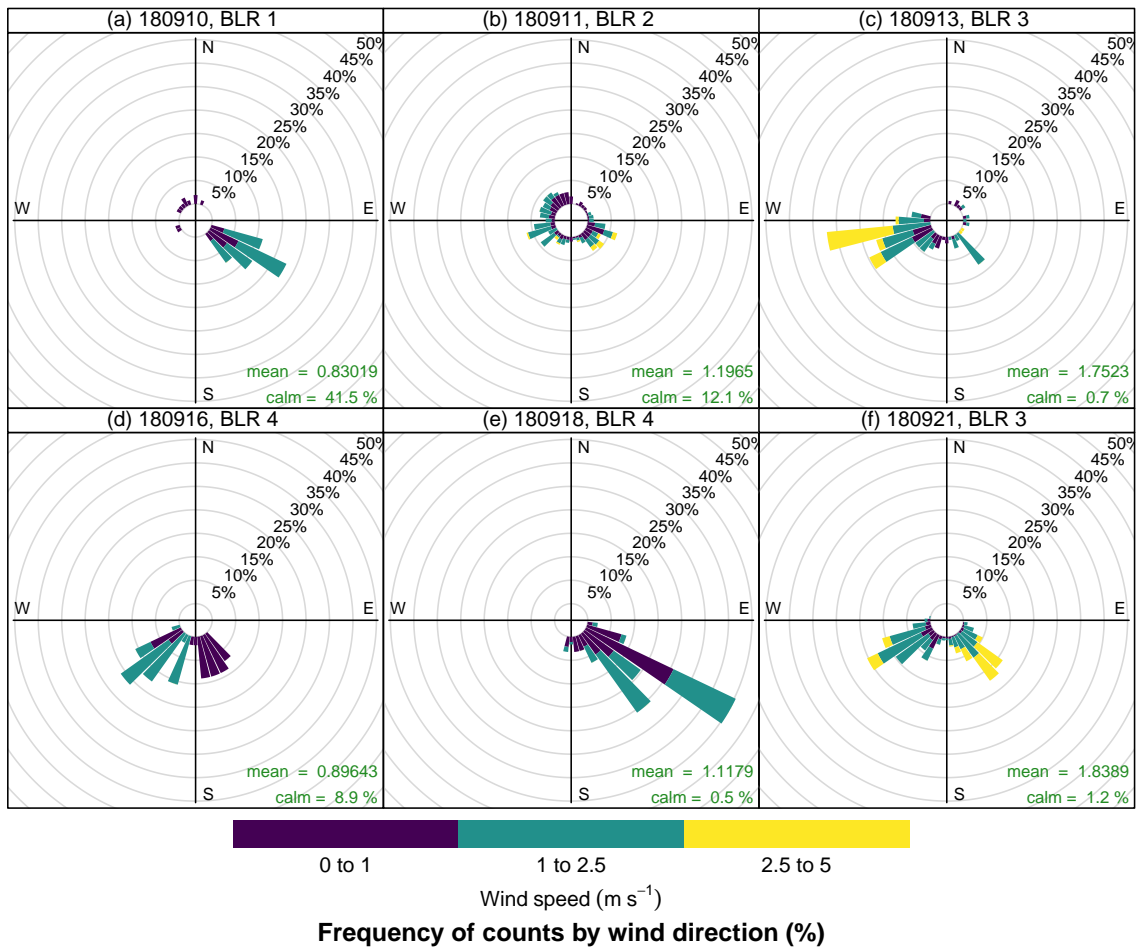


**Figure 3.6** Wind roses of winds at 10 m agl recorded on the BSRN tower for the measurement periods of the six fiber-optic experiments.

### 3.1.3. Conditions during fiber-optic experiments

Measurements taken during fiber-optic experiments are shown in this section to create a context for the observations in fiber-optic data discussed in later parts.

Wind directions during the experiments (Fig. 3.6) differed significantly for most experiments relative to those of the BLR definition periods (Fig. 3.3). For 180910 and 180918, winds at 10 m agl only arrived from  $110^\circ$  to  $140^\circ$  at the BSRN tower. At the same height and location, the southeast lobe of 180913 and 180921 was less dominant during experiments than for BLR periods, even hardly existent for 180913, while southwest directions were most abundant for these experiments with occurrence of strong winds. 180916 showed strong agreement between wind fields during and prior to the experiment. The clearest differences between experiment and BLR periods were found for 180911, where the prominent southwest and northwest lobes of the BLR period did not appear during the experiment, were almost omnidirectional winds with partly strong wind speeds from southeast were observed.

Differences between wind directions at 10 m agl and 2 m agl were only significant for 180918

and 180921, where southeast winds at 10 m agl were turned clockwise by more than  $20^\circ$  at 2 m agl, with wind speeds exceeding those at 10 m agl by  $0.3 \text{ m s}^{-1}$  for 180916. This directional shift indicates the occurrence of distinct shallow cold-air drainage from south or southwest during these three experiments. However, the dynamic stability of the advected air masses at the BSRN tower during the experiments was almost equal to that of the BLR periods (Fig. 3.4) for the same wind directions, with the exception of 180921, where a significant portion of northwest winds carried dynamically stable air during the experiment.  $Ri_b$  were supercritical for most of the experiment periods, with experiment averages between 0.61 and 1.97.

East and southeast winds were consistently found in SODAR data in the lowest 250 m agl for the last four experiments (Fig. 3.7). Weak winds from southerly to westerly directions frequently occurred in the lowest 100 m agl and 60 m agl for 180913 and 180921, respectively. 180913 and 180918 showed similar velocities rarely exceeding  $3 \text{ m s}^{-1}$ , while 180916 and 180921 reached more than  $4 \text{ m s}^{-1}$  at many measurement heights above 100 m agl.

Above the height where SODAR data were available horizontal wind speed measurements were only taken by the tether sondes at the top of the fiber-optic profiles. There, wind speeds averaged  $3.8 \text{ m s}^{-1}$  and  $3.4 \text{ m s}^{-1}$  at 800 m agl for 180913 and 180918, respectively, which was clearly exceeded by 180911 and 180921, with  $7.6 \text{ m s}^{-1}$  and  $5.4 \text{ m s}^{-1}$ , respectively, at around 600 m agl. Lower tether sonde speeds were recorded for 180910 and 180916, with  $2.0 \text{ m s}^{-1}$  at

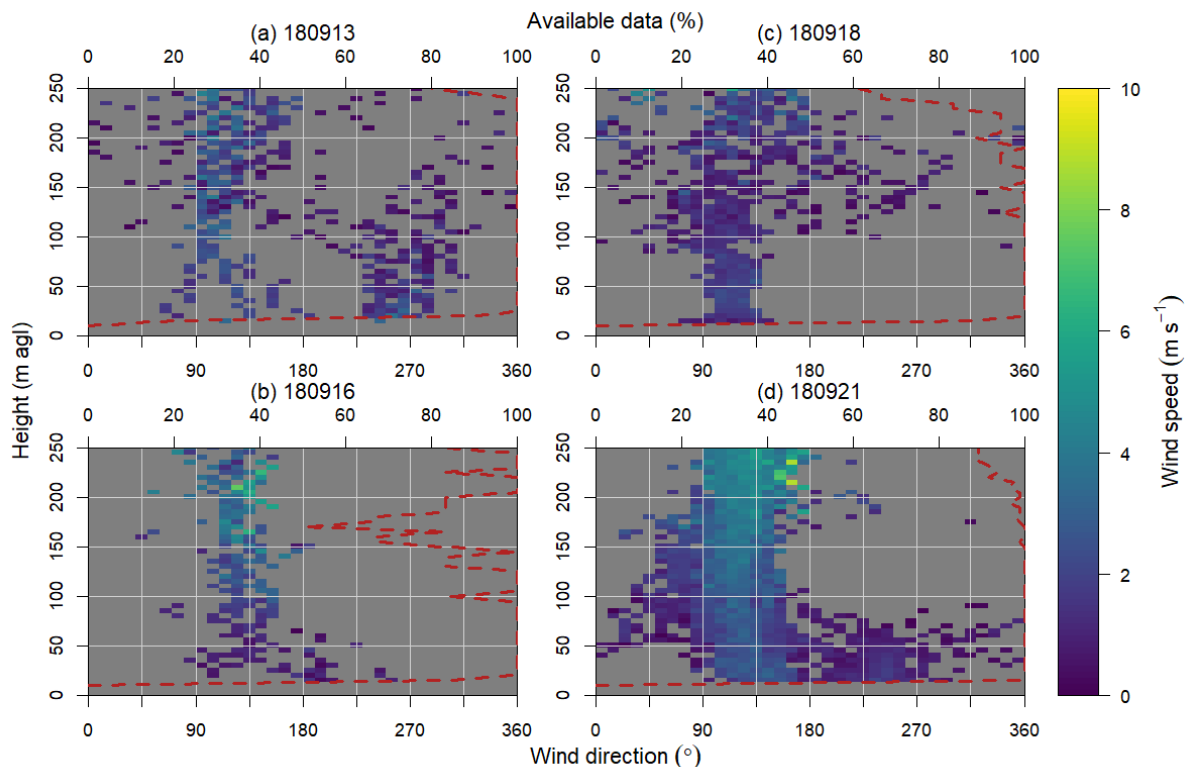


**Figure 3.7** Mean horizontal wind speeds depending on wind direction and height, taken from SODAR measurements for the measurement periods of the last four fiber-optic experiments. Broken red line denotes percentage of available data for each height bin.

450 m agl and  $2.5 \text{ m s}^{-1}$  at 100 m agl, respectively.

Variability of tethersonde wind speeds between experiments largely corresponds to wind speeds observed in reanalysis data (Tab. 3.1). Only for 180911, the pattern clearly disagrees, since reanalysis yielded a very low wind speed at 850 hPa level, while strongest winds across experiments were observed by the tethersonde. This indicates a distinct wind maximum below the 850 hPa level, which was confirmed by a radiosounding launched on September 11 at 16:49 UTC (see Fig. D.13).

Friction velocity  $u_*$  repeatedly exceeded  $0.1 \text{ m s}^{-1}$  coinciding with southwest winds at the EC station (Fig. 3.8). The highest  $u_*$  however, was observed during 180911 with a mean of  $0.11 \text{ m s}^{-1}$  were maximum values were associated with various directions. For 180910 and 180918 experiments,  $u_*$  remained below  $0.1 \text{ m s}^{-1}$ . Southeast winds, which were much less abundant in the EC data than at the BSRN tower, mostly also showed  $u_*$  values below this threshold.

Averaged over experiments,  $Q_H$  ranged from  $-16 \text{ W m}^{-2}$  for 180921 to  $-3 \text{ W m}^{-2}$  for

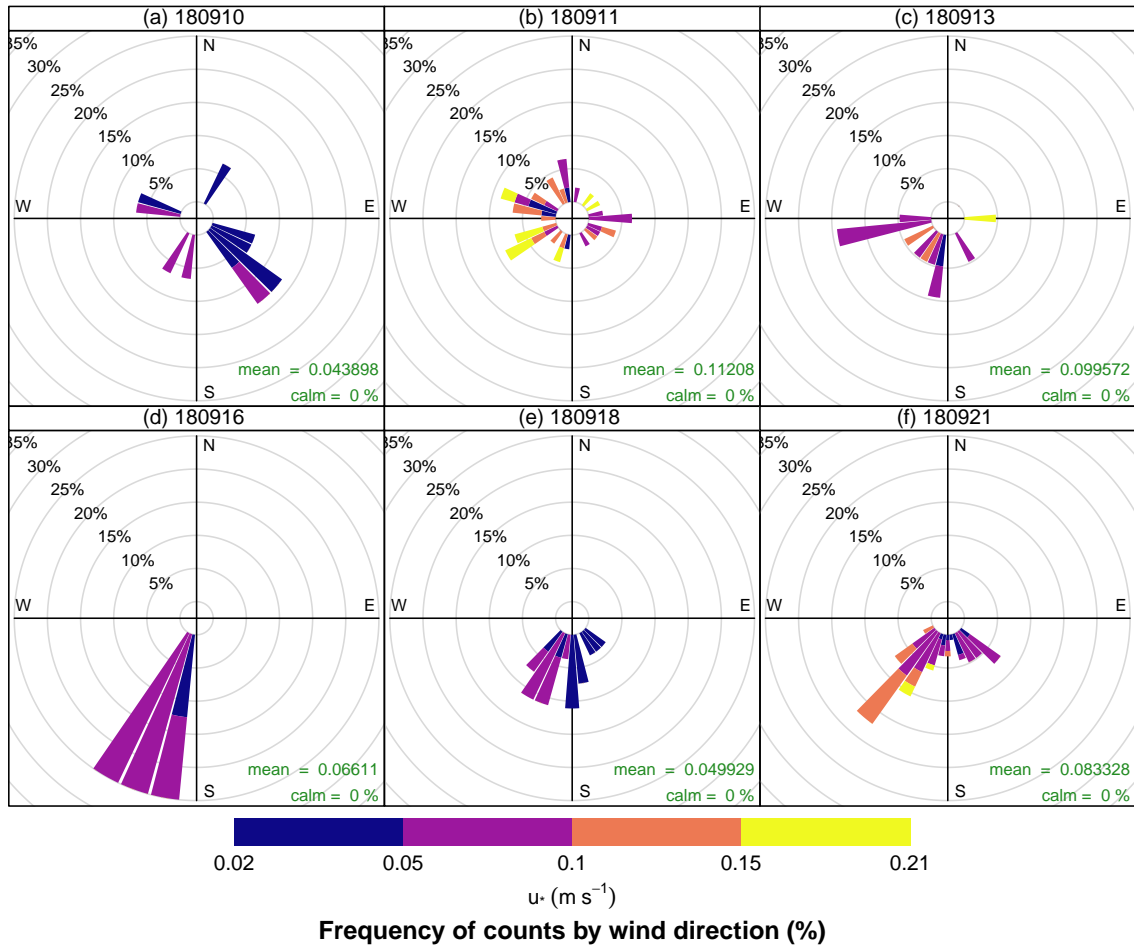


**Figure 3.8** Rose plots of friction velocity  $u_*$  at 2 m agl from measurements by the EC system for the periods of the six fiber-optic experiments.

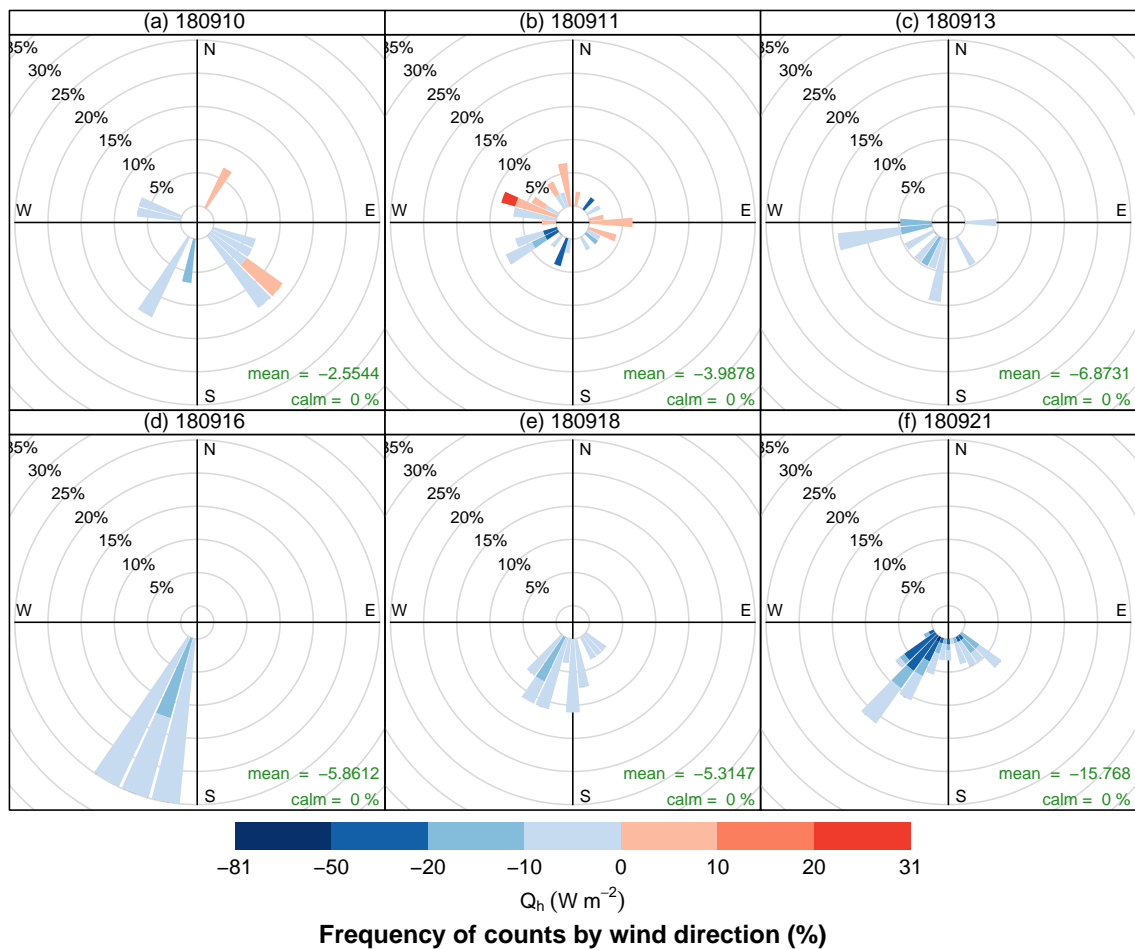


**Figure 3.9** Rose plots of sensible heat flux  $Q_H$  at 2 m agl from measurements by the EC system for the periods of the six fiber-optic experiments.

180910 (Fig. 3.9). However, averages may not be similar between experiments because significantly more positive  $Q_H$  values were excluded during the last three experiments with snow cover.  $Q_H$  below  $-20 W m^{-2}$  were mostly found for southwest winds at the EC station during experiments 180911 and 180921.

### 3.2. Overview of thermodynamic structure in fiber-optic profiles

Fiber-optic data from IceFOX were used to provide an overview of the thermodynamic structure of the lower troposphere observed during the flights via wavelet-filtered  $\theta_v$  and its standard deviation in time  $\sigma_{\theta_v}$ , and via  $LSS$ . Virtual potential temperatures  $\theta_v$  were available from the surface to the maximum height of the IceFOX profiles, where the surface at a height of 0 m agl corresponded to the platform of the AWIPEV balloon house. For the lowermost and uppermost 10 m of the profile, no  $LSS$  could be calculated (see 2.2.4). Patterns in  $\theta_v$  were then compared with the occurrence of LIs in the fiber-optic profiles.

All fiber-optic experiments exhibited layers with distinct increase in  $\theta_v$  with height of 0.5 K

to 6 K between the surface and 20 m agl to 50 m agl averaged over the entire measurement periods (Fig. 3.10). These layers contained the maximum  $LSS$  values in instantaneous fiber-optic profiles, reaching up to  $0.34 \text{ K m}^{-1}$ . Temporal  $\sigma_{\theta_v}$  also peaked within these layers for all experiments, spanning from 0.4 K to 1.3 K computed over entire experiment duration. Here,  $\sigma_{\theta_v}$  values above 1 K only occurred for experiments conducted under snow-covered conditions. For blocks with a duration of 30 min,  $\sigma_{\theta_v}$  reached up to 1.6 K at the surface. Observed thermodynamics indicate very stable atmospheric conditions close to the surface for most experiments.

The thermodynamic structures exhibited continuous increase in  $\theta_v$  with height for all flights (Fig. 3.10), but varied significantly above 50 m agl between experiments: A much steeper increase in  $\theta_v$  with height across the profiles was observed for 180913 and 180918 than for the other experiments (Fig. 3.10). Further, 180913 and 180918 showed a clearly defined thermodynamic structure, where some profile sections exhibited distinct LIs corresponding to peaks in  $\sigma_{\theta_v}$  which were less pronounced for the other experiments. Over the entire experiment periods  $\sigma_{\theta_v}$  reached up to 0.6 K above 50 m agl, but values were lower than at the surface. The very pronounced thermodynamic structure for 180913 and 180918 can be explained by more stationary conditions and increased atmospheric stability across the profiles relative to the other experiments.

The agreement between temperature inversions and peaks in  $\sigma_{\theta_v}$  was investigated by comparing  $\sigma_{\theta_v}$  to the ratio of temperature inversions in instantaneous profiles at each measurement height across time  $x_{I,h}$ , where temperature inversions are defined as  $LSS > 0.01 \text{ K m}^{-1}$ . No clear relationship between  $x_{I,h}$  and  $\sigma_{\theta_v}$  was evident for most experiments when comparing bulk

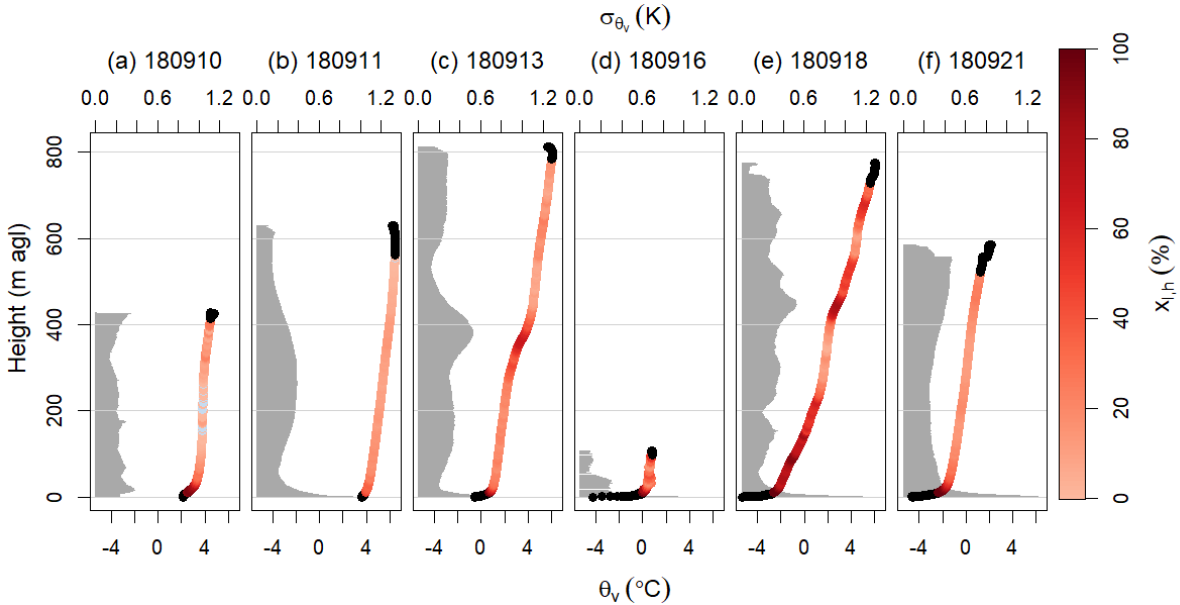


**Figure 3.10** Temporal statistics of virtual potential temperatures  $\theta_v$  from all fiber-optic experiments, calculated with a resolution of 20 s. Points show mean  $\theta_v$ , with colors denoting the ratio of temperature inversions at each measurement height across time  $x_{I,h}$ , where temperature inversions are defined as local static stability  $LSS > 0.01 \text{ K m}^{-1}$ . Blue points represent no occurrence of temperature inversions, black points indicate heights with  $LSS$  availability of less than 95% where no  $x_{I,h}$  was calculated. Gray surface shows standard deviation  $\sigma_{\theta_v}$ .

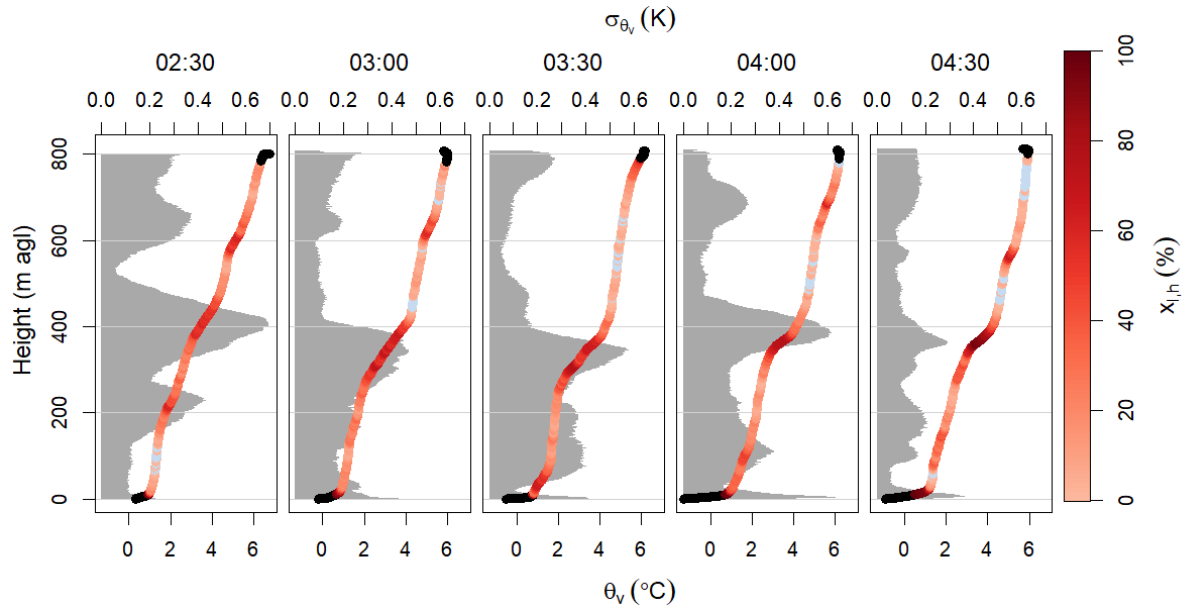


**Figure 3.11** Temporal statistics of virtual potential temperatures  $\theta_v$  as shown in Fig. 3.10, but only from 180913 experiment in time blocks of 30 min length. Start time of each block is indicated above the plots in UTC.

temporal statistics across entire experiments (Fig. 3.10a,b,d,f). However,  $\sigma_{\theta_v}$  was positively correlated with  $x_{I,h}$  for data blocks with a duration of 30 min representing a more stationary thermodynamic structure in the profiles, where the majority of distinct maxima in  $\sigma_{\theta_v}$  corresponded to high  $x_{I,h}$ , indicating an abundant presence of SIs and LIs across fiber-optic profiles. Figure 3.11 illustrates this connection between peaks in  $\sigma_{\theta_v}$  and peaks in  $x_{I,h}$  for 180913, where a distinct maximum in  $\sigma_{\theta_v}$  oscillated around 400 m agl that corresponded to a maximum in  $x_{I,h}$  revealing a deep LI. Only one distinct  $\sigma_{\theta_v}$  peak without an according peak in  $x_{I,h}$  was found, which occurred during 180911 between 17:00 UTC and 17:30 UTC and between 50 m agl and 500 m agl, with maximum  $\sigma_{\theta_v}$  at 200 m. This feature could be explained by cold air being advected through the lowest 500 m of the profile and a subsequent distinct warming above 100 m agl within this period (see Fig. D.8a). These observations show that temperature variability within the fiber-optic profiles was closely connected to the presence of SIs and LIs in most cases.

Fiber-optic atmospheric profiles of thermodynamics exhibited a distinct vertical structuring, with temperature inversions separating layers with weaker static stability. In the following sections, this structure is more closely analyzed using results of the layer detection and focusing on specific phenomena observed in the recorded data.

### 3.3. Detected sublayers and surface-based inversions

Local static stability  $LSS$  calculated from fiber-optic data was used to detect sublayers, divided into ILs and NILs, and to define the SI (see 2.4). Since  $LSS$  was not available in the lowermost and uppermost 10 m of the profiles due to computational reasons, sublayers were neither defined in these height ranges, and SIs with lower thickness than 10 m could not be detected. Since

**Table 3.2** Bulk statistics of sublayer detection for each experiment, including temporal ratio of detection of a surface-based inversion (SI)  $x_{\text{SI}}$ , median and standard deviation, respectively, of SI height  $h_{\text{SI}}$ , ratio of bins showing temperature inversions  $x_{\text{I}}$ , ratio of inversion layers (ILs)  $x_{\text{IL}}$ , and mean number of ILs in the column in instantaneous profiles  $n_{\text{IL,rel}}$ .

Experiment	$x_{\text{SI}}$ (%)	$h_{\text{SI}}$ (m)	$\sigma_{h_{\text{SI}}}$ (m)	$x_{\text{I}}$ (%)	$x_{\text{IL}}$ (%)	$n_{\text{IL,rel}}$
180910	87.9	36.5	16.4	15.3	14.5	1.6
180911	43.2	45.0	30.7	12.7	5.8	0.7
180913	98.2	23.5	16.1	24.3	20.1	3.5
180916	100.0	24.0	7.0	40.7	35.4	1.2
180918	100.0	107.0	56.2	45.6	46.0	3.4
180921	100.0	38.8	19.3	21.4	15.2	2.0

ILs and SIs were yielded from different detection routines, they partly overlapped where an IL could be part of the SI and the SI could contain multiple LIs. In this section, an overview of the characteristics of ILs, NILs, and SIs resulting from the detection algorithms is provided.

A SI was detected for the majority of data for all experiments except 180911 (Tab. 3.2). For the three experiments with snow-covered conditions, the SI lasted throughout the measurement periods. Median SI heights  $h_{\text{SI}}$  varied by a factor of 5 between the experiments, where 180918 stands out with a median  $h_{\text{SI}}$  of more than 100 m agl, which even exceeded 200 m agl at single time steps (Tab. 3.2, Fig. 3.12).

Bulk statistics of temperature inversions and detected ILs provide a first insight into results of the layer detection: The ratio of temperature inversions  $x_{\text{I}}$ , defined as percentage of  $LSS > 0.01 \text{ K m}^{-1}$  in the data, differed significantly between experiments (Tab. 3.2). Ratio of data assigned to ILs  $x_{\text{IL}}$  was lower than  $x_{\text{I}}$  for most experiments, illustrating that temperature inversions were more frequently integrated into NILs than  $LSS < 0.01 \text{ K m}^{-1}$  were assigned to ILs. Atmospheric profiles showed between 0.7 and 3.5 ILs in the vertical column averaged over experiments, which separated the remaining atmosphere into NILs (Tab. 3.2). These statistics underline differences in the thermodynamic structure of the fiber-optic profiles between experiments, where multiple ILs and NILs were present particularly during 180913 and 180918, and weaker stability prevailed during 180910 and 180911.

The distribution of ILs across the fiber-optic profiles was investigated for patterns corresponding between experiments. Most frequent occurrence of ILs and highest  $LSS$  was observed in the SI for all experiments (Fig. 3.12). Above the SI,  $LSS > 0.05 \text{ K m}^{-1}$  was rarely observed. Despite clear differences in thermodynamic structure between the experiments, some height ranges within the profiles outside the SI were more dominated by ILs than others: Between 350 m agl and 500 m agl, an increased number and duration of ILs relative to other heights was observed for all experiments, corresponding to an elevated ratio of  $LSS > 0.01 \text{ K m}^{-1}$  (Fig. 3.12). Centered around 650 m agl to 700 m agl, a similar yet less distinct accumulation of stably-stratified conditions was found for 180913 and 180918, the only experiments with measurements this high above the ground. Most even distributions of ILs across the profiles were observed for 180911 and 180921 compared to the other experiments which can be explained by the long recording periods (see 3.2). While the amount of data available is not sufficient to draw statistically mean-

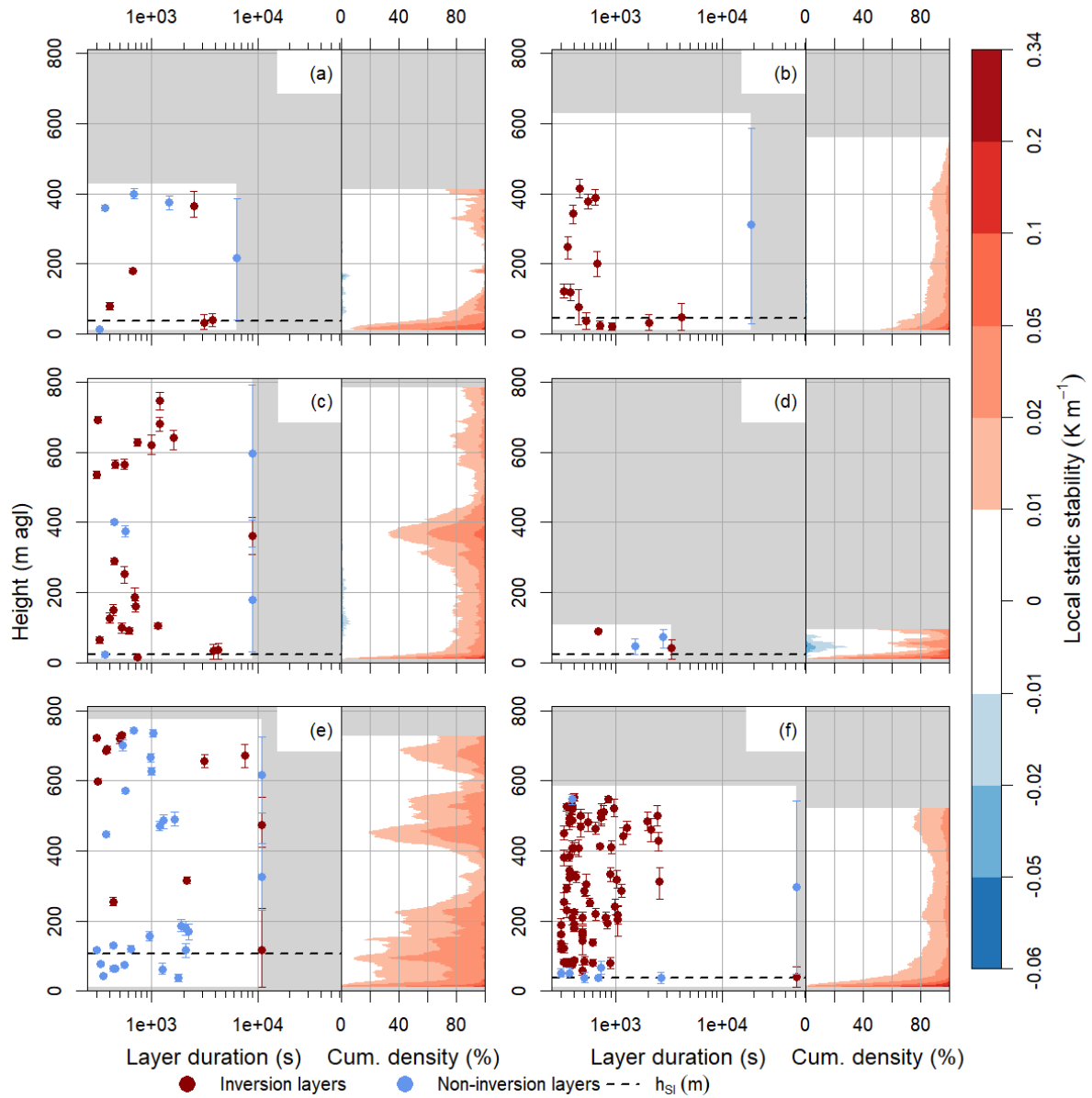


**Figure 3.12** Duration and thickness of detected sublayers for (a) 180910, (b) 180911, (c) 180913, (d) 180916, (e) 180918, and (f) 180921. Points and bars denote mean height and height range of each sublayer, respectively, all averaged over the entire layer duration. Spatial and temporal ranges outside the experiments are marked by gray surfaces. Median surface-based inversion height  $h_{SI}$  is included for each experiment. Cumulative probability density of local static stability ( $LSS$ ) classes is added for each height bin with data availability higher than 95 %.

ingful climatological conclusions, the pronounced maximum in IL occurrence between 350 m agl and 500 m agl may be a typical feature in the lower troposphere above Ny-Ålesund, since it corresponds to the height of the surface-based layer affected by wind channeling along Kongsfjorden (Esau and Repina, 2012; Maturilli and Kayser, 2017).

Observed thickness and duration of ILs were explored, where ILs located entirely above median  $h_{SI}$  of a flight were distinguished from ILs which were at least partly located within the SI, i.e., below the median  $h_{SI}$ . Mean duration of ILs above and within the SI was 15 min and 94 min, respectively (Fig. 3.12). This observation indicates that very stable conditions were more consistently present at the surface which can be explained by the strong forcing by radiative cooling of the surface, while the atmosphere above the SI showed a far higher horizontal heterogeneity, leading to shorter duration of ILs there. Mean thickness of ILs averaged to 39.5 m, and ranged between 10 m and 100 m for most ILs, where mean layer thickness was not related to mean layer height. Mean duration of ILs above the SI differed distinctly between experiments and ranged between 7 min and 11 min for 180911, 180916 and 180921, and between 18 min and 40 min for 180910, 180913 and 180918. Three ILs above the SI observed for 180913 and 180918 stood out, since they lasted for more than 1 hour and reached mean thicknesses of more than 50 m. While the short duration of ILs for 180916 was due to the short recording period of the experiment, the differences in IL duration between the other flights are assumed to represent true differences in horizontal heterogeneity of atmospheric profiles.

Mean thickness and duration of NILs was 73.2 m and 53.7 min, respectively, making them both deeper and longer-lived than ILs on average. This high duration and thickness was NILs with average thickness of more than 200 m lasted over the entire duration for all experiments, spanning the entire atmospheric profiles above the SI for 180910, 180911 and 180921, and separated by long-lived ILs for 180913 and 180918. These deep NILs expanded across spatiotemporally discontinuous LIs for 180911, and partly for 180913 and 180921. This issue occurred because such discontinuous LIs were only partly defined as individual short-lived ILs by the layer detection algorithm, which were discarded due to their layer duration of less than 5 min. This limitation of the algorithm precludes meaningful interpretations of the deep long-lived NILs for 180911, 180913 and 180921. The deepest meaningful long-lived NIL was found for 180910 above the SI, and can be viewed as a residual layer of a dynamically mixed layer that had developed under significant wind shear in the previous hours (see Fig. 3.1b,g), and diminished in height across the experiment period. Statistics of NILs are distorted by the presence of unphysical deep and long-lived NILs showing that the layer detection algorithm was more successful at detecting ILs than NILs.

A positive correlation between mean thickness and duration of sublayers existed independently of their classification (Fig. 3.13c). Sublayers thinner than 20 m rarely lasted longer than 15 min. At layer thickness between 20 m and 100 m the observed layer duration increased with thickness. Sublayers with greater thickness than 100 m did not show such a clear positive relationship between thickness and duration. This was caused by the limited measurement periods, suggesting that the positive relationship also exists for thicknesses greater than 100 m. As mentioned above, NILs with thickness of more than 200 m and lifespan of more than 2 hours were merged inadequately by the sublayer detection algorithm across temperature inversions and cannot be meaningfully interpreted. The positive correlation between thickness and duration suggests that thicker sublayers moving through the profile showed a larger horizontal extent than thinner sub-

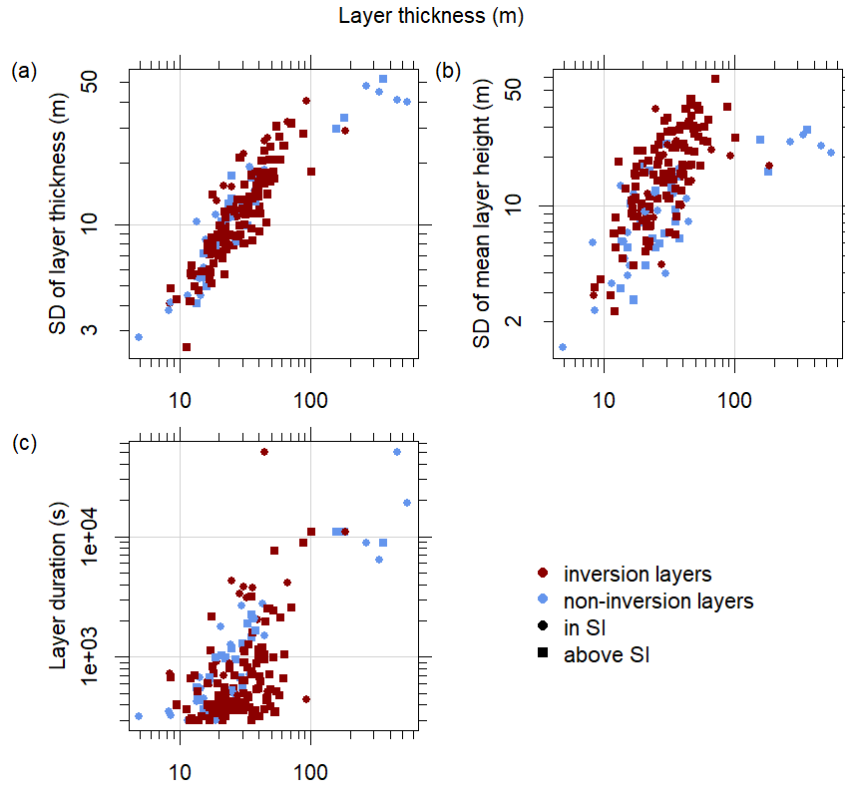


**Figure 3.13** Scatter plots of (a) standard deviation of thickness, (b) standard deviation of mean height, and (c) duration against average thickness for all detected sublayers. Layer thickness is here defined as total vertical extent of measurement bins belonging to a sublayer. Differentiation between sublayers reaching below the median surface-based inversion height at any time (“in SI”) and sublayers that remain above this height at all times (“above SI”) is included.

layers. It is unlikely that the differing lifetime of sublayers was due to ubiquitous mixing causing thinner sublayers to vanish, since the observed stable conditions preclude this from happening.

At layer thicknesses of less than 100 m, thickness showed significant positive linear relationships to its standard deviation (linear regression: Slope = 0.38,  $R^2 = 0.78$ ,  $p < 0.001$ , Fig. 3.13a), and to the standard deviation of the spatial mean layer height (linear regression: Slope = 0.47,  $R^2 = 0.44$ ,  $p < 0.001$ , Fig. 3.13b). At greater layer thicknesses than 100 m, these two relationships became nonlinear, which may not represent a true physical connection due to the issues with sublayer definition mentioned above. The positive correlations between variability in thickness and mean elevation, respectively, and layer thickness cannot be traced back to the mere elevation of sublayers, since there was no relationship between layer thickness and layer height.

### 3.4. Variability of the surface-based inversion

Dynamics within the SI and their variability were investigated more closely by means of fiber-optic data and results of the SI and sublayer detection. Parameters mainly investigated in this section are  $\theta_v$ ,  $U$  and  $Ri$  from fiber-optic profiles, and ancillary wind data from SODAR and

BSRN tower. Note that no analysis in this thesis was directly aimed at defining characteristics of the stable boundary layer (SBL), but the detected SIs may serve as a proxy for the SBL.

### 3.4.1. Overview of dynamics

Simultaneous observations of wind profiles and temperature profiles at a resolution of 5 m and 10 s to 20 s were enabled by the implementation of FireFOX for 180916, 180918 and 180921. These data allowed for investigation of dynamics and thermodynamics, and for the computation of Richardson number  $Ri$  to assess the dynamic stability within the SI. An overview of all combined instantaneous fiber-optic wind and temperature profiles is provided in Figs. D.4-D.6. Here, fiber-optic wind profiles were only analyzed for 180916 and 180921, since wind speeds from 180918 showed distinct non-correctable artifacts, additional to the low data availability due to artifacts induced by cable holders and entangled fibers. The SI was entirely captured by these profiles, with median  $h_{SI}$  of 24.0 m agl and 38.8 m agl for 180916 and 180921, respectively.

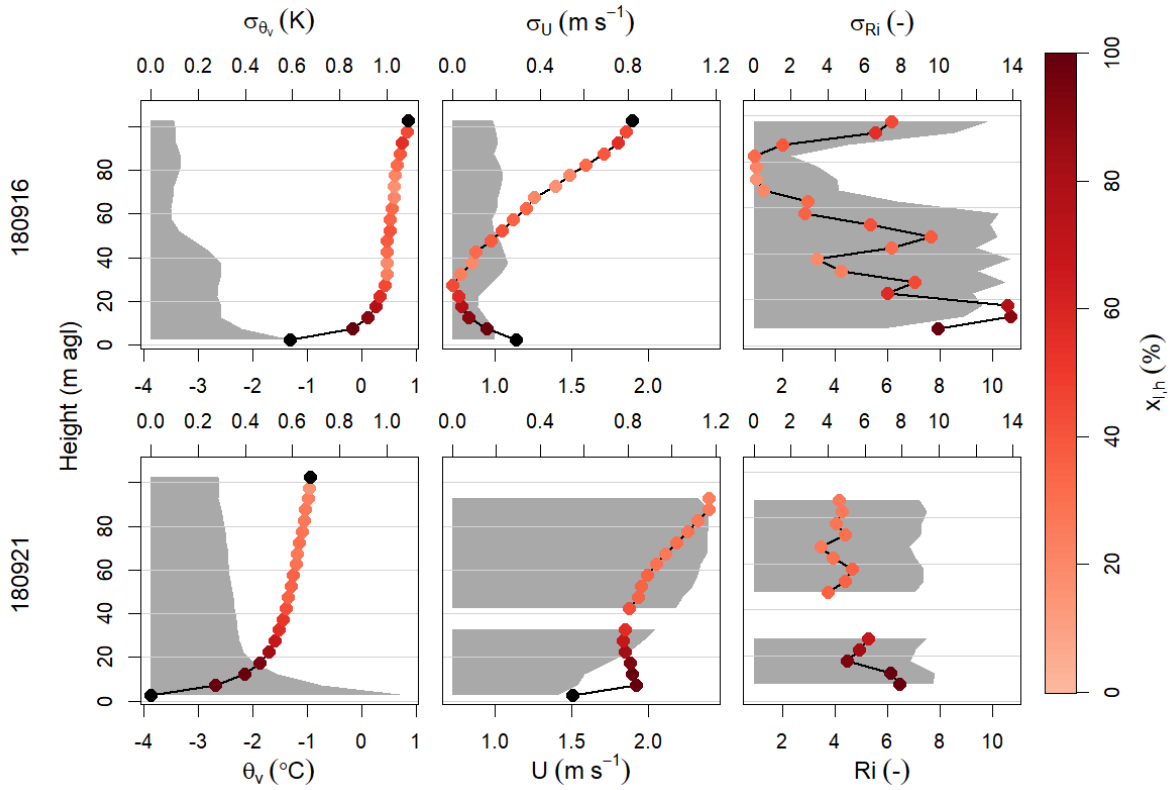


**Figure 3.14** Temporal statistics from the fiber-optic experiments 180916 and 180921, calculated with a resolution of 20 s. Virtual potential temperatures  $\theta_v$  are taken from IceFOX, and wind speeds  $U$  and simplified Richardson numbers  $Ri$  from FireFOX in the height range of the FireFOX experiments. Points show averages, with colors denoting the ratio of temperature inversions at each measurement height across time  $x_{I,h}$ , where temperature inversions are defined as local static stability  $LSS > 0.01 \text{ K m}^{-1}$ . Black points indicate heights with  $LSS$  availability of less than 95 % where no  $x_{I,h}$  was calculated. Gray surfaces show standard deviations. Any  $|Ri| > 30$  was set to 30 before calculating statistics. Only statistics at heights with data availability of more than 60 % are shown.

Profiles of horizontal fiber-optic wind speed  $U$  showed similar patterns for 180916 and 180921: Both experiments exhibited a  $U$  maximum in the lowermost meters which was most pronounced for 180916, with a wind speed difference of  $1 \text{ m s}^{-1}$  averaged over the entire experiment (Fig. 3.14). This peak in  $U$  close to the surface was bounded by a minimum in  $U$  at 30 m agl, above which  $U$  increased with height. The height range of these surface maxima corresponded to peaks in temporal  $\sigma_{\theta_v}$ , and to almost continuously present SIs, as indicated by  $x_{I,h}$  of more than 80 %. The flow responsible for these surface wind maxima originated from south to southwest, as this wind direction appeared in similar height ranges in SODAR data (Fig. 3.7b,d).

Standard deviation of fiber-optic wind speed  $\sigma_U$  remained nearly constant with height at  $0.9 \text{ m s}^{-1}$  for 180916, but increased by a factor of 1.6 between surface and 90 m agl to nearly  $2.5 \text{ m s}^{-1}$  for 180921. The uniformly low  $\sigma_U$  of 180916 can be explained by more stationary wind fields during the short period, while wind speeds varied strongly across 180921 within the lowermost 60 m agl (Fig. 3.7b,d).

Average  $Ri$  calculated from fiber-optic data lay above the critical value of 0.25 at all heights, and corresponding  $\sigma_{Ri}$  showed very similar values to the mean  $Ri$ . Because of very low wind speeds and wind shear  $Ri$  often showed values many orders of magnitude higher than the typically discussed range of up to  $10^1$ . Thus, all  $|Ri| > 30$  were set to 30 before calculating statistics. This approach avoided dropping a majority of the data but decreased variation in  $Ri$  averages and standard deviations which were influenced by the high abundance of  $Ri = 30$ . The high  $\sigma_{Ri}$  illustrates that subcritical  $Ri < 0.25$  existed even within very stable parts of the SI.

Over the 14-hour period of 180921 mean and standard deviation of  $Ri$  showed values of around 5 and 9, respectively, which was almost uniform with height in the lowest 100 m agl. (Fig. 3.14). On a 30-min scale 2.3 % of computed  $Ri$  values within the lowest 100 m agl were subcritical,

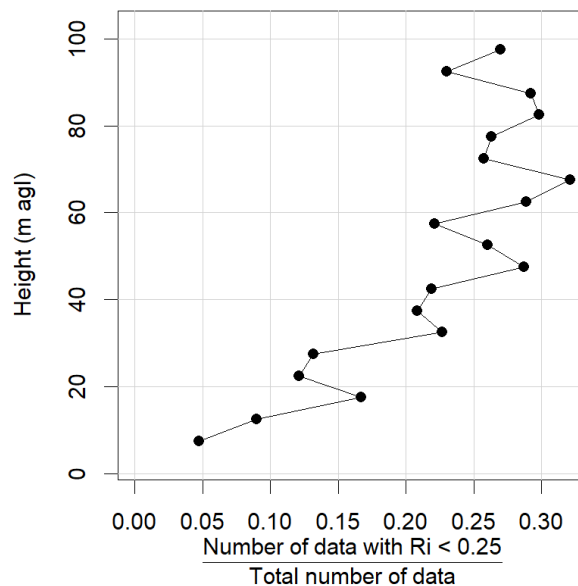


**Figure 3.15** Fraction of Richardson number  $Ri < 0.25$  in  $Ri$  calculated from fiber-optic temperatures and wind speeds during 180921 at a temporal resolution of 20 s.

which were located at different levels, but not including the lowest measurement height at 7.5 m agl. Subcritical  $Ri$  values could be observed more frequently in instantaneous 20-s data: A ratio of 5 % of  $Ri$  values at the lowest measurement bin height of 7.5 m agl were subcritical for 180921, and this ratio increased with height up to 68 m, where it reached 32 % (Fig. 3.15). Subcritical  $Ri$  under very stable conditions have been observed in several experiments and are connected to intermittent turbulence production (e.g. Mahrt, 1987; Sun et al., 2012; Grachev et al., 2013).

### 3.4.2. Influence of wind directions on thermodynamics

Spatiotemporal variability in fiber-optic  $\theta_v$  within the detected SIs was analyzed for all flights with respect to the influence of wind directions. To this end, standard deviation of  $\theta_v$  within the SI  $\sigma_{\theta_v,SI}$  was calculated for 10-min periods between the surface and the respective medians of  $h_{SI}$  for each experiment, and wind directions representing footprints were taken from BSRN tower data at 10 m agl. 180911 was neglected in this analysis because of the low  $x_{SI}$  observed there. Average  $\sigma_{\theta_v,SI}$  of 0.5 K were found for experiments without snow cover, which were greatly exceeded by values of 0.9 K to 1.0 K for experiments recorded under snow-covered conditions (Fig. 3.16). Southwest winds were related to higher  $\sigma_{\theta_v,SI}$  than southeast winds, reaching values of more than 1.5 K for 180921 (Fig. 3.16b,e). A general statement about the influence of northerly or northwesterly winds on  $\sigma_{\theta_v,SI}$  was difficult to make, since they were rarely observed. For 180910, northwest winds showed lower  $\sigma_{\theta_v,SI}$  than southeast winds (Fig. 3.16a). These observations indicate that the presence of snow cover increased variability in thermodynamics in the SI. The presence of southwest winds at the surface under snow-covered conditions was connected to highest temperature variability.

Here, instantaneous fiber-optic  $\theta_v$  data were used to illustrate the cause for high variability in thermodynamics in the SI coinciding with southwest winds: Along with south and southwest winds, cold-air events were recorded in the SI close to the surface. Fiber temperatures in the lowest meters above ground level dropped during these events by up to more than 2 K and 4 K for experiments without and with snow cover, respectively. These cold-air events caused significant temperature changes typically in the lowest 10 m agl to 20 m agl, for single events even up to more than 50 m agl, and lasted between few minutes and more than 1 hour (e.g. Fig. 3.17). These cold-air events can be defined as cold-air drainage flows. In some cases, particularly at low wind speed, they were only affecting the lowest 10 m agl. At higher wind speeds, shallow cold airflow was embedded within a deeper southwest flow between the surface and 60 m agl to 90 m agl (e.g. Fig. 3.17) with weaker or absent cold-air advection above 20 m agl. This deep flow was particularly observed under snow-covered conditions (Fig. 3.2). This suggests two origins of cold-air advection from south and southwest: (1) Very shallow cold-air advection was related to cold-air drainage from the mountain slopes directly south and southwest of Ny-Ålesund, and (2) deep southwest flow was generated by katabatic outflow from the Brøgger valley and glaciers with absence of strong winds from southeast. Since the shallow cold-air drainage from south and southwest caused the strongest temperature variability (Fig. 3.14), it was the dominating reason for high  $\sigma_{\theta_v,SI}$  associated with these wind directions.

Variability in wind speed and direction from fiber-optic and SODAR was connected to vertical displacement of ILs within the SI in multiple cases where stably-stratified air masses appeared

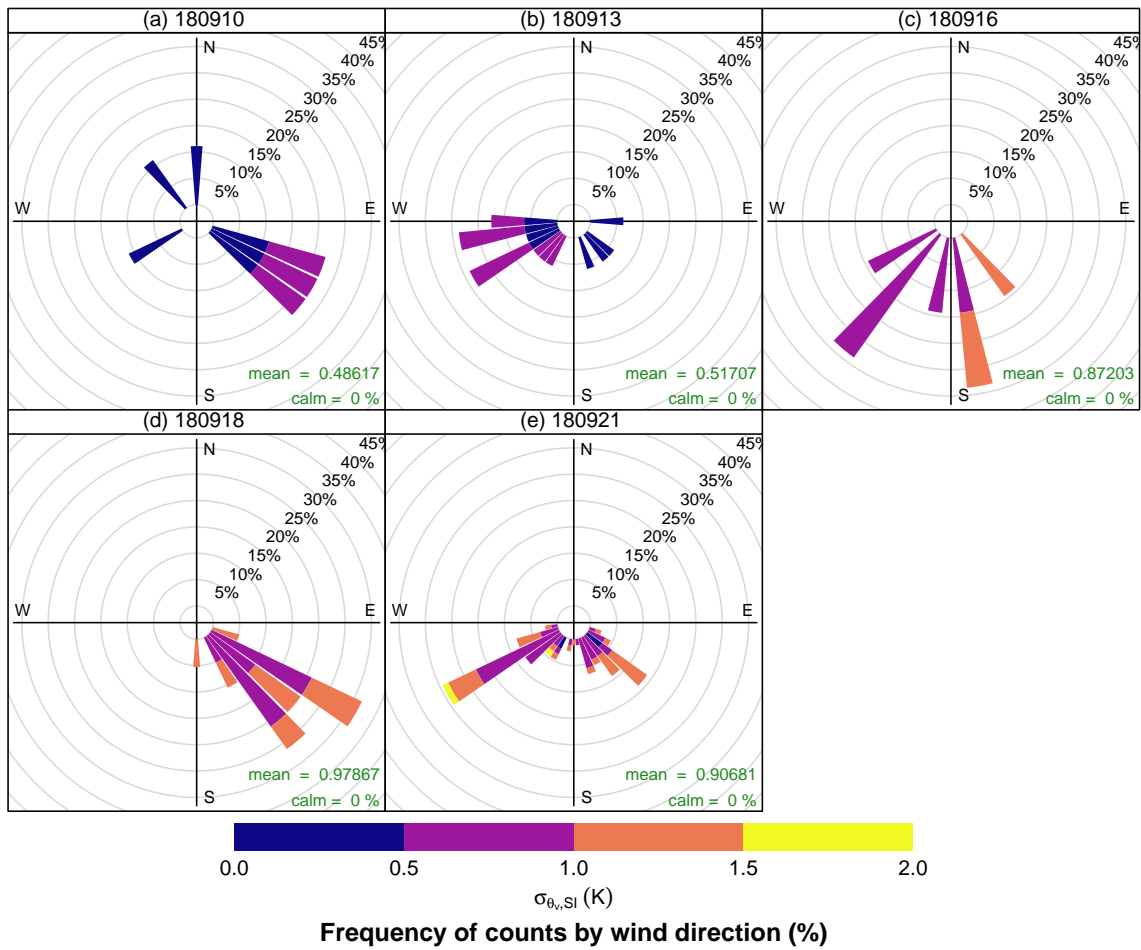


**Figure 3.16** Rose plots of standard deviation of virtual potential temperature  $\sigma_{\theta_v,SI}$  below the median surface-based inversion height in the fiber-optic data (see Tab, 3.2) and for the periods of five fiber-optic experiments. Standard deviations were calculated over 10-min periods. Wind directions were recorded at 10 m agl at the BSRN tower.

to be lifted upwards by up to 100 m. Various effects of these displacements of ILs were observed, including deepening of the SI associated with wind gusts, and apparent “disruption” of the SI concurring with wind direction changes. An example of this IL disruption is described in 3.4.3. When winds turned towards southwest and katabatic flow from southwest advected cold air, these displacements were likely true uplifts of stably-stratified air because of the higher density of the cold air arriving at the surface. However, vertical wind speeds from SODAR could only confirm uplift of air during these vertical displacements of ILs at few occasions which may partly be due to the low temporal resolution of SODAR data. In conclusion, it is likely that fiber-optic data revealed frequent vertical motion of stably-stratified air induced by density differences which were responsible for the deepening or disruption of ILs and the SI.

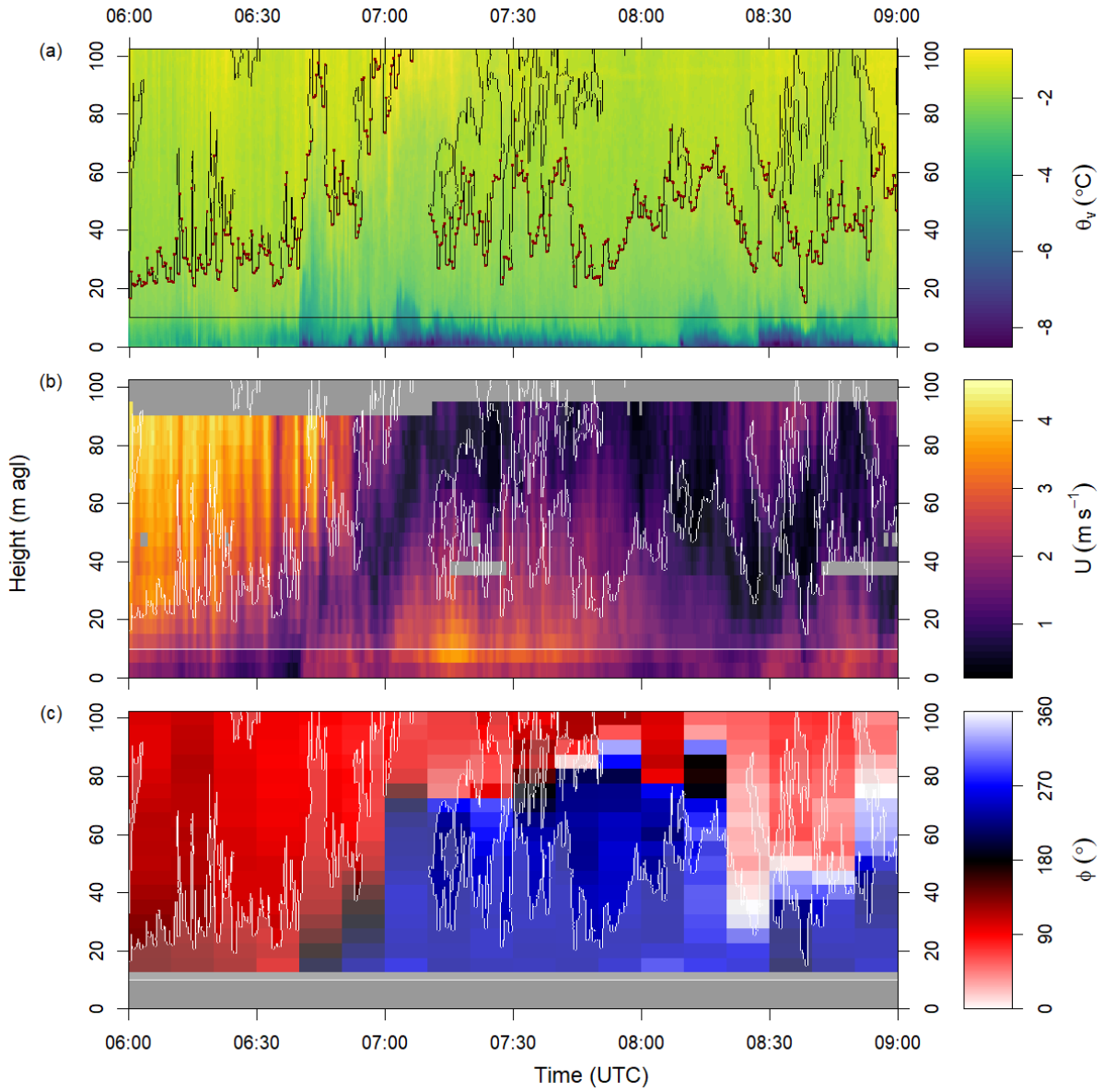


**Figure 3.17** Instantaneous atmospheric profiles of 3 hours of 180921 fiber-optic experiment within the height range of the FireFOX setup; black and white lines indicate borders between inversion layers (ILs) and non-inversion layers or the outer border of sublayer detection; ILs are overlain with light gray. (a) Virtual potential temperatures  $\theta_v$  from fiber-optic data, including dark red dots denoting height of the surface-based inversion. (b) Wind speed  $U$  from fiber-optic measurements, averaged to spatial resolution of 5 m. (c) Wind direction  $\phi$  recorded with SODAR. For entire experiment see Fig. D.6.

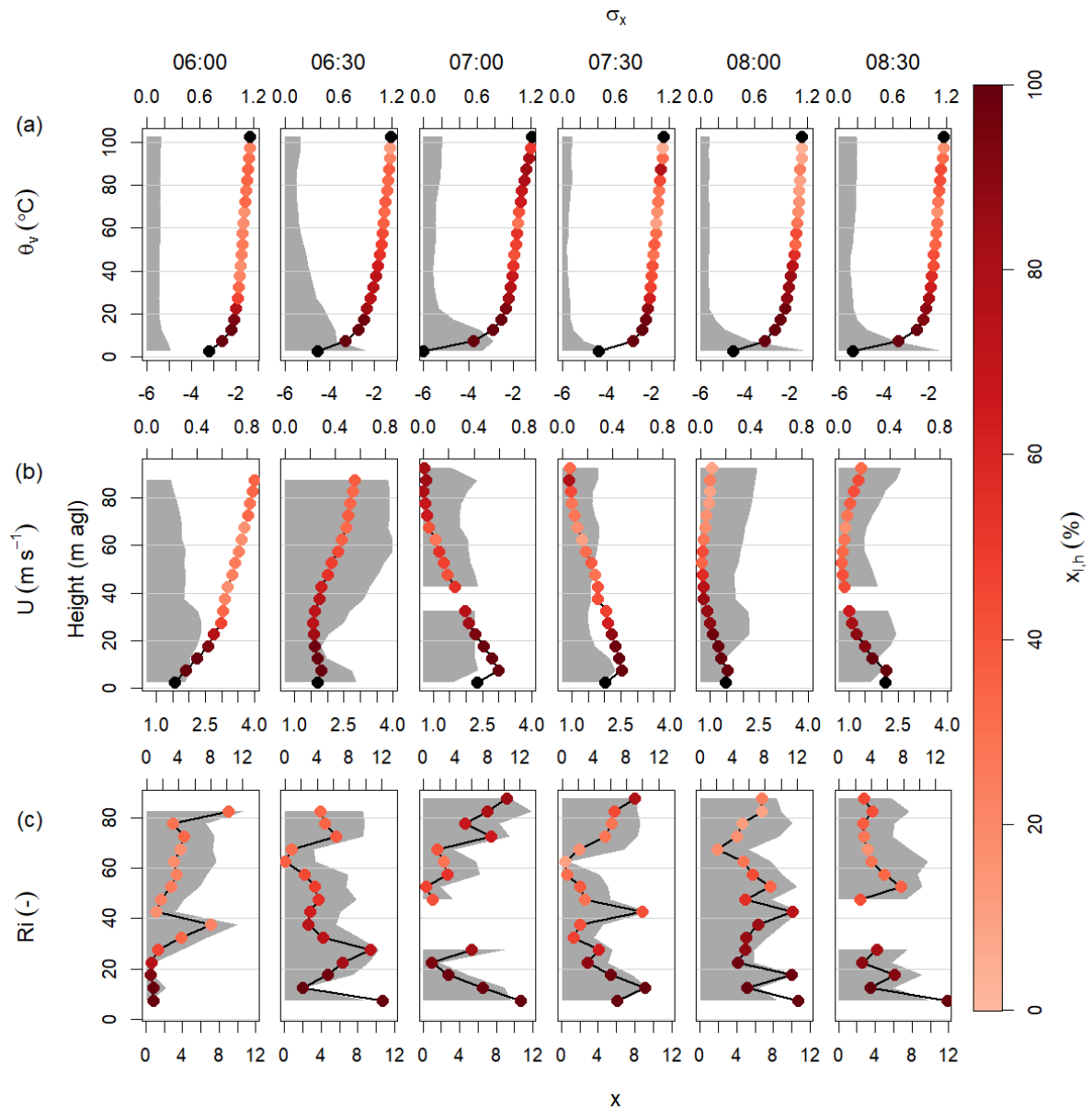


**Figure 3.18** Temporal statistics from a period of the fiber-optic experiment 180921 in time blocks of 30 min length, calculated with a resolution of 20 s. (a) virtual potential temperatures  $\theta_v$  were taken from IceFOX, and (b) wind speeds  $U$  and (c) simplified Richardson numbers  $Ri$  from FireFOX in the height range of the FireFOX experiments. Points show averages, with colors denoting the ratio of temperature inversions at each measurement height across time  $x_{I,h}$ , where temperature inversions are defined as local static stability  $LSS > 0.01 \text{ K m}^{-1}$ . Black points indicate heights with  $LSS$  availability of less than 95 % where no  $x_{I,h}$  was calculated. Gray surfaces show standard deviations. Any  $|Ri| > 30$  was set to 30 before calculating statistics. Only statistics at heights with data availability of more than 60 % are shown. Start time of each block is indicated above the plots in UTC.

### 3.4.3. Exemplary course of dynamics on September 21

The course of dynamics in the SI is presented for a selected period of 180921, ranging from 06:00 UTC to 09:00 UTC on September 21, using fiber-optic  $\theta_v$  and  $U$  and SODAR wind directions (Figs. 3.17-3.18). This period was chosen since it showed a variety of airflow modes in the SI and data availability of  $U$  was high.

Between 06:00 UTC and 06:30 UTC on September 21, strong southeast winds prevailed close to the surface with a nearly logarithmic wind profile in the lowermost 100 m agl. These conditions were associated with nearly subcritical  $Ri$  averaged over 30 min. In the following 30 min, a southwest wind formed at the surface and reached its maximum extent in the lowest 80 m agl between 07:00 UTC and 08:15 UTC, with highest speeds at 10 m agl and distinct shallow cold-air advection in the lowest 10 m agl (Fig. 3.17). During this period mean  $Ri$  over 30-min blocks were close to subcritical at 50 m agl to 70 m agl with an upward-directed momentum flux, but  $Ri$  never reached values below 0.25 within the lowermost 15 m, despite wind speeds of more than  $3 \text{ m s}^{-1}$  (Fig. 3.18c). This indicates the reason why static stability did not decrease with occurrence of these strong winds at the surface which is the suppression of continuous turbulence by high dynamic stability. The arrival of southwest winds with advection of colder air in the lowest 50 m agl concurred with a detachment of a part of the SI which was lifted up to 150 m agl until 08:00 UTC. The uplift of air was confirmed by vertical wind speed measurements by the SODAR. After 08:15 UTC the wind speed minimum descended down to 20 m again, with easterly winds above. Due to the arrival of a new cold-air event at 08:00 UTC, easterly winds did not reach the surface though.

The high spatiotemporal resolution of fiber-optic data revealed a strong variability of atmospheric dynamics in the selected period which resulted from the interplay between different flow modes present in the SI. Still, this period does not cover all modes of airflow observed in the SI during fiber-optic experiments, such as shallow cold-air drainage events with absence of deep katabatic southwest flow (see D.5).

## 3.5. Phenomena in thermodynamic profiles above the surface-based inversion

The thermodynamic structure of the lower troposphere was captured as  $\theta_v$  throughout the fiber-optic profiles. Although there were no wind data from fiber-optics and SODAR available for most of the profiles above the SI, instantaneous  $\theta_v$  profiles enabled the characterization and discussion of thermodynamic phenomena there. The most pronounced types of phenomena observed in  $\theta_v$  profiles are presented here. For a full overview of instantaneous fiber-optic profiles of thermodynamics, the reader is referred to Figs. D.7-D.12.

### 3.5.1. Oscillations of lifted inversions

Temperature inversions above the SI, i.e., LIs showed pronounced wavelike oscillations in height over time. Here, characteristics and effects of these oscillations and their influence on the variability of the vertical thermodynamic structure of the fiber-optic profiles are discussed.

Oscillating LIs corresponded to long-lived ILs with strong stability above the SI, as observed for 180913 and 180918. Typical event scales of oscillations of such long-lived ILs ranged from 10 min to 30 min and reached vertical amplitudes of up to 100 m. These oscillations typically

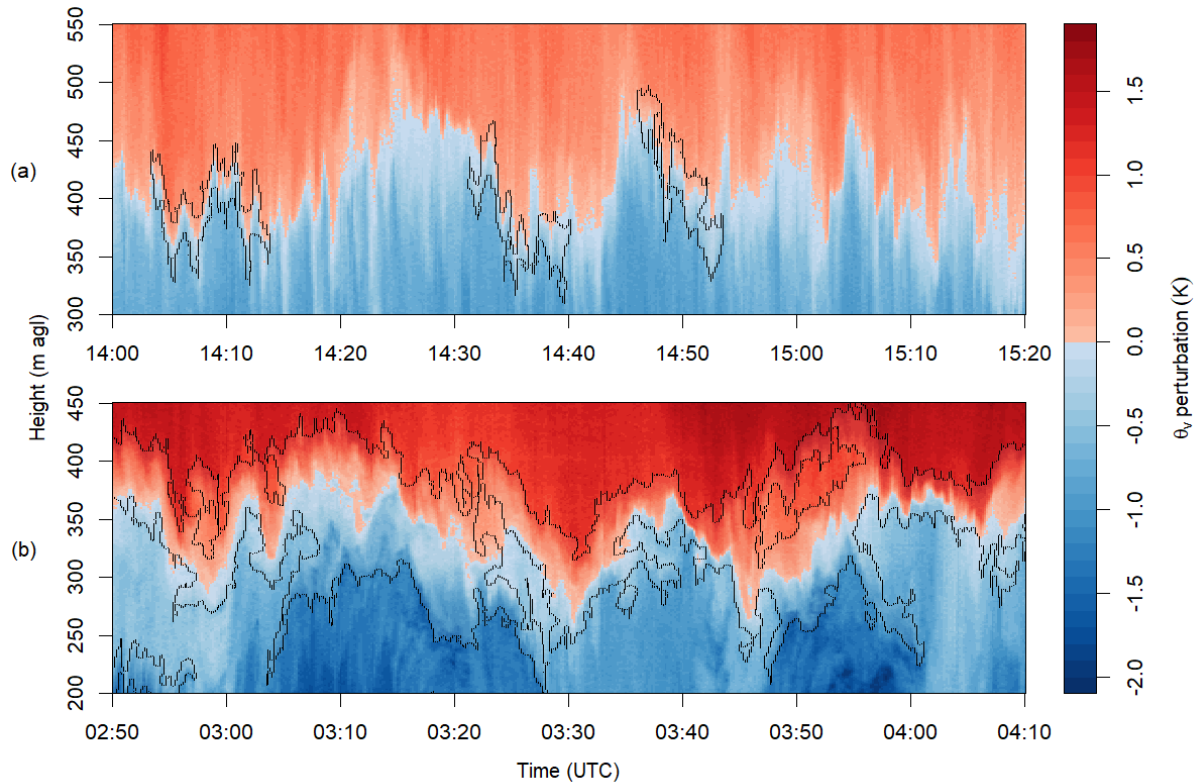


**Figure 3.19** Selections of instantaneous fiber-optic profiles from (a) 180911 and (b) 180913. Colors display perturbation of virtual potential temperature  $\theta_v$  within each of the two selections. Detected inversion layers are indicated by shaded surfaces bounded by black lines.

caused temporal changes in  $\theta_v$  between 1 K and 2 K within a height range of up to more than 100 m. Nearly synchronous oscillation of multiple super-imposed ILs was observed across height ranges of several hundreds of meters under stable conditions and weak uniform easterly winds, which were present during 180918. This synchronicity implied vertical coupling of oscillations.

Oscillations of LIs during 180911 and 180921 showed larger height amplitudes of up to 200 m and similar event scales to those for 180913 and 180918, or lower event scales reaching down to less than 5 min. Due to the weaker static stability of these LIs their oscillations caused similar temperature variations to those observed for 180913 and 180918, despite larger amplitudes in height. The sublayer detection algorithm repeatedly did not merge the oscillating LIs into spatiotemporally continuous ILs. This was due to low thickness and spatiotemporal continuity of LIs for 180911 and 180921, sometimes in combination with the large vertical oscillations.

Examples for the two types of LI oscillations described above are provided in Fig. 3.19, showing spatiotemporal perturbations of  $\theta_v$  within selected fiber-optic data samples: The sample from 180911 displayed a LI centered at 400 m agl to 450 m agl which was shallower and showed weaker stability and stronger height oscillations than the LI from 180913 located at around 350 m agl. Thus, the LI from 180911 was not characterized as a continuous IL by the layer detection algorithm, but three separate ILs were detected instead lasting for a minor part of the observed LI within the selected period, whereas a continuous IL was detected for 180913.

Oscillations of LIs dominated the variability in  $\theta_v$  above the SI, since they were responsible for the peaks in temporal  $\sigma_{\theta_v}$  associated with the presence of LIs (Fig. 3.11).

### 3.5.2. Neutral stability events in non-inversion layers

A frequent feature found in the thermodynamic profiles was the sudden formation of near-neutral static stability, mainly within NILs, which previously exhibited stably-stratified conditions. Due to the transient existence, they may be called neutral stability events (NSEs). NSEs were observed during most of the experiments, with height ranges between  $10^1$  m  $10^2$  m, and lifetimes between  $10^1$  s  $10^3$  s.

Observations indicated that occurrence of NSEs was linked to wind speed: NSEs were largely absent for 180910 and 180918 and occurred most often in 180911 and 180921 data. Since these two pairs of experiments showed the lowest and highest wind speeds above the SI, respectively, as observed in tethersonde data, this difference in NSE abundance suggests that NSEs were forced by turbulent mixing forced by wind shear at high wind speeds.

The cause for the transient appearance of NSEs in the fiber-optic profiles cannot be inferred with certainty because temporal variability of thermodynamics cannot be distinguished from horizontal heterogeneity. However, it is unlikely that NSEs formed through vigorous mixing across hundreds of meters in stably-stratified air. Further, multiple observations of air temperature change up to 1 K along with NSEs indicate advection of heat. These findings point to the appearance of NSEs due to advection of a highly heterogeneous vertical thermodynamic structure past the fiber-optic profile.

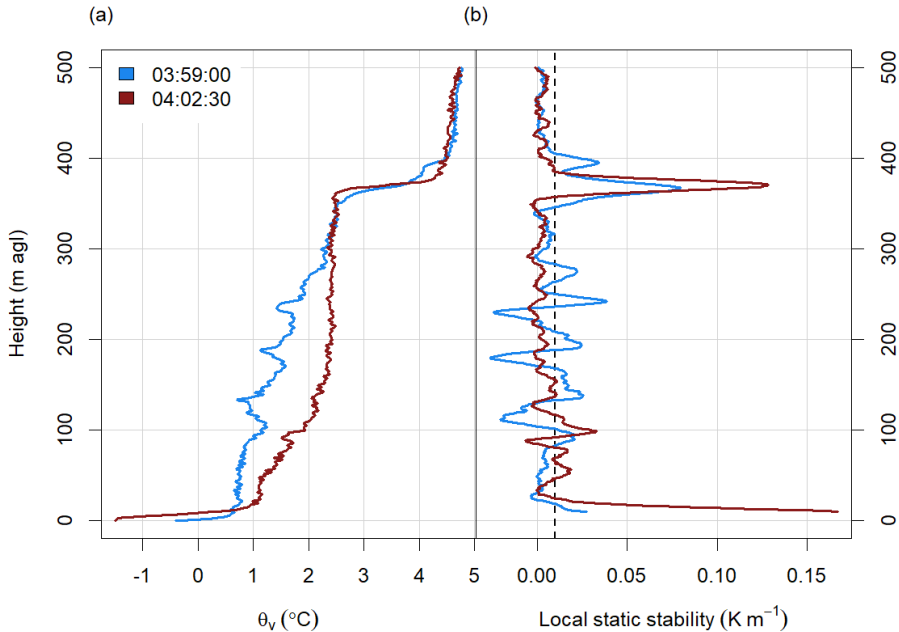


**Figure 3.20** Exemplary instantaneous fiber-optic profiles with a temporal and spatial resolution of 10 s and 0.25 m, respectively, for two time steps on September 13 given in UTC and denoted by colors. (a) Wavelet-filtered virtual potential temperature  $\theta_v$  and (b) local static stability as calculated with Eq. (2.8) from block differences in unfiltered  $\theta_v$ . Vertical broken line marks  $0.01 \text{ K m}^{-1}$ , the defined minimum  $LSS$  of an inversion.

Here, an exemplary NSE is presented: Around 04:00 UTC on September 13, the significant thermodynamic structuring of the atmosphere between 150 m agl and 350 m agl gave way to near-neutral stability within a few minutes (Fig. 3.20). This NSE was characterized by warming of air above the SI and below the long-lived IL at 370 m agl, while the temperatures above this inversion stayed constant. *LSS* of the IL increased during the NSE. Wind speeds recorded by SODAR within this NSE stayed mostly below  $2 \text{ m s}^{-1}$ . Hence, possible short-term variability in wind direction at these low wind speeds could have caused advection of warmer and well-mixed air from the ice-free Fjord which, however, cannot be verified since the resolution of the available SODAR data is too low.

The frequency and scale of NSEs make them a potentially crucial phenomenon in the multi-layered lower troposphere. Since NSEs probably enable vertical mixing of air, they may be an important promoter of vertical exchange of energy and mass in the lower troposphere of the Arctic. However, a deeper analysis of NSEs does not lie within the scope of this thesis, since there were no high-resolution wind measurements available at heights of most NSEs, which would have enabled investigating the influence of shear and advection on NSEs.

### 3.6. Scales observed in fiber-optic profiles of thermodynamics

Scales in the spatiotemporal thermodynamic structure of the lower troposphere were investigated using multiresolution decomposition (MRD) on fiber-optic  $\theta_v$  with varying approaches (see 2.5). These analyses yielded insights into thermodynamic space and time scales in the fiber-optic profiles and in detected sublayers, and into vertical length scales of motions inferred from thermodynamic coupling via 2-point correlations. I decided not to present data from 180916 in this section because of the large ratio of spatial interpolation of  $\theta_v$  necessary for MRD of 180916 data making any analysis untrustworthy. Since MRD spectra return event scales, i.e., half-period lengths, the terms “time scale” and “space scale” exclusively refer to event scales from MRD within this section.

#### 3.6.1. Spatial scales in thermodynamic profiles

Spatial scales in the fiber-optic profiles were investigated via raw spatial MRD spectra of  $\theta_v$  for individual fiber-optic experiments (Fig. 3.21). These spectra were computed by MRD over the entire profiles (see 2.5.1), and calculated with Eq. (2.14). These are the first spectral analyses of vertical spatial scales in atmospheric profiles. Spectra are presented in classes of  $x_{I,t}$ , the ratio of temperature inversions in each instantaneous profile.

Spectral power  $D_{\theta_v}^2$  from 180918 and 180921 was about half an order of magnitude higher across space scales than for the first three experiments, which were recorded under snow-free conditions. This observation underlines the stronger stratification and structuring of the atmosphere under snow-covered conditions.

At the largest space scale  $D_{\theta_v}^2$  displays the bulk change in  $\theta_v$  with height across the profiles. For all investigated experiments largest  $D_{\theta_v}^2$  was found at the largest space scale, reflecting the general increase in  $\theta_v$  with height.

The influence of the SI on spatial scales in thermodynamics was examined. Maximum  $D_{\theta_v}^2$  variability within  $x_{I,t}$  classes was found for space scales between 2 m and 20 m for all experiments, ignoring the largest scale. When an SI was present, it dominated  $D_{\theta_v}^2$  at these space

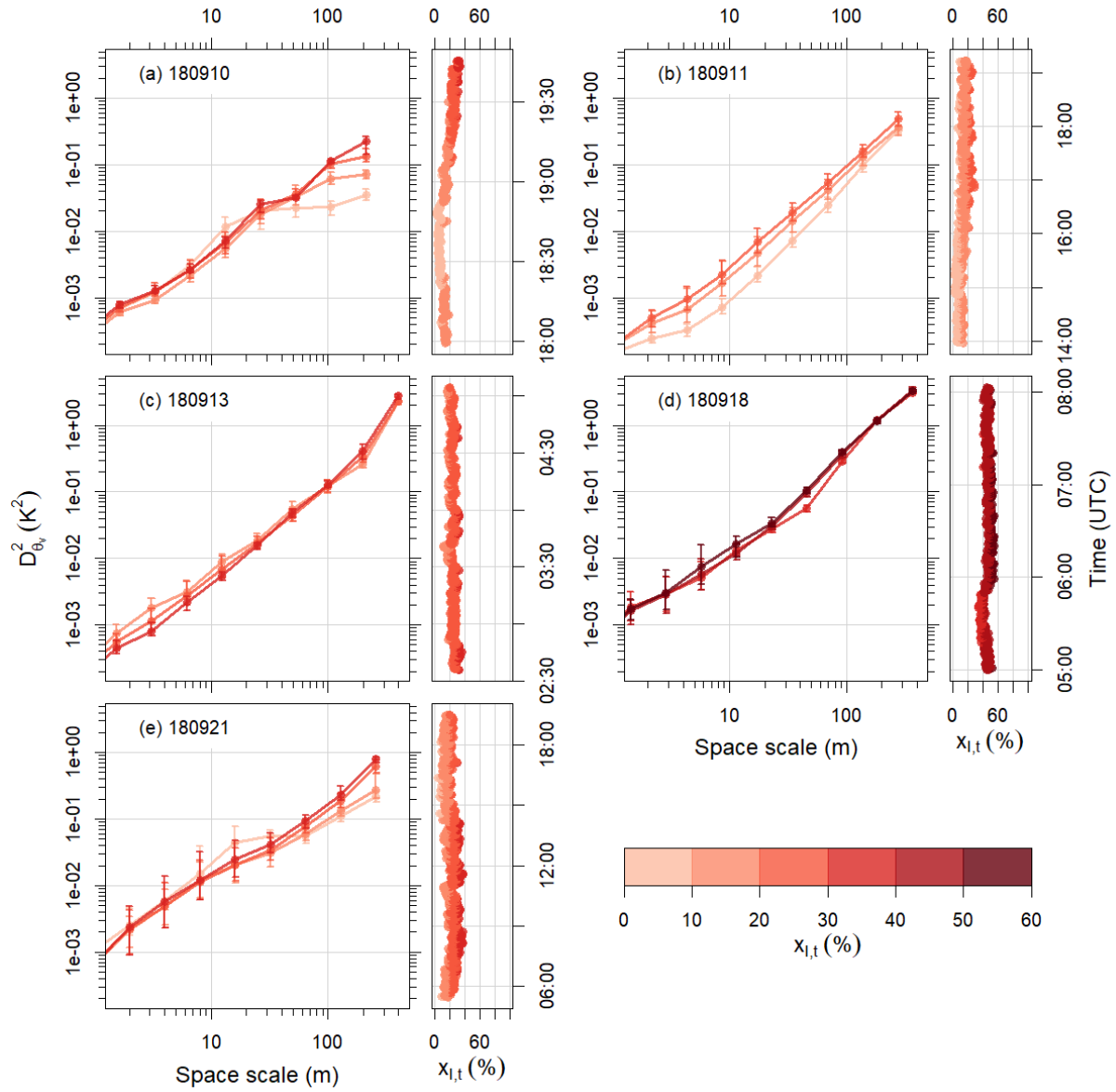


**Figure 3.21** Spatial spectra of virtual potential temperatures from multiresolution decomposition over five entire fiber-optic experiments. Variation of spectral power  $D_{\theta_v}^2$  with space scale is presented in classes distinguished by the ratio of temperature inversions  $x_{I,t}$  for each instantaneous profile, where space scale refers to event scale, i.e., half-period length. For each stability class and space scale median of  $D_{\theta_v}^2$  is marked by points with bars denoting interquartile ranges. Distribution of  $x_{I,t}$  across time is shown for each experiment. Only space scales larger than the critical length 1.57 m of spatial wavelet filtering are shown (see Fig. A.8).

scales, so the variability in  $h_{\text{SI}}$  was likely responsible for the large variability in spectral power within experiments at these scales. The only period with longer absence of a SI was observed in 180911 from 14:00 UTC to 16:30 UTC (Fig. D.8a). This period roughly corresponded to  $x_{\text{I,t}} < 10\%$ , where a significant log-slope decrease in the spatial spectra was found for scales smaller than 5 m (Fig. 3.21b). This flattening of spectral slope might have been impacted by remaining instrument noise, or by physical variability, which unfortunately cannot be discerned. In conclusion, the presence and variability of an SI distinctly impacts spatial scales in thermodynamics in atmospheric profiles reaching maximum heights of several hundreds of meters.

Stationary and instationary thermodynamic conditions in the fiber-optic profiles were connected to patterns in the spatial spectra: The variability of  $D_{\theta_v}^2$  over time and across  $x_{\text{I,t}}$  classes at larger space scales than 100 m was very low between and within  $x_{\text{I,t}}$  classes for 180913 and 180918, while there were clear differences between  $x_{\text{I,t}}$  classes for 180910 and 180921. The low variability for 180913 and 180918 was due to the stationary profile characteristics with long-lived ILS. Instationary conditions explain the increased  $D_{\theta_v}^2$  for higher  $x_{\text{I,t}}$  classes for 180910 and 180921, such as warm-air advection above 300 m agl on September 10 (see Fig. D.7a).

These first analyses of spatial MRD spectra in atmospheric profiles revealed differences in  $\theta_v$  variability across space scales between experiments. Presence of snow cover increased spatial  $\theta_v$  variations for all observed scales, and the SI dominated  $\theta_v$  variability at scales between 2 m and 20 m.

### 3.6.2. Temporal scales in thermodynamic profiles

Raw temporal MRD spectra over the entire duration of fiber-optic experiments were used to infer temporal scales in the fiber-optic  $\theta_v$  profiles (see 2.5.1). Spectra are presented in classes of  $x_{\text{I,h}}$ , the ratio of temperature inversions at each measurement height across experiment duration (Fig. 3.22).

Broad spectral peaks and plateaus in spectral power  $D_{\theta_v}^2$  were observed within the SI. In the lowermost 10 m agl these peaks exhibited the largest  $D_{\theta_v}^2$  in the fiber-optic profiles for most experiments and time scales, often more than one order of magnitude higher than in the height classes above. This underlines the finding from the analysis of spatial spectra that the SI dominated  $\theta_v$  variability in the profiles.

Spectral peaks in the lowermost 20 m agl spanned 1.5 orders of magnitude of time scales between 30 s and 3000 s. A substantial part of  $\theta_v$  variability on these time scales can be attributed to events of cold-air drainage from southwest and south. Longest maximum time scales of these drainage flows were reached for 180918 and 180921, both showing more than  $10^3$  s in the lowermost 10 m agl (Fig. 3.22d-e). Further, median  $D_{\theta_v}^2$  at scales of cold-air drainage events between surface and 10 m agl was largest for these two experiments, reaching more than  $0.1 \text{ K}^2$ . This confirms that cold-air drainage events lasted longer and created more distinct  $\theta_v$  variability when soil was snow-covered.

Between 20 m agl and 50 m agl spectral power between 30 s and 3000 s decreased relative to the surface by more than half an order of magnitude, and peaks narrowed to a time scale range of one order of magnitude or less and shifted to larger time scales of 100 s to 3000 s. This change in spectra with height mirrors the reduced impact of cold-air drainage at heights of more than 20 m agl, and the dominance of larger structures and motions there.

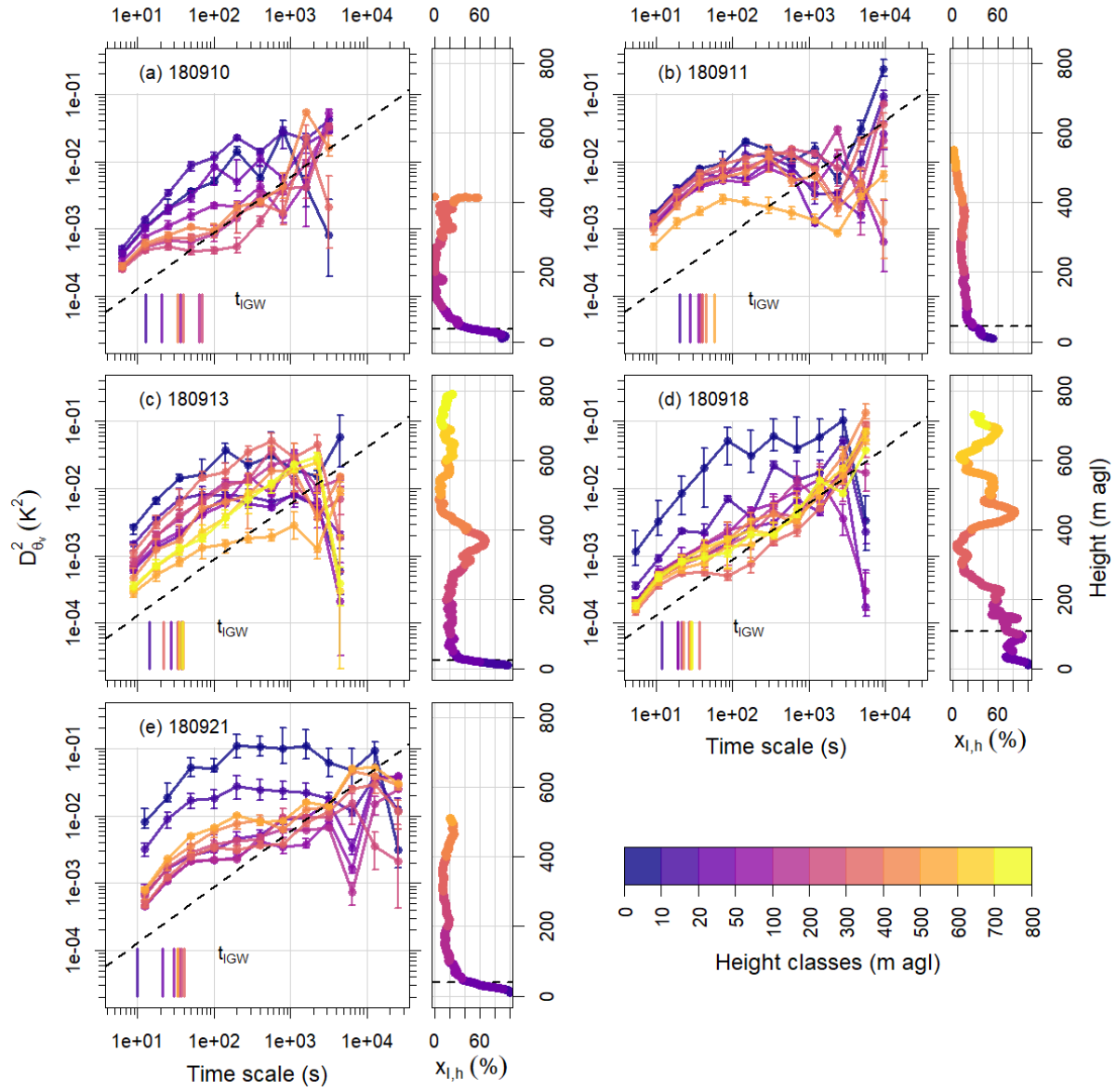


**Figure 3.22** Temporal spectra of virtual potential temperatures from multiresolution decomposition over five entire fiber-optic experiments. Variation of spectral power  $D_{\theta_v}^2$  with time scale is presented in classes distinguished by height agl, where time scale refers to event scale, i.e., half-period length. For each height class and space scale, median of  $D_{\theta_v}^2$  is marked by points with bars denoting interquartile ranges. Diagonal broken line indicates 5/6 log slope. Distribution of ratio  $x_{I,h}$  of inversions across measurement heights is shown for each experiment, with a horizontal broken line signifying respective median surface-based inversion heights.  $(2 N_{BV})^{-1} = t_{IGW}$ , the average minimum event scale of internal gravity waves was calculated after Eqs. (2.9)-(2.11) for each height class, except between 0 m agl and 10 m agl, where no *LSS* was determined.

Spectral peaks above the SI were expected to correspond to oscillations of LIs which were observed to result in large  $\theta_v$  variability (see 3.5.1). This connection was confirmed by correlations between  $D_{\theta_v}^2$  peaks and  $x_{I,h}$  for individual fiber-optic experiments, displayed in Fig. 3.22: Spectral peaks were most pronounced at high  $x_{I,h}$ , such as for 180913 between 300 m agl and 400 m agl, where highest  $D_{\theta_v}^2$  of all fiber-optic data above the SI was observed. Correspondingly, low  $x_{I,h}$  was associated with lowest  $D_{\theta_v}^2$  in peaks above the SI, observed for example between 500 m agl and 600 m agl for 180911 and 180913. These observations match the connection between  $x_{I,h}$  and temporal  $\sigma_{\theta_v}$  over experiment duration described in 3.2.

Time scales of  $D_{\theta_v}^2$  peaks associated with oscillations of LIs differed between experiments. For 180911 and 180921, two experiments with weak stability above the SI, such peaks or plateaus were found at time scales between 30 s and 1000 s, with  $D_{\theta_v}^2$  reaching  $10^{-2}$  K<sup>2</sup>. Peaks connected with LI oscillations for 180913 showed time scales between 60 s and 3000 s, where highest  $D_{\theta_v}^2$  was observed for scales from 200 s to 3000 s, almost reaching  $10^{-1}$  K<sup>2</sup>. 180918 showed oscillations of ILs at similar time scales to 180913. Due to their weaker amplitudes induced  $D_{\theta_v}^2$  was so low that it was obscured by the temporal trend in  $\theta_v$  above the SI indicated by the distinct maxima in  $D_{\theta_v}^2$  at the largest time scale for 180918. To find the time scales associated with oscillations of ILs for 180918, the  $\theta_v$  time series at 500 m agl was linearly detrended, resulting in the emergence of a spectral peak at a scale of 1000 s. Individual experiments showed increased  $\theta_v$  variability associated with LI oscillations at similar time scales between 30 s and 3000 s. At high occurrence of LIs, as found for 180913 and 180918, highest  $\theta_v$  variability was observed towards the larger end of this scale range. Despite the strong overlap of time scales of  $\theta_v$  variability induced by LI oscillations between experiments, 180911 and 180921 showed a general tendency to oscillations at smaller time scales than 180913 and 180918.

Temporal spectral analysis enables studying the time scales of homogeneous Kolmogorov cascade turbulence in the fiber-optic profiles via searching for inertial subranges. While inertial subranges are characterized by a 5/3 log-log slope when using Fourier spectra based on period lengths, MRD yields event scales, i.e., half-period lengths, leading to inertial subranges showing 5/6 log-log slopes in the spectra. Since the temporal MRD involved resampling of data to a larger dyadic length (see 2.5.1), time scales smaller than the original sampling resolution were yielded. Thus, time scales smaller than 20 s and 10 s for 180921 and the other fiber-optic experiments, respectively, contain no true signal and can therefore not be interpreted.

Inertial subranges within the SI were searched in the temporal MRD spectra. Turbulence in contact with the surface under weakly stable conditions at subcritical  $Ri < 0.25$  typically shows an inertial subrange at smaller time scales than 10 s, while the inertial subrange breaks down at supercritical  $Ri$  (e.g. Grachev et al., 2013; Acevedo et al., 2014). Hence, no inertial subranges were expected to be found within the SI in the fiber-optic temperatures. However, 5/6 log-log slopes existed in the spectra of lowermost 10 m agl for all experiments, at maximum scales between 30 s and 100 s (Fig. 3.22). These observations indicate the presence of Kolmogorov turbulence close to the surface even under the observed strongly stable conditions with supercritical  $Ri$ . This finding lines up with observations of surface-based turbulent layers under very stable conditions by Petenko et al. (2019). Thus, continuous turbulence was likely present close to the surface which may have been generated by intermittent strong wind shear (see 3.4.1).

At all heights above the SI, clear 5/6 log-log slopes were found for 180911, 180913 and 180921 at time scales smaller than 40 s to 80 s (Fig. 3.22b,c,e). This matches observations of inertial

turbulence at time scales of a few minutes and less in the free atmosphere by Vinnichenko (1970). Thus, these observed 5/6 log-log slopes and gaps probably displayed inertial Kolmogorov turbulence.

Spectral gaps clearly separating turbulent from meso-scale motions in temporal spectra simplify the detection of scales of turbulence. Multiple spectral gaps were found in the temporal MRD spectra, which were most distinct at low  $x_{I,h}$ : A spectral gap at time scales between 2000 s and 3000 s was partly observed for 180911. This observation corresponds to gap scales of nearly 1 hour, estimated for near-neutral conditions in CASES-99 data at 100 m agl by Vickers and Mahrt (2003). At low  $x_{I,h}$ , a spectral gap emerged for 180910 and 180918 at around 100 s, possibly with Kolmogorov turbulence at smaller time scales, providing evidence that turbulence outside the SI at low wind speeds showed smaller scales than at stronger winds, as observed for 180911, 180913 and 180921. Since the spectral gaps were located at submeso scales, they were more distinctive at near-neutral conditions, where they were not overlain by substantial temperature variability caused by submeso-scale motions which was present at stronger stability.

The analysis of  $t_{IGW}$  enables testing whether observed LI oscillations were possibly connected with IGWs. The entire scale ranges of the spectral peaks and plateaus associated with LI oscillations were larger than the corresponding smallest possible time scales of IGWs,  $t_{IGW}$  (Fig. 3.22b-e). This implies that the observed oscillations were potentially associated with IGWs propagating along LIs. This suspicion is supported by the observed vertical amplitudes of IGWs which match typical values of up to 200 m (e.g. Finnigan et al., 1984). Thus, observations point to gravity waves caused by the flow of stably-stratified air across the mountainous terrain of Svalbard as the most likely forcing for the observed oscillations of LIs. Still, observed LI oscillations may represent the horizontal heterogeneity of the lower troposphere rather than true wave motions which cannot be discerned by the recorded data.

Since maximum time scales of inertial subranges in MRD spectra were in most cases equivalent to  $t_{IGW}$  and the smallest scales of  $D_{\theta_v}^2$  peaks associated with wavelike LI oscillations, production of turbulent energy was likely connected to these oscillations. This connection between wavelike oscillations of LIs and the production of turbulence has been observed before (Gossard et al., 1985; Chimonas, 1999).

### 3.6.3. Spatial and temporal scales in thermodynamics of sublayers

Spatial and temporal spectra from MRD of fiber-optic  $\theta_v$  for sublayer samples, as calculated in 2.5.3, were used to analyze scales in thermodynamics of ILs and NILs. To this end median spectra for samples of each detected sublayer are displayed in Fig. 3.23.

Power  $D_{\theta_v}^2$  of spatial MRD spectra of IL samples, as calculated in 2.5.3, was increased by up to 1.5 orders of magnitude relative to NILs (Fig. 3.23a). For both sublayer classes, log-log slopes of around 5/3 were typical at scales of more than 10 m. At smaller space scales the slope was the same for ILs, but decreased significantly for NILs. This led to smaller differences in power between ILs and NILs which became almost insignificant for 180921. The constant slope can be easily explained by the increase in  $\theta_v$  with height which was typical even for most NILs. The high spectral power caused by this temperature trend obliterated smaller structures in ILs. Since the power caused by temperature trend was lower for NILs than for ILs, structures of less than 10 m scale became apparent there. However, the flattened slope of NIL spectra at these

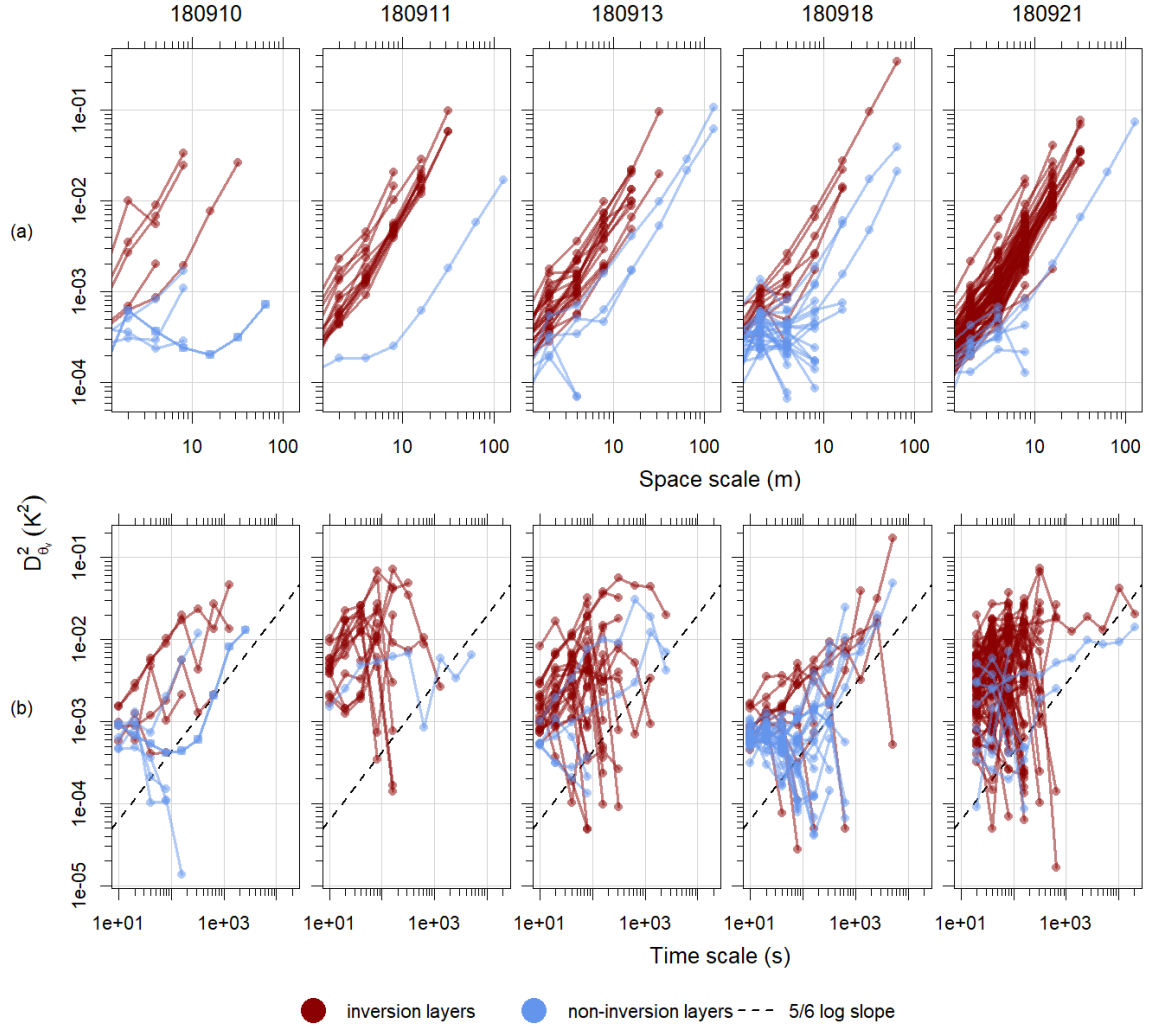


**Figure 3.23** Spectra of virtual potential temperatures from multiresolution decomposition over detected sublayers in (a) space and (b) time, respectively, for five fiber-optic experiments. Space and time scale refer to event scale, i.e., half-period length. Median  $D_{\theta_v}^2$  of each individual sublayer is shown, with colors distinguishing between inversion layers and non-inversion layers. In (a), only space scales larger than the critical length 1.57 m of spatial wavelet filtering are shown (see Fig. A.8). Physically most meaningful deep non-inversion layer, detected for 180910, is indicated by blue squares.

scales may have occurred due to remaining instrument noise in the filtered temperatures, and a clear association with physical features was not possible.

The deep NIL with lowest power at scales of more than 10 m was found for 180910 (indicated in Fig. 3.23). This sublayer did only reach a  $D_{\theta_v}^2$  of less than  $10^{-3}$  K<sup>2</sup> at 64 m scale where deep NILs of other experiments around  $10^{-2}$  K<sup>2</sup>. This points to the influence of the erroneous detection of long-lived and deep NILs (see 3.3), where all NILs with space scales of more than 20 m in the MRD spanned across step  $\theta_v$  steps, with the exception of the deep NIL for 180910. Hence, spectral power of NILs might be overestimated at large scales for these NILs because of  $\theta_v$  variability induced by stable sections within these NILs. This suggests that the deep NIL of 180910 showcases the only representative example for a spectrum of a deep NIL.

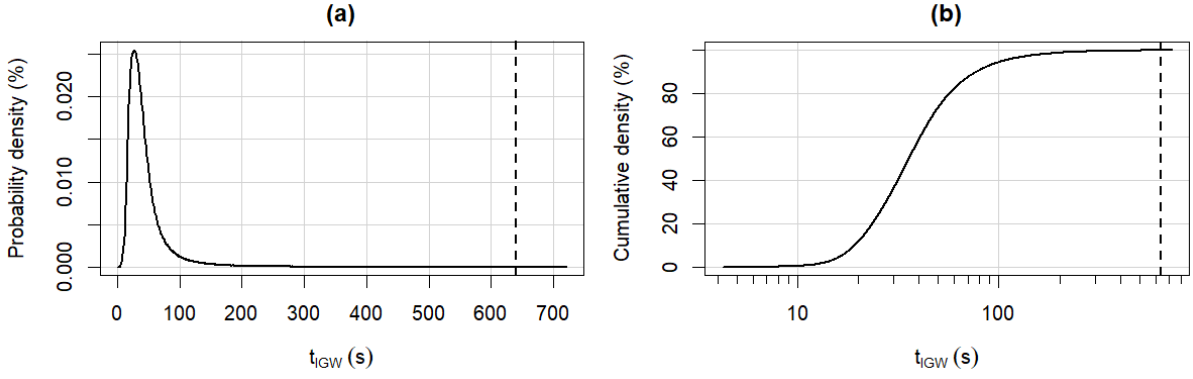


**Figure 3.24** (a) Probability density and (b) cumulative probability density of minimum event scale of internal gravity waves  $t_{IGW} = (2 N_{BV})^{-1}$  from fiber-optic data, with Brunt-Väisälä frequency  $N_{BV}$ . The smaller 99.9 % of all observed  $t_{IGW}$  are shown. Vertical broken lines mark 640 s, the window size of multiresolution decomposition for investigating vertical scales of horizontal motions.

Temporal spectra of sublayers unfortunately showed such large variations within the sublayer categories that a categorization was not possible. Supposedly, the assumption of ergodicity was not fulfilled for single sublayers, with varying and sometimes very short layer duration preventing temporal and spatial mean to converge.

### 3.6.4. Vertical length scales and coupling of horizontal motions

Temporal MRD of fiber-optic  $\theta_v$  in time windows of 640 s provided the basis for estimating the relationship between time scales and vertical length scales of motions across the atmospheric profiles (see 2.5.2). The vertical length scale parameter  $L_v$  was calculated via decay of 2-point correlations between measurement heights for individual MRD modes. Thus,  $L_v$  can be viewed as a scale of vertical coherence of horizontal motions, i.e., it describes the depth of coupled motions at each elevation and at each time scale smaller than the window size of 640 s.

Minimum event scale of IGWs  $t_{IGW}$  was below 640 s for more than 99.9 % of all fiber-optic measurements, despite a significantly right-skewed probability density distribution (Fig. 3.24). In more than 50 % of data  $t_{IGW}$  did not exceed 40 s. Consequently, all time scales larger than 20 s observed in this MRD analysis may have been significantly influenced by buoyancy-driven oscillations of air masses.

$L_v$  increased with time scale at scales smaller than 160 s for all measurements (Fig. 3.25). At larger time scales, but below the largest time scale of 640 s, the relationship between time scale and  $L_v$  showed flatter increase or even became insignificant for most experiments. The relatively constant  $L_v$  at time scales between 80 s and 320 s across the fiber-optic profiles reveal increasing anisotropy of motions with scale, i.e., horizontal air motions becoming flatter the larger they were.

For 180910, significant increase in  $L_v$  was present at all observed time scales above the SI. (Fig. 3.25a). Since the atmosphere was neutrally stratified above the SI for most of this experiment (Fig. D.7a), larger motions were probably more isotropic there than for the other flights where profiles were clearly more stratified at these heights.

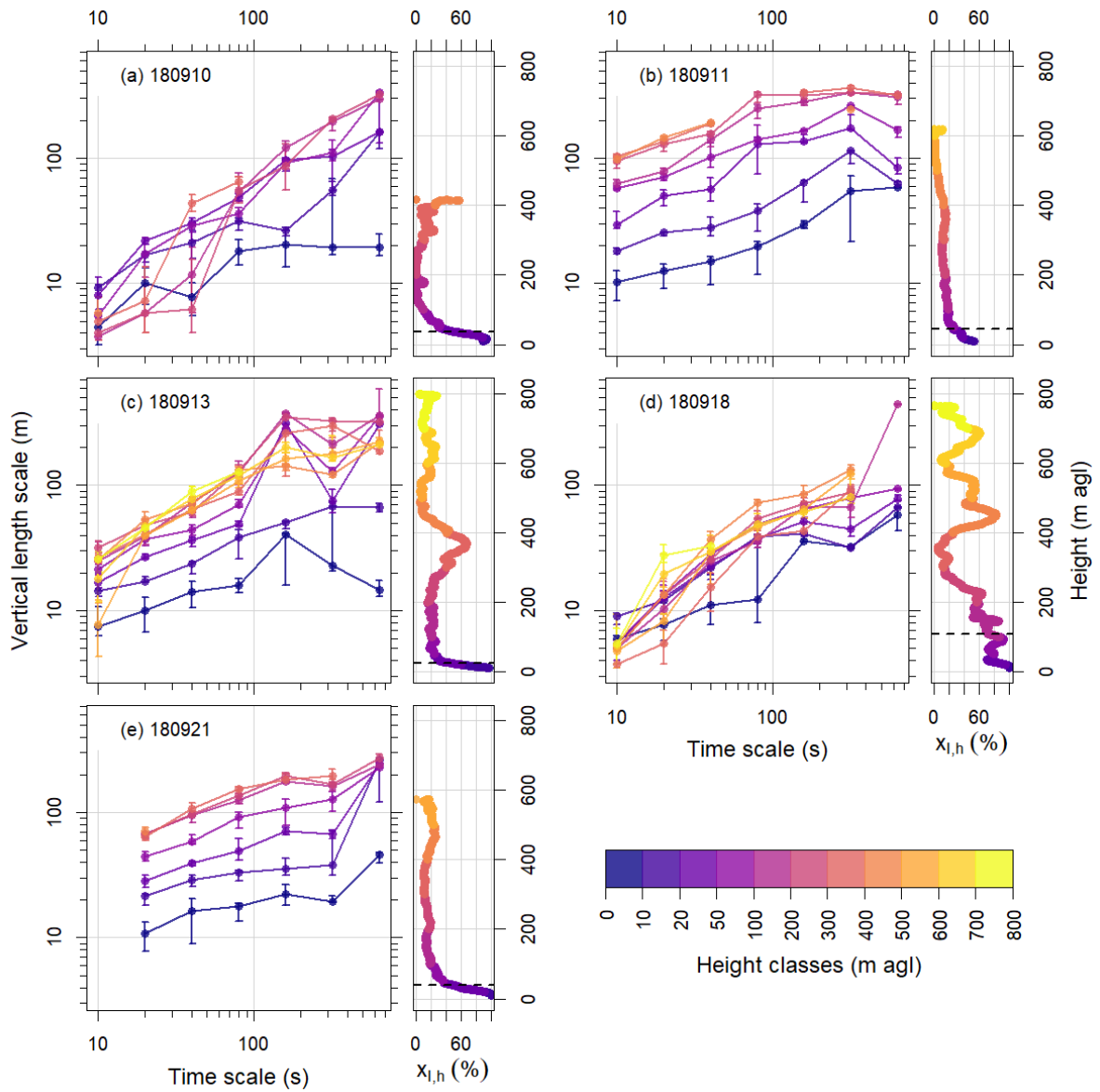


**Figure 3.25** Vertical length scales  $L_v$  of observed motions for five fiber-optic experiments, inferred via correlation decay of multiresolution decomposition modes between individual measurement bins in the fiber-optic virtual potential temperatures, and plotted against multiresolution time scale. Time scale refers to event scale, i.e., half-period length. Statistics of  $L_v$  were calculated in height classes, with points and bars showing medians and interquartile ranges, respectively, of all bins with data availability  $> 50\%$ . Height classes, ratio of inversions  $x_{I,h}$  and median surface-based inversion height are shown as in Fig. 3.22.

Within the SI, increase in  $L_v$  with time scale was weaker than above or nonexistent, with  $L_v$  rarely exceeding 50 m in the lowermost 10 m agl (Fig. 3.25). This underlines the very flat pancake-like structure of motions typical for the SI, and the very weak coupling of the SI to the more elevated atmosphere (e.g. Mahrt et al., 2009).

Relatively high  $L_v$  within the SI was observed for a specific time scale: For several experiments, a peak in  $L_v$  was observed in the lowest 10 m agl at 160 s, reaching values of more than 40 m (Fig. 3.25c-e). This time scale often showed high spectral power as well (Fig. 3.22), associated with cold-air advection. There were no systematic differences in  $L_v$  between experiments with and without snow cover (Fig. 3.25). Thus, 160 s is concluded to be the time scale with highest vertical coherence of cold-air advection observed in the SI.

The variability of  $L_v$  with height was investigated across fiber-optic profiles. On average,  $L_v$  increased with height within the SI. In most cases this positive correlation between  $L_v$  and height existed in the lowermost 100 m agl to 200 m agl (Fig. 3.25b,c,e). From these observations it is deduced that the shape of air motions at the observed scales changed with height from pancake-like structures at the surface to more isotropic motions at heights of 100 m agl to 200 m agl. Above these heights, there was no clear connection between  $L_v$  and height for all experiments, indicating that motions did not further grow in depth with height above 100 m agl to 200 m agl. This phenomenon may be due to the often distinct multi-layered structure in the profiles decoupling air masses vertically from one another, limiting vertical extent of air motions to  $L_v$  of mostly lower than a few hundreds of meters.

The influence of wind speed above the SI on vertical length scales was tested by comparing tethersonde wind speed data to  $L_v$ . Magnitudes of  $L_v$  at time scales of 160 s and 320 s  $L_v$  for all data above 100 m agl showed a positive relationship to mean tethersonde wind speed (linear regression:  $R^2 = 0.36$ ,  $p < 0.001$ ). Hence, vertical coherence of motions was positively connected to wind speed above the SI. This relationship between wind speed and  $L_v$  may have been related to weaker  $LSS$ , and to the more frequent deep NSEs observed during experiments with high wind speed, enabling vertical turbulent exchange of energy across large distances.

Assuming Taylor's hypothesis of frozen turbulence, tethersonde wind speeds could be used to infer a crude estimate of the relationship between time scale and horizontal space scale above the SI from the MRD analysis. To this end, the increase in  $L_v$  with time scale between time scales of 20 s and 80 s above 100 m agl was compared with mean tethersonde wind speed. These parameters were correlated (linear regression:  $R^2 = 0.58$ ,  $p < 0.001$ ). This relationship confirms that time scales corresponded to larger horizontal space scales of motions under higher wind speeds. Hence, part of the between-experiment variation in the dependence of  $L_v$  on time scale is based upon differences in wind speeds. However, the validity of Taylor's hypothesis in fiber-optic profiles above the SI could not be tested, since no sufficiently resolving wind speed estimated were available.

At the largest calculated time scale of 640 s  $L_v$  could not be interpreted as vertical length scale of motions at this time scale. Instead,  $L_v$  corresponded there to structures with larger time scales, such as  $\theta_v$  trends over experiment periods. Equal  $L_v$  at largest time scale across different height classes of an experiment revealed corresponding temperature trends. Often the lowermost 10 m agl showed different trends than the atmosphere above (Fig. 3.25a,c,e). Concurring trends in  $\theta_v$  above the SI partly generated larger  $L_v$  than detectable within the profile at 640 s already at 200 m agl (Fig. 3.25d).

The analysis of  $L_v$  across time scales, measurement heights, and fiber-optic experiments revealed multiple influences on vertical length scales of motions across the fiber-optic profiles. These include increase in  $L_v$  with wind speed above the SI, restrictions of  $L_v$  within the SI to few decameters, and above the SI to few hundred meters at time scales of less than 640 s. Thus, the parameter  $L_v$  has proven as a useful tool to assess vertical length scales in high-resolution fiber-optic data.

### 3.7. Response of the surface-based inversion to varying airflow

After detailed analysis of atmospheric conditions within the SI by means of fiber-optic and ancillary measurements and multiple statistical methods, shown in earlier parts of results and discussion, this section provides a condensed discussion of the observed properties and variability of the SI as it responded to varying footprints and flow modes.

The shallow strong surface-based temperature inversions (SIs) within the lowermost 20 m agl to 50 m agl, with dominating supercritical  $Ri_b$  at the BSRN tower found for all experiments, show that very stable conditions were present for most of the fiber-optic recording periods at the surface. The strong temporal variation and heterogeneous structure of wind and temperatures observed near the surface fit typical properties of very stable boundary layers, as described by Mahrt (2014). Temperature variability over time periods of 10 min within the SI was strongly increased by snow cover conditions, while wind directions and dynamic stability, as defined in the BLRs, had a minor impact on temperature variability and were therefore unable to relatively predict average temperature variability of experiments in the SI. The change between surface flow modes caused a peak in  $\theta_v$  variability at the ground, exceeding variability higher up in the atmosphere by more than a factor of 2. In contrast, wind speed variability was lowest at the surface and increased by a factor of more than 2 with height in the lowest 100 m agl. Among the surface flow types, local cold air drainage, particularly from the direction of the Brøggerbreen glaciers generated the largest temperature variability. These directions were associated with the largest momentum flux and the strongest turbulent sensible heat transport towards the surface, which occurred simultaneously, independent of snow cover situation. Lowest temperature variability within the SI and lowest dynamic stability was observed for weak winds from between northwest and east, transporting well-mixed air from Kongsfjorden with absence of snow cover, which was the only occurrence of absence of a surface-based inversion.

Within the lowest 20 m of the SI, submeso-scale motions with event scales between 30 s and 3000 s dominated temperature variability. These intense submeso-scale structures under the observed very stable conditions can be explained by the complexity of the terrain (Mahrt, 2014; Hoover et al., 2015; Pfister et al., 2017; Mahrt et al., 2020). Submeso-scale structures in temperatures within the SI were clearly connected with variability of flow directions and modes: At time scales of cold-air drainage events from south and southwest, submeso-scale motions were often coupled vertically within more than half of the entire SI. Small vertical length scales  $L_v$  within the SI provided evidence for the flat shape of submeso-scale motions and weak coupling between the SI and the air above at corresponding time scales.

Vertical displacement of air within the SI was frequently observed, often forced by arrival of colder air at the surface. These vertical movements caused a thickening of the SI, which partly led to detachment of stably-stratified air masses from the SI.

Kolmogorov turbulence was indicated by 5/6-log-log slopes close to the surface at maximum time scales of 30 s to 100 s, contradicting frequent observations of time scales smaller than 10 s for very stable conditions (e.g. Grachev et al., 2013; Acevedo et al., 2014). Richardson number  $Ri$  was nearly constant with height in the lowest 100 m agl, at supercritical values of around 5. However, high spatiotemporal variability of  $Ri$  enabled intermittent production of stronger turbulence with subcritical  $Ri$  in instantaneous data at resolutions of 10 s to 20 s, found at all heights within the SI. Such intermittent mixing events can contribute the major

part of the turbulent exchange under such strongly stable conditions (Mahrt et al., 2012). Close to the surface, subcritical  $Ri$  values under very stable conditions were only found during events of strong wind shear in the entire SI, with absence of wind maxima close to the surface caused by katabatic flow from Brøgger Valley. This finding contradicts the strong negative  $Q_H$  values recorded for southwest winds, which should not have been possible at supercritical  $Ri$  with discontinuous turbulence.

### 3.8. Conditions influencing lifted inversions and their variability

The presented and analyzed temperature profiles in the lower troposphere over Ny-Ålesund clearly showed that temporal temperature variability is strongly impacted by the presence and variability of lifted temperature inversions separating less stable or near-neutral layers. Here, the contributions of atmospheric conditions impacting the occurrence and properties of lifted ILs and NILs above the SI are discussed.

When comparing general patterns in atmospheric structure above the SI, three simplified lower troposphere regimes (LTRs) emerged:

- LTR1 showed near-neutral stability, i.e., a residual layer, above the SI, leading to low  $LSS$  values. Inversions were deep and long-lived and fluctuated weakly in height at large time scales. LTR1 was observed in 180910.
- LTR2 was defined by low  $LSS$  and shallow, often spatiotemporally discontinuous inversions, partly with large height oscillations at short time scales, and is represented by 180911 and 180921.
- LTR3 exhibited strong  $LSS$ , with deep and long-lived inversions oscillating at medium height amplitudes, and was extracted from 180913 and 180918.

180916 could not be assigned to an LTR since it covers only few meters of the atmosphere above the SI. It is therefore left out in the following discussion. In the following paragraphs the influence of atmospheric observations on LTRS is discussed, with a focus on conditions at the site, regional airflow conditions and topography, and radiative forcing.

Surface flow and dynamic stability at synoptic time scale, as categorized by boundary layer regimes (BLRs) in 3.1.2, showed no agreement with LTRs. Hence, surface flow and stability conditions over periods of several hours did not generate typical layer and inversion patterns over Ny-Ålesund in the analyzed data.

When looking at immediate surface flow conditions during the experiments, LTR2 was associated with the intermittent presence of strong southeast winds at the surface during the experiment, with wind speeds  $U > 2.5 \text{ m s}^{-1}$  at 2 m agl. A connection between surface flow and sublayer characteristics above the SI was to be expected under these wind conditions, since strong southeasterly winds typically prevail in the entire depth of wind channeling along Kongsfjorden (Beine et al., 2001; Maturilli and Kayser, 2017). These uniform strong southeast winds were observed in SODAR data during 180921 (Fig. 3.7d). However, the strong winds at the surface occurred for less than 10 % of LTR2 data. For weak winds from all directions or katabatic winds from southwest, wind direction and dynamic stability patterns at the surface during experiments were no meaningful predictors of LTRs. For instance, weak southeast winds with

dynamically stable conditions at similar  $Ri$  values were found for 180910 and 180918, which belonged to different LTRs. In conclusion, the only relevant relationship between surface conditions and LTRs was the one between occurrence of strong southeast winds and LTR2.

The impact of synoptic advection and subsidence on LTRs was inferred from NCEP/NCAR reanalysis data. Cold air was advected for 180913 at 850 hPa, warm-air advection occurred for 180910 and 180911, but no temperature advection was found for the other three experiments. Since cold-air advection above an air mass does not force the formation of inversions, it does not explain the strong long-lived LIs for 180913. Further, 180916, 180918 and 180921 all showed multiple LIs without any observable temperature advection at 850 hPa. Thus, no influence of large-scale advection of heat with free-atmosphere flow on LTRs could be found. Subsidence was indicated for all experiments at 850 hPa by vertical air motion  $\omega$  from reanalysis data. Hence, variability of atmospheric structure between LTRs could not be explained by synoptic subsidence effects. These observations point out that advection and subsidence as typical generation mechanisms of LIs were not responsible on a synoptic scale for the LIs observed in the fiber-optic profiles. This deduction is substantiated by the lack of cloud cover which typically forms accompanying advection- and subsidence-generated LIs (Busch et al., 1982; Wetzel and Brümmer, 2011).

Since temperature inversions are commonly formed by radiative cooling of earth's surface, the role of radiative forcing in the generation of LIs and the observed LTRs was investigated. Both experiments of LTR3 were recorded around sunrise (Fig. 2.2) and were associated with stronger and more long-lived LIs than for LTR1 and LTR2. At diminishing insolation  $K\downarrow$  in the afternoon and evening, LTR1 and LTR2 showed weakly stable or near-neutral conditions throughout most of the profiles. Within LTR3, 180918 exhibited a deeper SI and overall higher  $LSS$  than 180913 which was probably due to the presence of snow which fell on September 16, leading to almost permanent radiative cooling at the surface afterwards, indicated by positive  $Q_S^*$  (Fig. 3.1j). 180921 also captured the period shortly after sunrise with low solar angles and snow cover, but the strong winds from southeast in the night from September 20 to September 21 (Fig. 3.2) probably prevented the formation of an equally strong stability. These observations indicate that the diurnal course of net radiation  $Q_S^*$  in the area surrounding Ny-Ålesund strongly impacted the generation of LIs, where surface cooling at low solar angles forced spatially homogeneous and strong LIs. Thus, regional radiative forcing was likely the key mechanism governing LTRs through the generation of temperature inversions via surface cooling.

The connection between LTRs and topographically modified airflow was tested to explain how temperature inversions generated by radiative surface cooling could result in a vertical atmospheric structure containing multiple LIs. Temperature inversions generated by radiative surface cooling in heterogeneous mountainous terrain are known to be lifted when transported by downvalley and downslope winds (Emeis et al., 2007). Further, downslope cold-air drainage flow can be lifted if adiabatic warming results in a lower density of the draining air masses relative to the surrounding air, leading to the formation of lifted inversions (Fig. 9b in Vihma et al. (2011)). Distinct wind shear associated with LIs was observed in SODAR, FireFOX and radiosonde data. Although the connection between LIs and wind shear became evident from the data no correlation between LTRs and wind speed shear or wind directional shear was found. In conclusion, observations indicate that LIs in the fiber-optic profiles were typically generated as SIs in the surrounding mountainous area of Spitsbergen at varying elevations and transported

by channeled downvalley and downslope winds to the fiber-optic profiles.

An effect of strong channeled winds along Kongsfjorden on LTR classification was observed: Agreeing with southeasterly winds being intermittently present at the surface in LTR2, a strong channeled southeasterly airflow was found for LTR2, with southeasterly and easterly winds above the SI up to the 850 hPa level (Tab. 3.1, Fig. D.13). These channeled winds were associated with high geostrophic wind speeds on September 21. On September 11 wind speeds within the fiber-optic profiles greatly exceeded the weak winds at 850 hPa, suggesting that the exact alignment of the geostrophic wind along Kongsfjorden and Kongsvegen glacier caused an amplification and deepening of the channeling effect due to downward acceleration of the flow over Spitsbergen (see also Skeie and Grønås, 2000). The strong channeled southeast wind observed in LTR2 likely decreased heterogeneity of mountain–valley circulations which explains the lower stability observed in the fiber-optic profiles in LTR2 compared to LTR3. Further, high wind speeds and wind shear may have caused more vigorous intermittent turbulent mixing in the lower troposphere, which then prevented the buildup of strong temperature inversions.

To conclude, the analyses provide strong evidence that LIs were neither generated in association with synoptic advection or subsidence, nor were they correlated to surface conditions in Ny-Ålesund. Instead, a combination of regionally forced radiation inversions and topographically modified airflow was responsible for the observed patterns in LIs.

### 3.9. Implications for research on lower Arctic troposphere

While this work showcases the possibilities of detailed atmospheric measurements introduced by FLYFOX, the findings of this study do not describe climatic conditions above Ny-Ålesund with statistical meaningfulness, since measurements were restricted to a season with significant diurnal variation of insolation, and to predominantly weak winds, which never reached speeds higher than  $10 \text{ m s}^{-1}$  within the profiles. Further, the small number of fiber-optic experiments cannot provide conclusive classification of observable regimes at the site.

Characteristic structures were identified for snow-free and snow-covered conditions, and varying flow modes in the lower troposphere at weak winds and light or absent cloud cover, which are likely representative for the site and similar regions in the Arctic with strong topography. Since the only afternoon measurements without snow cover on September 11 contained no temperature inversion within the lowermost 400 m agl, multiple inversions within heights influenced by topographic effects probably form less frequently at higher solar angles, especially during polar day. This would be an opposite seasonal pattern to the occurrence of deeper LIs formed by advection and subsidence, which show highest frequency in the summer season (Serreze et al., 1992; Wetzel and Brümmer, 2011). However, low static stability at the site is generated by shear rather than buoyancy year-round because of weak solar irradiance even during polar day (Schulz, 2017). Hence, topographically forced LIs may be a common feature under weak-wind and cloudless conditions above Ny-Ålesund throughout the year. A consistent SI at the surface, and multiple LIs within the lowest 600 m agl were always present under snow-covered and cloudless conditions. However, winds higher than  $2.5 \text{ m s}^{-1}$  have the ability to erode the SI even in the polar night, and generate continuous turbulence up to heights of more than 1 km (Schulz, 2017). Under such conditions, no LIs are likely within these heights.

Since similar observations of multiple thin LIs with strong temporal height oscillations have

been made at high latitudes over flat terrain under snow-covered conditions (Cheung, 1991; Anderson, 2003), they may be a ubiquitous feature in the stably-stratified lower Arctic troposphere at low solar angles. These inversions may be generated in regions with significant topography and transported over far distances in stably-stratified air. Since LIs are such a defining feature of the lower Arctic troposphere under stably-stratified conditions, they are a major barrier for vertical exchange of matter and energy. However, observations of this study suggest that oscillations of LIs associated with IGWs can induce turbulent exchange within adjacent air masses with less stable stratification.

#### 3.10. Implications for future research, lessons learned

The FLYFOX approach provides a unique opportunity to record thermodynamics and dynamics in profiles in the lowermost kilometer of the troposphere at a high resolution of  $10^0$  m and  $10^1$  s. From the data presented in this thesis, novel insights into the variability and scales in the lower Arctic troposphere could be gained, where oscillations of stably stratified air masses and the highly varying wind field in the surface-based inversion at a topographically heterogeneous site were revealed via *in-situ* observations in sufficient detail.

While the vertical structure of the atmosphere is resolved through spatially distributed measurements, the technique still relies on Taylor's hypothesis of frozen turbulence like established point observations, converting a time series into an assumed horizontal structure in space. Therefore, with only one FLYFOX launch at a time no true two-dimensional measurement of the vertical and horizontal structure of the atmosphere is captured. It is thus not possible to distinguish the respective influences of horizontal heterogeneity and temporal changes in the atmosphere on the temporal variability in fiber-optic profiles.

FODS measurements on tethered balloons hold the potential of being a crucial part of boundary layer research, especially under conditions of weak wind and strong stability. An expanded setup with additional high-resolution aircraft data can reveal atmospheric dynamics at higher elevation. This will help identifying where and how turbulence is generated in the profile above the SI (e.g. Muschinski and Wode, 1998). This methodical combination will also help improving our understanding of the generation mechanisms of the observed NSEs. When variability of thin LIs, as analyzed in this thesis, are compared to simultaneous aerosol concentration measurements via LIDAR, the impact of these inversions on vertical exchange of matter can be directly displayed.

Analysis of quadrature spectra of  $\theta_v$  records from IceFOX can reveal, if the height oscillations of LIs are caused by IGWs or other wavelike types of motions. The spatiotemporal profiles also enable investigation of the vertical propagation of IGWs.

Additional implementations of the FLYFOX technique to the one published by Keller et al. (2011) have already been accomplished in 2019 and 2020: Several flights were launched at a weak-wind site in a mountain valley in Southern Germany by the Micrometeorology Group of the University of Bayreuth, and, more closely connected to this thesis, regular FLYFOX experiments were launched during the MOSAiC campaign (Multidisciplinary drifting Observatory for the Study of Arctic Climate) by the Alfred-Wegener Institute, having received training in the technique by the Micrometeorology Group of the University of Bayreuth. These year-round high-resolution measurements of the lower troposphere in the high Arctic will further the under-

standing of dynamics and thermodynamics in the lower Arctic atmosphere and the role played by LIs.

This proof-of-concept study and the presented analyses highlight the merit of detailed observations of atmospheric thermodynamics and dynamics via FLYFOX. Owing to its novelty, some practical issues related to the technique were revealed which are discussed in the following paragraphs.

The single-ended FODS setup caused calibration issues, particularly associated with signal losses at fiber splices, which could not be entirely corrected post-hoc. This caused distinct temperature differences between fiber branches of up to 0.6 K. Since these problems depend upon the direction of laser pulses through the fibers, they can be mitigated by using a double-ended fiber setup, where both fiber ends are connected to the DTS device which allows sending laser pulses in two directions through the fiber. This would make double-ended calibration possible and reduce the error caused by the splices.

Correction of artifacts induced by fiber holders, particularly for FireFOX experiments, can be simplified by detailed mapping of their positions on the fiber. This includes fixating them at regular separation distances and maybe noting down their locations while setting up or launching the experiments. Some of the artifacts in FireFOX wind speeds were likely caused by entangling of the various cables. It remains to be seen whether this problem can be easily solved.

Physical mapping of the fibers, i.e., conversion of locations along the fiber to elevation above ground, was achieved for IceFOX with a linear approach with appropriate height accuracy. The same was not possible for the FireFOX setup, where the nonlinear shape of the fiber, caused by the greater weight of the installation, required a nontrivial correction routine. This was solved by fitting measurement bins of FireFOX to those of IceFOX via maximum correlation, and by inferring a non-numerical relationship between length along fiber and height above ground from this for FireFOX. This solution cannot be viewed as ideal, since it may suffer from large, non-quantifiable height uncertainty and is only possible if an IceFOX setup is recording simultaneously. Thus, the development of a different approach to the height correction issue is recommended for future implementations.

Artificial temperature offsets and variability in the Pt-100 reference temperatures within the calibration baths were caused by electric induction by the stainless-steel coated fibers. These signal distortions can be overcome relatively well by the applied correction approach consisting of offset correction and wavelet filtering. However, this issue can be avoided by using newly developed solid-phase baths instead of water baths. These solid-phase baths are also more appropriate for calibrating fiber-optic data in cold environments than water baths, since the latter ones cannot generate reference temperatures far below 0 °C.

The yielded temperature and wind profiles contained substantial small-scale noise at the original resolution of 0.25 m, possibly creating artificial signal variation along the fiber with scales of up to 4 m. I removed scales below 1.57 m via wavelet filtering, but the remaining data may still contain fictitious variability. A thorough estimation of noise in the data was not pursued in this work, but needs to be done to provide a reliable representation of errors in FLYFOX measurements.

The analysis of the newly developed sublayer detection algorithm showed that it performs well at defining ILs. The method succeeded in identifying shallow inversions with thickness of a few meters. However, spatiotemporally incoherent inversions were not recognized as one

entity, but as very short-lived individual ILs which often were discarded due to short duration. In the final merging of sublayers, this caused the generation of very deep NILs, which were actually divided by inversions. Thus, some detected NILs represented multiple layers, and could not be interpreted in a meaningful way. When more realistic near-neutral layers are to be detected from fiber-optic temperatures, it may be viable detect NILs as isothermal samples of the atmospheric profiles, with uniform  $\theta_v$  coherently in space and time, while ILs are the transitional air masses between NILs. Thresholds for minimum layer duration and minimum  $LSS$  were chosen arbitrarily. Thresholds are therefore likely not universally applicable, but have to be altered between sites and meteorological conditions, and particularly between research questions.

Spectral analysis, as used in this thesis, is a crucial approach to extracting patterns from the large amount of data produced by fiber-optic measurements in the atmosphere. The methods presented here are just a starting point, showing possibilities and suggesting directions for future research. From the experience gained during this work, the conclusion is drawn that MRD of  $\theta_v$  over several hours and hundreds of meters provides a first estimate of the structures that are present in the fiber-optic data. A deeper analysis of finer structures in the atmosphere can be achieved by selecting smaller samples in time and space for the MRD. However, the comparability of temperature spectra of small structures such as LIs has been shown here to be complicated, and further steps need to be taken to yield meaningful results, for which this work may serve as a guideline.

---

## 4. Conclusion

In this thesis, a novel *in-situ* approach was presented for recording spatiotemporal variability of temperature and wind speed in the lower troposphere at high resolution. This method was based on fiber-optic distributed sensing on a tethered balloon, and was employed on 6 days in September 2018 at the Arctic research site Ny-Ålesund on Svalbard during predominantly weak-wind conditions. The recorded data were used to gain new insights into the vertical structure of the lower Arctic troposphere. An algorithm was developed and applied to categorize the vertical thermodynamic structure in the fiber-optic profiles, detecting spatiotemporally continuous temperature inversions and the less stable layers separated by the inversions. Structures in the profiles were analyzed using multiresolution decomposition on virtual potential temperatures, including a vertical length scale of motions based on spatial correlation decay between measurements.

The initially proposed hypotheses were mostly confirmed by the findings of this thesis:

- Instantaneous fiber-optic profiles contained between 0.7 and 3.5 inversions in the column averaged over experiments, lasting for more than 5 min and showing thickness between 10 m and more than 100 m, with a positive correlation between thickness and duration. Hence, the anticipated multi-layered vertical structure was present in the majority of data recorded in the campaign.
- Large wavelike height oscillations of lifted inversions were the most important cause for temperature variability above the surface-based inversion, peaking at submeso time scales. Amplitudes of these oscillations increased with layer thickness, and reached up to 200 m within a few minutes. Their time scales corresponded to those of potential internal gravity waves given by the Brunt-Väisälä Frequency.
- Temporal temperature variability within the fiber-optic profiles peaked at the surface, exceeding values above the surface-based inversion by more than a factor of 2. This surface peak was due to distinct events of shallow cold-air drainage from southwest which mainly affected the lowermost 20 m agl, and were most pronounced when snow cover was present. Turbulent sensible heat transfer towards the surface during katabatic flow from southwest indicated intermittent turbulence under very stable conditions with supercritical  $Ri$  at the surface. Observations of subcritical  $Ri$  in instantaneous fiber data throughout the lowermost 100 m, increasing in abundance with height in the lowest 70 m, implied intermittent generation of turbulence at sufficient shear in the surface-based inversion, despite the strong temperature inversions. Variability of wind speed and directions frequently caused the deepening or disruption of the surface-based inversion, particularly with deep cold-air advection where air masses were vertically displaced. This observed variability in dynamics and thermodynamics confirms that variation in footprints represented by wind directions caused distinct responses of the surface-based inversion.
- Neither surface flow and stability nor synoptic advection and subsidence were related to the thermodynamic structure of the atmosphere above the surface-based inversion. Instead, evidence was found that lifted inversions and their variability were impacted by topographic effects on airflow, with generation of lifted inversions as surface-based inversions

by radiative cooling at varying elevations in the heterogeneous and mountainous terrain surrounding Kongsfjorden and on the mainland of Spitsbergen, which were transported to the site by a combination of channeled winds and katabatic flow. Here, stronger winds, channeled from the inland ice along Kongsfjorden, were associated with weaker static stability, and with fewer, shallower, and strongly fluctuating lifted inversions than at weaker winds. Presence of snow cover and cloud-free conditions forced stronger static stability above the surface-based inversion at weak winds and was associated with longer-lived lifted inversions. In conclusion, observations point to the regional generation of lifted inversions by radiative cooling and their transport to the site by topographically modified airflow.

The employed analyses revealed further insights into the spatiotemporal variability in the lower Arctic troposphere:

Inertial subranges with maximum time scales between 30 s and 100 s found in spectral analyses of virtual potential temperatures indicated the common presence of cascade turbulence throughout the fiber-optic profiles. Above the surface-based inversion strongest turbulence was associated with lifted inversions and maximum time scales of this turbulence corresponded to minimum time scales of oscillations of lifted inversions, indicating a connection between inversion oscillations and production of cascade turbulence there.

Weakly stable stratification frequently developed into near-neutral stability within seconds or minutes across several hundreds of meters, which points to a strong horizontal heterogeneity of the lower troposphere. These neutral stability events are a potentially crucial promoter of vertical exchange in a stably-stratified lower Arctic troposphere.

Analysis of vertical length scales of motions revealed the flat shape of submeso-scale motions in the surface-based inversion under very stable conditions and corresponding weak coupling between surface-based inversion and the air above. Vertical length scales increased with height in the lowermost 100 m. The absence of a further increase in vertical length scale above this height provides evidence for the vertical restriction of large motions in a significantly structured lower atmosphere.

This proof-of-concept study constitutes a groundbreaking progress in atmospheric observations, as it showcases the plethora of research opportunities provided by the unprecedented resolution of the novel *in-situ* fiber-optic sensing method employed in the FLYFOX-A campaign: The analysis of the fiber-optic data enabled multiple novel insights into thermodynamics and dynamics in the lower Arctic troposphere, where observed phenomena are likely typical for high-latitude regions with close proximity to high-elevation topography. A profound statistical description of the climatic conditions at Ny-Ålesund cannot be gained from this work, since this requires more data systematically capturing a broad range of meteorological conditions across all seasons.

Further studies at multiple locations with varying surface properties will enable a more exhaustive analysis of the meteorological forcings of shallow lifted inversions and the general thermal structure of the lower Arctic troposphere, including a deeper investigation of the impacts of site and season. With an expanded setup that combines fiber-optic measurements with direct high-resolution turbulence measurements above the surface-based inversion, the role of lifted inversions as barriers or promoters of vertical exchange of heat and mass in the stably-stratified polar atmosphere will likely emerge. The sublayer detection algorithm developed in the course

---

of the thesis has proven as a powerful tool to identify lifted inversions. However, the detection of meaningful “non-inversion” layers with relatively homogeneous properties requires a refined version of the algorithm, which still needs to be developed. The findings of this work and future related research provide a basis for improvements of atmospheric circulation models via a more realistic parameterization of thermodynamic and dynamic variability and exchange processes in the stable lower troposphere.

## Acknowledgements

First, I thank my main supervisor, Christoph Thomas, for providing me with the opportunity to do my master thesis in such a fascinating place as Ny-Ålesund with such an innovative method as FLYFOX. I really enjoyed developing and launching the balloon experiments together with him and the AWI guys, discussing science, playing games and going hiking in this beautiful area. Christoph's excitement about this research was very motivating, and our long one-to-one meetings and his detailed feedback always gave me lots of ideas and impulses for my work.

This research would not have been possible without the support by the atmospheric physics people from AWI and their enthusiasm about FLYFOX. I thank Alex Schulz of the AWI for organizing our field stay, for protecting us from polar bears, and for giving me valuable feedback on my work. Further, I thank him and Jürgen "Egon" Gräser for constructing and launching FLYFOX together with Christoph and myself, and for being our "family" in Ny-Ålesund, together with Anja Sommerfeld. More thanks go to the AWIPEV staff who provided us with everything we needed while we were there, and even gave us a fascinating boat tour around Kongsfjorden. Cheers to Marion Maturilli for providing me with lots of data recorded at the site which served as reference for the fiber-optic measurements. Thanks to Markus Rex and Roland Neuber for inviting us to Ny-Ålesund!

Of the Micromet people in Bayreuth, I thank Karl Lapo for walking me through pyfocs, and for taking time to give me guidance and advice while I was developing my algorithms and searching for directions. My thanks go to Johann Schneider for preparing fiber holders and other useful stuff needed for FLYFOX, and to Jo Olesch and Lena Pfister for packing heaps of crates with equipment for us. Further thanks to Lena Pfister for helping me getting started with the MRD. Also, I thank Anita Freundorfer for helping me with the wind speed calculation. Thanks to the entire Micromet group for listening to my long talks about complicated analyses and giving me feedback and encouragement.

Very special thanks go to my friends and family who were always very supportive and motivating. This particularly includes those who gave me very helpful feedback on my manuscript. And, last but not least, I thank Swetlana Fork who always listened to my thoughts and concerns and helped me through several crises during this project.

---

## References

- Acevedo, O. C., Moraes, O. L. L., Fitzjarrald, D. R., Sakai, R. K., and Mahrt, L.: Turbulent carbon exchange in very stable conditions, *Boundary-Layer Meteorology*, 125, 49–61, 2007.
- Acevedo, O. C., Costa, F. D., Oliveira, P. E. S., Puhales, F. S., Degrazia, G. A., and Roberti, D. R.: The Influence of Submeso Processes on Stable Boundary Layer Similarity Relationships, *Journal of the Atmospheric Sciences*, 71, 207–225, 2014.
- Anderson, P. S.: Fine-Scale Structure Observed In A Stable Atmospheric Boundary Layer By Sodar And Kite-Borne Tethersonde, *Boundary-Layer Meteorology*, 107, 323–351, 2003.
- Andreas, E. L., Claffy, K. J., and Makshtas, A. P.: Low-Level Atmospheric Jets And Inversions Over The Western Weddell Sea, *Boundary-Layer Meteorology*, 97, 459–486, 2000.
- Anfossi, D., Oetl, D., Degrazia, G., and Goulart, A.: An Analysis Of Sonic Anemometer Observations In Low Wind Speed Conditions, *Boundary-Layer Meteorology*, 114, 179–203, 2005.
- Argentini, S., Viola, A. P., Mastrantonio, G., Maurizi, A., Georgiadis, T., and Nardino, M.: Characteristics of the boundary layer at Ny-Ålesund in the Arctic during the ARTIST field experiment, *Annals of Geophysics*, 46, 2003.
- Argentini, S., Mastrantonio, G., Petenko, I., Pietroni, I., and Viola, A.: Use of a High-Resolution Sodar to Study Surface-layer Turbulence at Night, *Boundary-Layer Meteorology*, 143, 177–188, 2012.
- Baas, P., van de Wiel, B. J. H., van Meijgaard, E., Vignon, E., Genthon, C., van der Linden, S. J. A., and de Roode, S. R.: Transitions in the wintertime near-surface temperature inversion at Dome C, Antarctica, *Quarterly journal of the Royal Meteorological Society. Royal Meteorological Society (Great Britain)*, 145, 930–946, 2019.
- Beine, H. J., Argentini, S., Maurizi, A., Viola, A., and Mastrantonio, G.: The local wind field at Ny-lesund and the Zeppelin mountain at Svalbard, *Meteorology and Atmospheric Physics*, 78, 107–113, 2001.
- Belušić, D. and Mahrt, L.: Estimation of length scales from mesoscale networks, *Tellus A*, 60, 706–715, 2008.
- Belušić, D. and Mahrt, L.: Is geometry more universal than physics in atmospheric boundary layer flow?, *Journal of Geophysical Research: Atmospheres*, 117, 2012.
- Busch, N., Ebel, U., Kraus, H., and Schaller, E.: The structure of the subpolar inversion-capped ABL, *Meteorology and Atmospheric Physics*, 31, 1–18, 1982.
- Cheng, Y., Sayde, C., Li, Q., Basara, J., Selker, J., Tanner, E., and Gentine, P.: Failure of Taylor’s hypothesis in the atmospheric surface layer and its correction for eddy-covariance measurements, *Geophysical Research Letters*, 44, 4287–4295, 2017.
- Cheung, T. K.: Sodar observations of the stable lower atmospheric boundary layer at Barrow, Alaska, *Boundary-Layer Meteorology*, 57, 251–274, 1991.
- Chimonas, G.: Steps, Waves and Turbulence in the Stably Stratified Planetary Boundary Layer, *Boundary-Layer Meteorology*, 90, 397–421, 1999.

- Collineau, S. and Brunet, Y.: Detection of turbulent coherent motions in a forest canopy part I: Wavelet analysis, *Boundary-Layer Meteorology*, 65, 357–379, 1993.
- Dalaudier, F., Sidi, C., Crochet, M., and Vernin, J.: Direct Evidence of “Sheets” in the Atmospheric Temperature Field, *Journal of the Atmospheric Sciences*, 51, 237–248, 1994.
- Emeis, S., Münkkel, C., Vogt, S., Müller, W. J., and Schäfer, K.: Atmospheric boundary-layer structure from simultaneous SODAR, RASS, and ceilometer measurements, *Atmospheric Environment*, 38, 273–286, 2004.
- Emeis, S., Jahn, C., Münkkel, C., Münsterer, C., and Schäfer, K.: Multiple atmospheric layering and mixing-layer height in the Inn valley observed by remote sensing, *Meteorologische Zeitschrift*, 16, 415–424, 2007.
- Esau, I. and Repina, I.: Wind Climate in Kongsfjorden, Svalbard, and Attribution of Leading Wind Driving Mechanisms through Turbulence-Resolving Simulations, *Advances in Meteorology*, 2012, 1–16, 2012.
- Finnigan, J. J., Einaudi, F., and Fua, D.: The Interaction between an Internal Gravity Wave and Turbulence in the Stably-Stratified Nocturnal Boundary Layer, *Journal of the Atmospheric Sciences*, 41, 2409–2436, 1984.
- Fritts, D. C., Wang, L., Werne, J., Lund, T., and Wan, K.: Gravity Wave Instability Dynamics at High Reynolds Numbers. Part II: Turbulence Evolution, Structure, and Anisotropy, *Journal of the Atmospheric Sciences*, 66, 1149–1171, 2009.
- Galperin, B., Sukoriansky, S., and Anderson, P. S.: On the critical Richardson number in stably stratified turbulence, *Atmospheric Science Letters*, 8, 65–69, 2007.
- Gossard, E. E., Gaynor, J. E., Zamora, R. J., and Neff, W. D.: Finestructure of Elevated Stable Layers Observed by Sounder and In Situ Tower Sensors, *Journal of the Atmospheric Sciences*, 42, 2156–2169, 1985.
- Grachev, A. A., Fairall, C. W., Persson, P. O. G., Andreas, E. L., and Guest, P. S.: Stable Boundary-Layer Scaling Regimes: The Sheba Data, *Boundary-Layer Meteorology*, 116, 201–235, 2005.
- Grachev, A. A., Andreas, E. L., Fairall, C. W., Guest, P. S., and Persson, P. O. G.: The Critical Richardson Number and Limits of Applicability of Local Similarity Theory in the Stable Boundary Layer, *Boundary-Layer Meteorology*, 147, 51–82, 2013.
- Hausner, M. B. and Kobs, S.: Identifying and Correcting Step Losses in Single-Ended Fiber-Optic Distributed Temperature Sensing Data, *Journal of Sensors*, 2016, 1–10, 2016.
- Hausner, M. B., Suárez, F., Glander, K. E., van de Giesen, N., Selker, J. S., and Tyler, S. W.: Calibrating single-ended fiber-optic Raman spectra distributed temperature sensing data, *Sensors*, 11, 10 859–10 879, 2011.
- Higgins, C. W., Froidevaux, M., Simeonov, V., Vercauteren, N., Barry, C., and Parlange, M. B.: The Effect of Scale on the Applicability of Taylor’s Frozen Turbulence Hypothesis in the Atmospheric Boundary Layer, *Boundary-Layer Meteorology*, 143, 379–391, 2012.

- Higgins, C. W., Wing, M. G., Kelley, J., Sayde, C., Burnett, J., and Holmes, H. A.: A high resolution measurement of the morning ABL transition using distributed temperature sensing and an unmanned aircraft system, *Environmental Fluid Mechanics*, 18, 683–693, 2018.
- Holtslag, A. A. M., Svensson, G., Baas, P., Basu, S., Beare, B., Beljaars, A. C. M., Bosveld, F. C., Cuxart, J., Lindvall, J., Steeneveld, G. J., Tjernström, M., and van de Wiel, B. J. H.: Stable Atmospheric Boundary Layers and Diurnal Cycles: Challenges for Weather and Climate Models, *Bulletin of the American Meteorological Society*, 94, 1691–1706, 2013.
- Hoover, J. D., Stauffer, D. R., Richardson, S. J., Mahrt, L., Gaudet, B. J., and Suarez, A.: Sub-meso Motions within the Stable Boundary Layer and Their Relationships to Local Indicators and Synoptic Regime in Moderately Complex Terrain, *Journal of Applied Meteorology and Climatology*, 54, 352–369, 2015.
- Howard, L. N.: Note on a paper of John W. Miles, *Journal of Fluid Mechanics*, 10, 509, 1961.
- Howell, J. F. and Mahrt, L.: Multiresolution Flux Decomposition, *Boundary-Layer Meteorology*, 83, 117–137, 1997.
- Hunt, J., Shutts, G. J., and Derbyshire, S. H.: Stably stratified flows in meteorology, *Dynamics of Atmospheres and Oceans*, 23, 63–79, 1996.
- Jocher, G., Karner, F., Ritter, C., Neuber, R., Dethloff, K., Obleitner, F., Reuder, J., and Foken, T.: The Near-Surface Small-Scale Spatial and Temporal Variability of Sensible and Latent Heat Exchange in the Svalbard Region: A Case Study, *ISRN Meteorology*, 2012, 1–14, 2012.
- Jocher, G., Schulz, A., Ritter, C., Neuber, R., Dethloff, K., and Foken, T.: The Sensible Heat Flux in the Course of the Year at Ny-Ålesund, Svalbard: Characteristics of Eddy Covariance Data and Corresponding Model Results, *Advances in Meteorology*, 2015, 1–16, 2015.
- Kahl, J. D.: Characteristics of the low-level temperature inversion along the Alaskan Arctic coast, *International Journal of Climatology*, 10, 537–548, 1990.
- Kallistratova, M. A., Petenko, I. V., Kouznetsov, R. D., Kulichkov, S. N., Chkhetiani, O. G., Chunchusov, I. P., Lyulyukin, V. S., Zaitseva, D. V., Vazaeva, N. V., Kuznetsov, D. D., Perepelkin, V. G., and Bush, G. A.: Sodar Sounding of the Atmospheric Boundary Layer: Review of Studies at the Obukhov Institute of Atmospheric Physics, Russian Academy of Sciences, *Izvestiya, Atmospheric and Oceanic Physics*, 54, 242–256, 2018.
- Kalnay, E., Kanamitsu, M., Kistler, R., Collins, W., Deaven, D., Gandin, L., Iredell, M., Saha, S., White, G., Woollen, J., Zhu, Y., Leetmaa, A., Reynolds, R., Chelliah, M., Ebisuzaki, W., Higgins, W., Janowiak, J., Mo, K. C., Ropelewski, C., Wang, J., Jenne, R., and Joseph, D.: The NCEP/NCAR 40-Year Reanalysis Project, *Bulletin of the American Meteorological Society*, 77, 437–471, 1996.
- Keller, C. A., Huwald, H., Vollmer, M. K., Wenger, A., Hill, M., Parlange, M. B., and Reimann, S.: Fiber optic distributed temperature sensing for the determination of the nocturnal atmospheric boundary layer height, *Atmospheric Measurement Techniques*, 4, 143–149, 2011.
- Kilpeläinen, T. and Sjöblom, A.: Momentum and Sensible Heat Exchange in an Ice-Free Arctic Fjord, *Boundary-Layer Meteorology*, 134, 109–130, 2010.

- Kilpeläinen, T., Vihma, T., Lafsson, H., and Karlsson, P. E.: Modelling of spatial variability and topographic effects over Arctic fjords in Svalbard, *Tellus A: Dynamic Meteorology and Oceanography*, 63, 223–237, 2011.
- Lapo, K. and Freundorfer, A.: *klapo/pyfocs v0.5*, <https://doi.org/10.5281/zenodo.4292490>, 2020.
- Lapo, K., Freundorfer, A., Pfister, L., Schneider, J., Selker, J., and Thomas, C.: Distributed observations of wind direction using microstructures attached to actively heated fiber-optic cables, *Atmospheric Measurement Techniques*, 13, 1563–1573, 2020.
- Lyulyukin, V., Kallistratova, M., Zaitseva, D., Kuznetsov, D., Artamonov, A., Repina, I., Pertenko, I., Kouznetsov, R., and Pashkin, A.: Sodar Observation of the ABL Structure and Waves over the Black Sea Offshore Site, *Atmosphere*, 10, 811, 2019.
- Mahrt, L.: Grid-Averaged Surface Fluxes, *Monthly Weather Review*, 115, 1550–1560, 1987.
- Mahrt, L.: Stably Stratified Atmospheric Boundary Layers, *Annual Review of Fluid Mechanics*, 46, 23–45, 2014.
- Mahrt, L. and Vickers, D.: Contrasting vertical structures of nocturnal boundary layers, *Boundary-Layer Meteorology*, 105, 351–363, 2002.
- Mahrt, L., Thomas, C. K., and Prueger, J. H.: Space-time structure of mesoscale motions in the stable boundary layer, *Quarterly Journal of the Royal Meteorological Society*, 135, 67–75, 2009.
- Mahrt, L., Richardson, S., Seaman, N., and Stauffer, D.: Turbulence in the nocturnal boundary layer with light and variable winds, *Quarterly Journal of the Royal Meteorological Society*, 138, 1430–1439, 2012.
- Mahrt, L., Thomas, C., Richardson, S., Seaman, N., Stauffer, D., and Zeeman, M.: Non-stationary Generation of Weak Turbulence for Very Stable and Weak-Wind Conditions, *Boundary-Layer Meteorology*, 147, 179–199, 2013.
- Mahrt, L., Pfister, L., and Thomas, C. K.: Small-Scale Variability in the Nocturnal Boundary Layer, *Boundary-Layer Meteorology*, 174, 81–98, 2020.
- Maturilli, M.: Continuous meteorological observations at station Ny-Ålesund (2018-09), PANGAEA, 2019a.
- Maturilli, M.: Basic and other measurements of radiation at station Ny-Ålesund (2018-09), PANGAEA, 2019b.
- Maturilli, M.: Expanded measurements from station Ny-Ålesund (2019-09), PANGAEA, 2019c.
- Maturilli, M.: High resolution radiosonde measurements from station Ny-Ålesund (2019-09), PANGAEA, 2019d.
- Maturilli, M. and Kayser, M.: Arctic warming, moisture increase and circulation changes observed in the Ny-Ålesund homogenized radiosonde record, *Theoretical and Applied Climatology*, 130, 1–17, 2017.

- Maturilli, M., Herber, A., and König-Langlo, G.: Climatology and time series of surface meteorology in Ny-Ålesund, Svalbard, *Earth System Science Data*, 5, 155–163, 2013.
- Miles, J. W.: On the stability of heterogeneous shear flows, *Journal of Fluid Mechanics*, 10, 496, 1961.
- Monin, A. S. and Obukhov, A. M.: Osnovnye zakonomernosti turbulentnogo peremesivaniya v prizemnom sloe atmosfery, *Tr. Geofiz. inst. AN SSSR*, 24, 163–187, 1954.
- Muschinski, A. and Wode, C.: First In Situ Evidence for Coexisting Submeter Temperature and Humidity Sheets in the Lower Free Troposphere\*, *Journal of the Atmospheric Sciences*, 55, 2893–2906, 1998.
- Muschinski, A., Frehlich, R. G., and Balsley, B. B.: Small-scale and large-scale intermittency in the nocturnal boundary layer and the residual layer, *Journal of Fluid Mechanics*, 515, 319–351, 2004.
- Palo, T., Vihma, T., Jaagus, J., and Jakobson, E.: Observations of temperature inversions over central Arctic sea ice in summer, *Quarterly Journal of the Royal Meteorological Society*, 143, 2741–2754, 2017.
- Petenko, I., Mastrantonio, G., Viola, A., Argentini, S., and Pietroni, I.: Wavy Vertical Motions in the ABL Observed by Sodar, *Boundary-Layer Meteorology*, 143, 125–141, 2012.
- Petenko, I., Argentini, S., Casasanta, G., Genthon, C., and Kallistratova, M.: Stable Surface-Based Turbulent Layer During the Polar Winter at Dome C, Antarctica: Sodar and In Situ Observations, *Boundary-Layer Meteorology*, 171, 101–128, 2019.
- Pfister, L., Sigmund, A., Olesch, J., and Thomas, C. K.: Nocturnal Near-Surface Temperature, but not Flow Dynamics, can be Predicted by Microtopography in a Mid-Range Mountain Valley, *Boundary-Layer Meteorology*, 165, 333–348, 2017.
- Pfister, L., Lapo, K., Sayde, C., Selker, J., Mahrt, L., and Thomas, C. K.: Classifying the nocturnal atmospheric boundary layer into temperature and flow regimes, *Quarterly Journal of the Royal Meteorological Society*, 145, 1515–1534, 2019.
- Poulos, G. S. and Burns, S. P.: An Evaluation of Bulk Ri-Based Surface Layer Flux Formulas for Stable and Very Stable Conditions with Intermittent Turbulence, *Journal of the Atmospheric Sciences*, 60, 2523–2537, 2003.
- Sayde, C., Thomas, C. K., Wagner, J., and Selker, J.: High-resolution wind speed measurements using actively heated fiber optics, *Geophysical Research Letters*, 42, 10,064–10,073, 2015.
- Schulz, A.: Untersuchung der Wechselwirkung synoptisch-skaliger mit orographisch bedingten Prozessen in der arktischen Grenzschicht über Spitzbergen, Potsdam, 2017.
- Selker, J. S., Thévenaz, L., Huwald, H., Mallet, A., Luxemburg, W., van de Giesen, N., Stejskal, M., Zeman, J., Westhoff, M., and Parlange, M. B.: Distributed fiber-optic temperature sensing for hydrologic systems, *Water Resources Research*, 42, 1038, 2006.
- Serreze, M. C., Schnell, R. C., and Kahl, J. D.: Low-Level Temperature Inversions of the Eurasian Arctic and Comparisons with Soviet Drifting Station Data, *Journal of Climate*, 5, 615–629, 1992.

- Sigmund, A., Pfister, L., Sayde, C., and Thomas, C. K.: Quantitative analysis of the radiation error for aerial coiled-fiber-optic distributed temperature sensing deployments using reinforcing fabric as support structure, *Atmospheric Measurement Techniques*, 10, 2149–2162, 2017.
- Skeie, P. and Grønås, S.: Strongly stratified easterly flows across Spitsbergen, *Tellus A: Dynamic Meteorology and Oceanography*, 52, 473–486, 2000.
- Smedman, A.-S.: Observations of a multi-level turbulence structure in a very stable atmospheric boundary layer, *Boundary-Layer Meteorology*, 44, 231–253, 1988.
- Sorbjan, Z. and Balsley, B. B.: Microstructure of Turbulence in the Stably Stratified Boundary Layer, *Boundary-Layer Meteorology*, 129, 191–210, 2008.
- Stull, R. B.: An introduction to boundary layer meteorology, Kluwer Academic Publishers, Dordrecht, 1988.
- Sun, J., Lenschow, D. H., Burns, S. P., Banta, R. M., Newsom, R. K., Coulter, R., Frasier, S., Ince, T., Nappo, C., Balsley, B. B., Jensen, M., Mahrt, L., Miller, D., and Skelly, B.: Atmospheric Disturbances that Generate Intermittent Turbulence in Nocturnal Boundary Layers, *Boundary-Layer Meteorology*, 110, 255–279, 2004.
- Sun, J., Mahrt, L., Banta, R. M., and Pichugina, Y. L.: Turbulence Regimes and Turbulence Intermittency in the Stable Boundary Layer during CASES-99, *Journal of the Atmospheric Sciences*, 69, 338–351, 2012.
- Sun, J., Nappo, C. J., Mahrt, L., Belušić, D., Grisogono, B., Stauffer, D. R., Pulido, M., Staquet, C., Jiang, Q., Pouquet, A., Yagüe, C., Galperin, B., Smith, R. B., Finnigan, J. J., Mayor, S. D., Svensson, G., Grachev, A. A., and Neff, W. D.: Review of wave–turbulence interactions in the stable atmospheric boundary layer, *Reviews of Geophysics*, 53, 956–993, 2015.
- Taylor, G. I.: The spectrum of turbulence, *Proceedings of the Royal Society of London. Series A*, 164, 476–490, 1938.
- Thomas, C. and Foken, T.: Detection of long-term coherent exchange over spruce forest using wavelet analysis, *Theoretical and Applied Climatology*, 80, 91–104, 2005.
- Thomas, C. and Selker, J. S.: Optical fiber-based distributed sensing methods, in: *Handbook of Atmospheric Measurements*, edited by Foken, T., p. 1705pp., Springer International Publishing, 2021.
- Thomas, C. K.: Variability of Sub-Canopy Flow, Temperature, and Horizontal Advection in Moderately Complex Terrain, *Boundary-Layer Meteorology*, 139, 61–81, 2011.
- Thomas, C. K., Law, B. E., Irvine, J., Martin, J. G., Pettijohn, J. C., and Davis, K. J.: Seasonal hydrology explains interannual and seasonal variation in carbon and water exchange in a semiarid mature ponderosa pine forest in central Oregon, *Journal of Geophysical Research*, 114, 714, 2009.
- Thomas, C. K., Kennedy, A. M., Selker, J. S., Moretti, A., Schroth, M. H., Smoot, A. R., Tuffiaro, N. B., and Zeeman, M. J.: High-Resolution Fibre-Optic Temperature Sensing: A New Tool to Study the Two-Dimensional Structure of Atmospheric Surface-Layer Flow, *Boundary-Layer Meteorology*, 142, 177–192, 2012.

- Tyler, S. W., Selker, J. S., Hausner, M. B., Hatch, C. E., Torgersen, T., Thodal, C. E., and Schladow, S. G.: Environmental temperature sensing using Raman spectra DTS fiber-optic methods, *Water Resources Research*, 45, 951, 2009.
- van de Wiel, B. J. H., Moene, A. F., Jonker, H. J. J., Baas, P., Basu, S., Donda, J. M. M., Sun, J., and Holtslag, A. A. M.: The Minimum Wind Speed for Sustainable Turbulence in the Nocturnal Boundary Layer, *Journal of the Atmospheric Sciences*, 69, 3116–3127, 2012.
- Vercauteren, N. and Klein, R.: A Clustering Method to Characterize Intermittent Bursts of Turbulence and Interaction with Submesoscale Motions in the Stable Boundary Layer, *Journal of the Atmospheric Sciences*, 72, 1504–1517, 2015.
- Viana, S., Yagüe, C., and Maqueda, G.: Vertical structure of the stable boundary layer detected by RASS-SODAR and in-situ measurements in SABLES 2006 field campaign, *Acta Geophysica*, 60, 1261–1286, 2012.
- Vickers, D. and Mahrt, L.: The Cospectral Gap and Turbulent Flux Calculations, *Journal of Atmospheric and Oceanic Technology*, 20, 660–672, 2003.
- Vihma, T., Kilpeläinen, T., Manninen, M., Sjöblom, A., Jakobson, E., Palo, T., Jaagus, J., and Maturilli, M.: Characteristics of Temperature and Humidity Inversions and Low-Level Jets over Svalbard Fjords in Spring, *Advances in Meteorology*, 2011, 1–14, 2011.
- Vinnichenko, N. K.: The kinetic energy spectrum in the free atmosphere-1 second to 5 years, *Tellus*, 22, 158–166, 1970.
- Westermann, S., Lüers, J., Langer, M., Piel, K., and Boike, J.: The annual surface energy budget of a high-arctic permafrost site on Svalbard, Norway, *The Cryosphere*, 3, 245–263, 2009.
- Wetzel, C. and Brümmner, B.: An Arctic inversion climatology based on the European Centre Reanalysis ERA-40, *Meteorologische Zeitschrift*, 20, 589–600, 2011.
- Zeeman, M. J., Selker, J. S., and Thomas, C. K.: Near-Surface Motion in the Nocturnal, Stable Boundary Layer Observed with Fibre-Optic Distributed Temperature Sensing, *Boundary-Layer Meteorology*, 154, 189–205, 2015.

# Appendices

## A. Fiber-optic distributed sensing

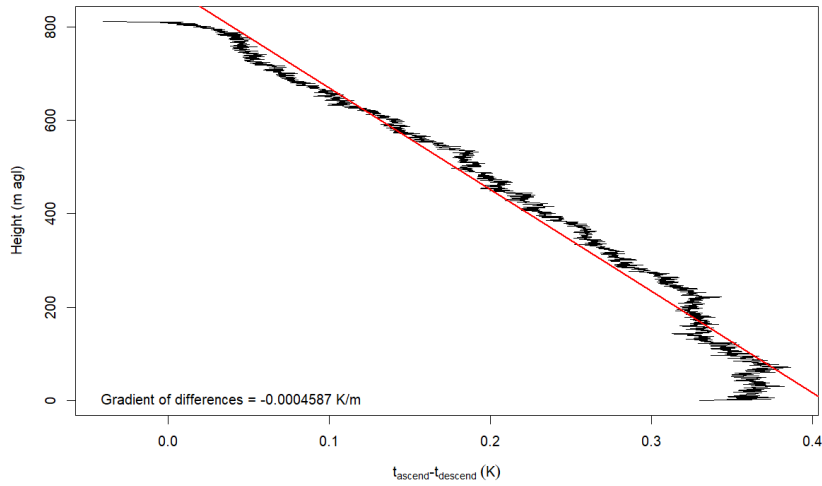


Figure A.1 Differences in fiber temperatures between ascending and descending branch of profile for 180913.

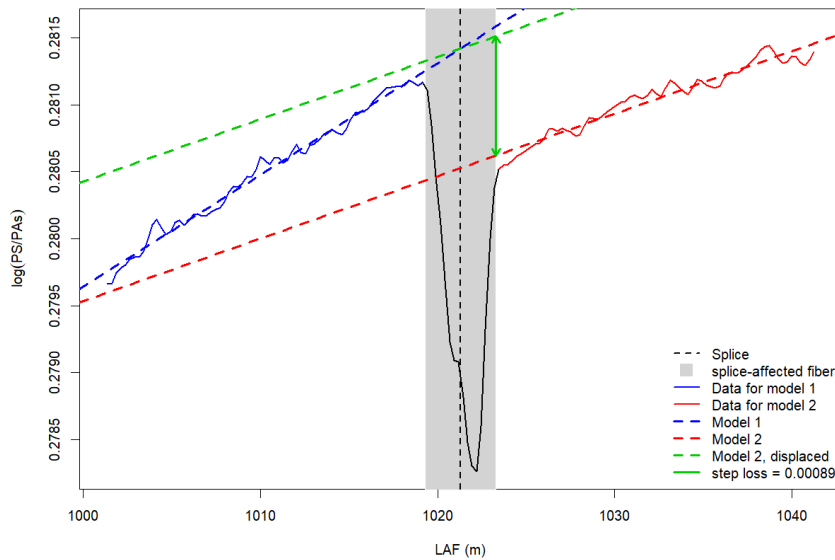
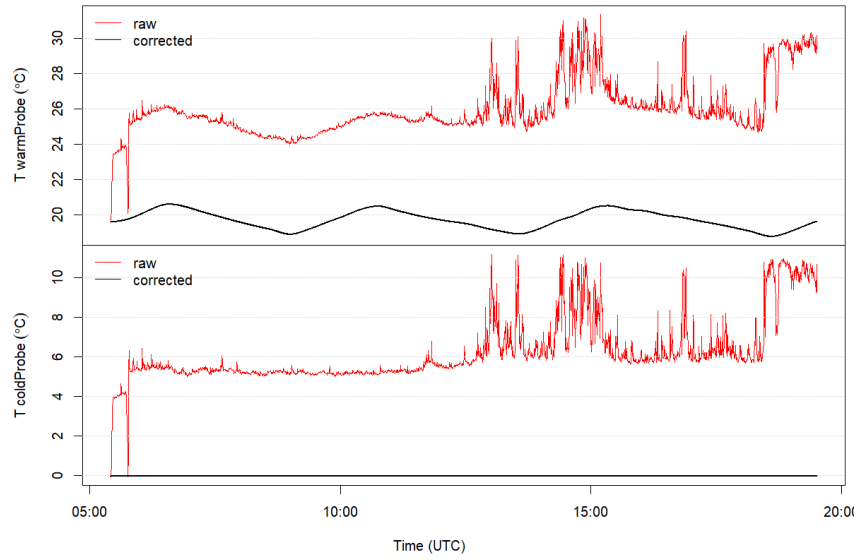


Figure A.2 Estimating step losses of log ratio of Raman Stokes and Antistokes for 180913.

**Table A.1** Parameters used for step loss correction: Locations along fiber of step loss ( $z_{sl}$ ), start ( $z_1$ ) and end ( $z_2$ ) of splice-affected fiber section; differential attenuation parameters in front of ( $\Delta\alpha_1$ ) and behind ( $\Delta\alpha_2$ ) the splice-affected fiber section determined with linear regression; estimated step loss ( $\Delta x_{S,As}$ ) at  $z_{sl}$ . Step losses were corrected at the intended splice connecting the two fiber branches, except for 180918, where two additional corrections were performed at different splices

Experiment	$z_{sl}$ (m af)	$z_1$ (m af)	$z_2$ (m af)	$\Delta\alpha_1$ (m s <sup>-1</sup> )	$\Delta\alpha_2$ (m s <sup>-1</sup> )	$\Delta x_{S,As}$ (-)
180910	1064.5	1062.5	1066.5	$8.93 \times 10^{-5}$	$4.93 \times 10^{-5}$	$7.79 \times 10^{-4}$
180911	1021.1	1019.6	1023.6	$1.09 \times 10^{-4}$	$6.79 \times 10^{-6}$	$5.17 \times 10^{-4}$
180913	1021.3	1019.3	1023.3	$8.33 \times 10^{-5}$	$4.67 \times 10^{-5}$	$8.93 \times 10^{-4}$
180918	1019.8	1017.8	1022.3	$8.31 \times 10^{-5}$	$4.12 \times 10^{-5}$	$3.17 \times 10^{-4}$
180918 2	384.2	382.7	385.7	$1.88 \times 10^{-5}$	$3.60 \times 10^{-5}$	$1.36 \times 10^{-4}$
180918 3	1656.0	1654.7	1657.3	$8.46 \times 10^{-5}$	$1.08 \times 10^{-4}$	$3.26 \times 10^{-4}$
180921	1019.4	1016.8	1021.9	$9.91 \times 10^{-5}$	$3.67 \times 10^{-5}$	$6.60 \times 10^{-4}$



**Figure A.3** Correcting the resistance thermometer temperatures for 180921.

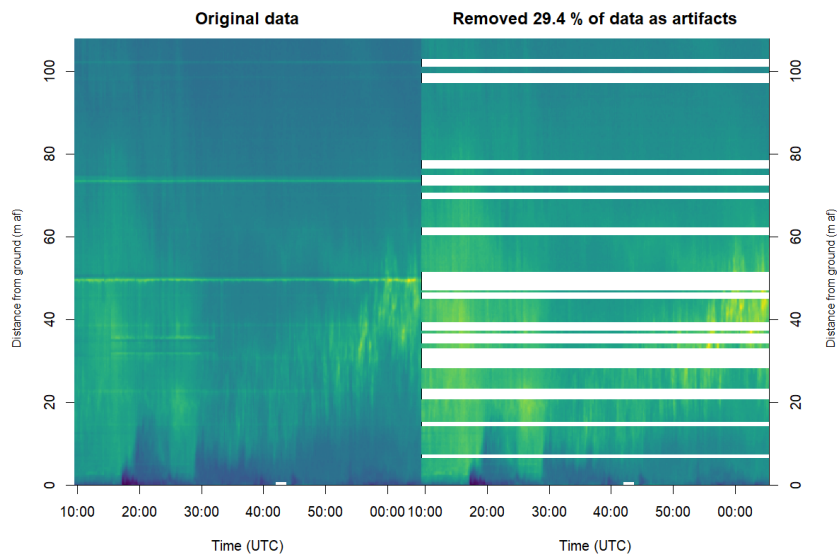


Figure A.4 Removing fiber holder artifacts in the fiber temperatures for ascending branch of 180916 FireFOX.

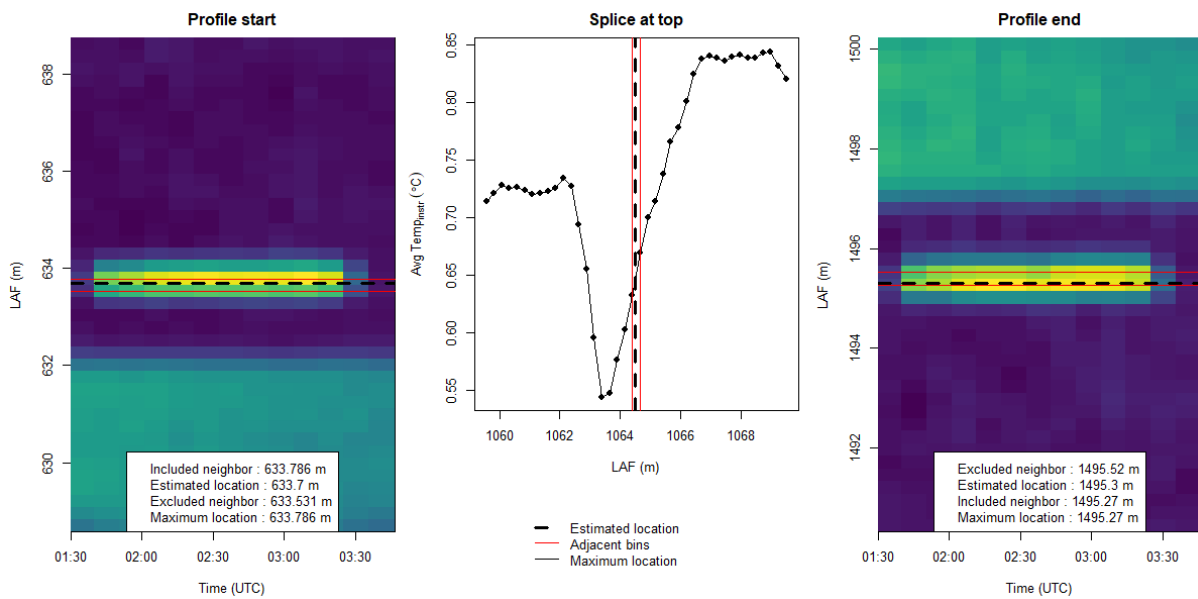
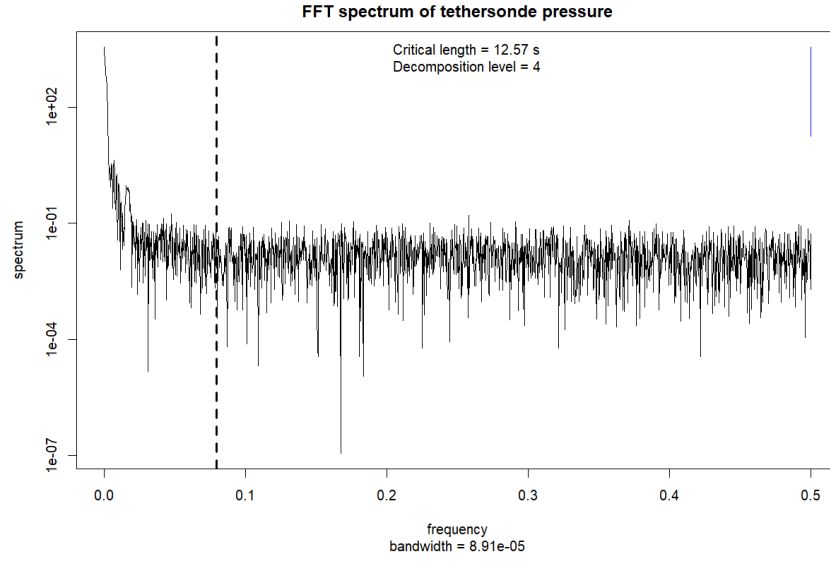


Figure A.5 Defining the start, top and end of the fiber section within the atmospheric profile via manually induced temperature pulses at the start and end and defining the center location along fiber between them as the profile top where the fibers were spliced together. Example taken from 180910.



**Figure A.6** FFT spectrum of tetheronde pressure while tetheronde was located at ground level during 180916 experiment. Decomposition level and critical length are values chosen for the denoising of tetheronde data with the BIOR5.5 set of wavelets.

**Table A.2** Relationships between distance along fiber from ground ( $d_f$ ) of FireFOX and IceFOX, manually defined via temporal correlations of unheated fiber temperatures over the entire experiment duration for all experiments with FireFOX deployment.  $d_f$  of IceFOX for individual flights is shown in the rightmost three columns. The exemplary relationship between  $d_{f,\text{FireFOX}}$  and  $d_{f,180918}$  is displayed in Fig. A.7 as blue dots and line. Since there was no IceFOX deployment for 180916 the values, taken from 180918, show a theoretical  $d_f$  that was used to infer the fiber heights above ground level.

$d_{f,\text{FireFOX}}$ (m af)	$d_{f,180916}$ (m af)	$d_{f,180918}$ (m af)	$d_{f,180921}$ (m af)
0	0	0	0
5	2	2	1
10	5	5	3
14	8	8	-
20	14	14	9
40	34	34	21

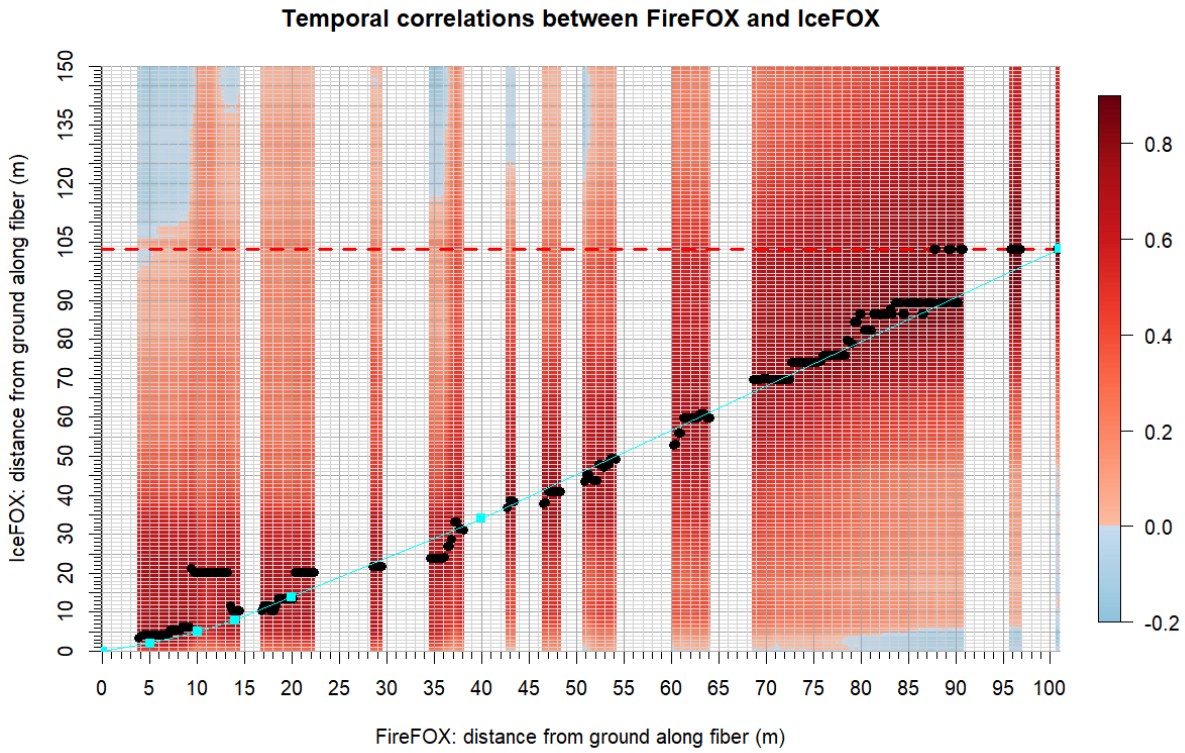


**Figure A.7** Defining the relationship between distance along fiber from ground ( $d_f$ ) of FireFOX and IceFOX via temporal correlations of unheated fiber temperatures over the entire experiment duration. Black dots show the location of maximum correlations for each FireFOX bin, red dotted line specifies the IceFOX  $d_f$  corresponding to the top of the FireFOX profile, blue dots and line indicate the manually defined relationship. Example taken from 180918.

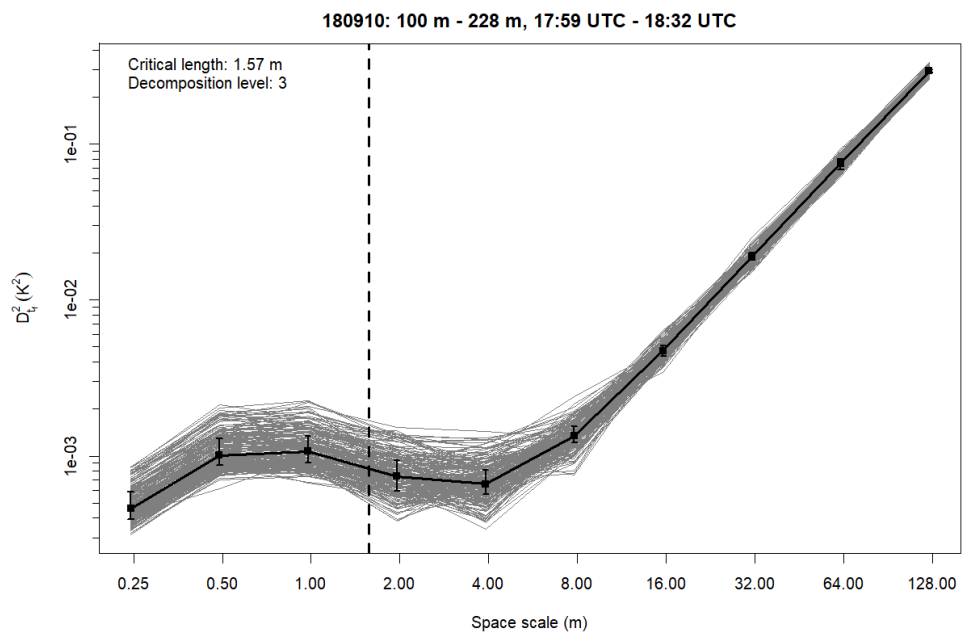


**Figure A.8** Spatial MRD spectra of fiber temperatures for a sample of 180910 experiment showing neutral stability. Chosen critical length for wavelet filtering shown by broken line, along with corresponding decomposition level for the BIOR5.5 filter.

## B. Detecting sublayers

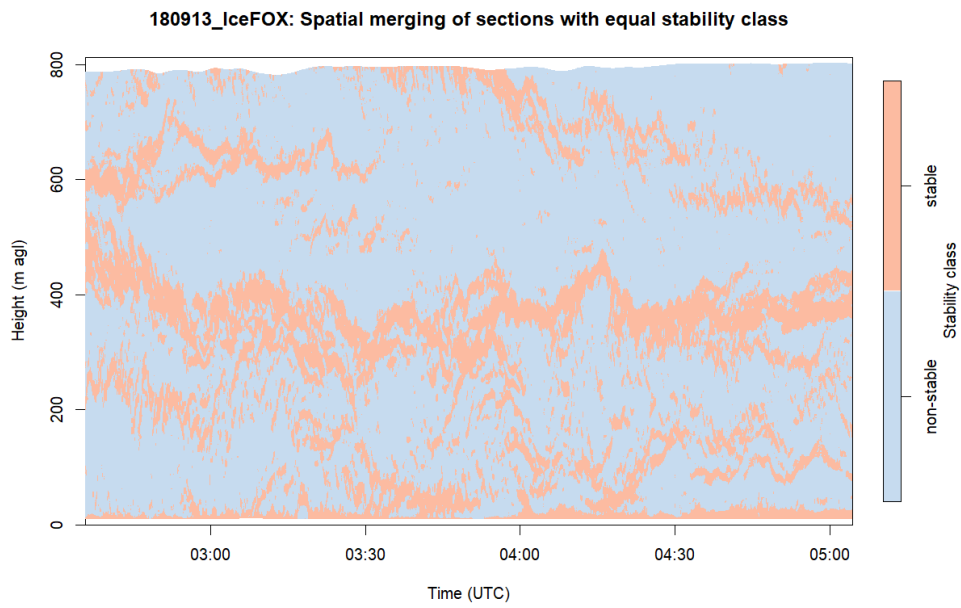


**Figure B.1** Sublayer detection, step 1: spatial merging of sections with equal stability class for 180913. For more information see 2.4.

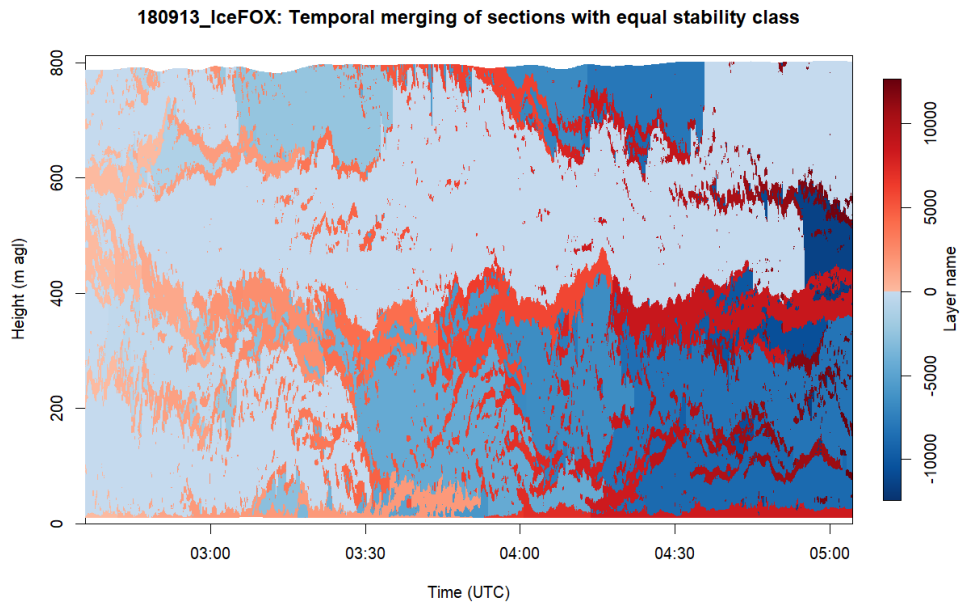


**Figure B.2** Sublayer detection, step 2: Temporal merging of sections with equal stability class forward in time for 180913. Positive and negative integers as layer names specify stable and non-stable layers, respectively, integer magnitude of layer names shows order of first occurrence of layers in the respective stability classes. For more information see 2.4.

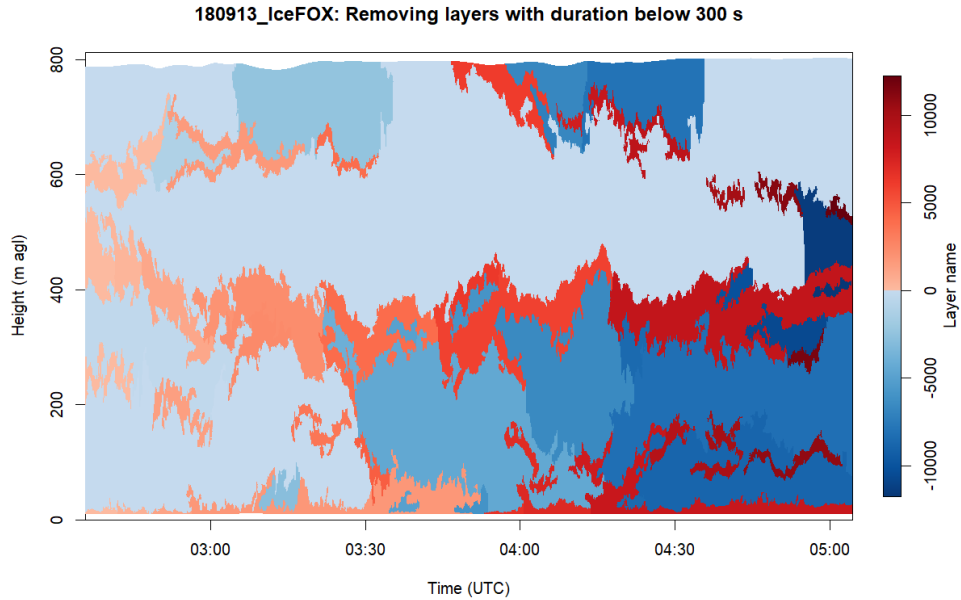


**Figure B.3** Sublayer detection, step 3: Removing layers with duration below 5 min by integrating them in neighboring layers of duration above 5 min, shown for 180913. Positive and negative integers as layer names specify stable and non-stable layers, respectively, integer magnitude of layer names shows order of first occurrence of layers in the respective stability classes. For more information see 2.4.

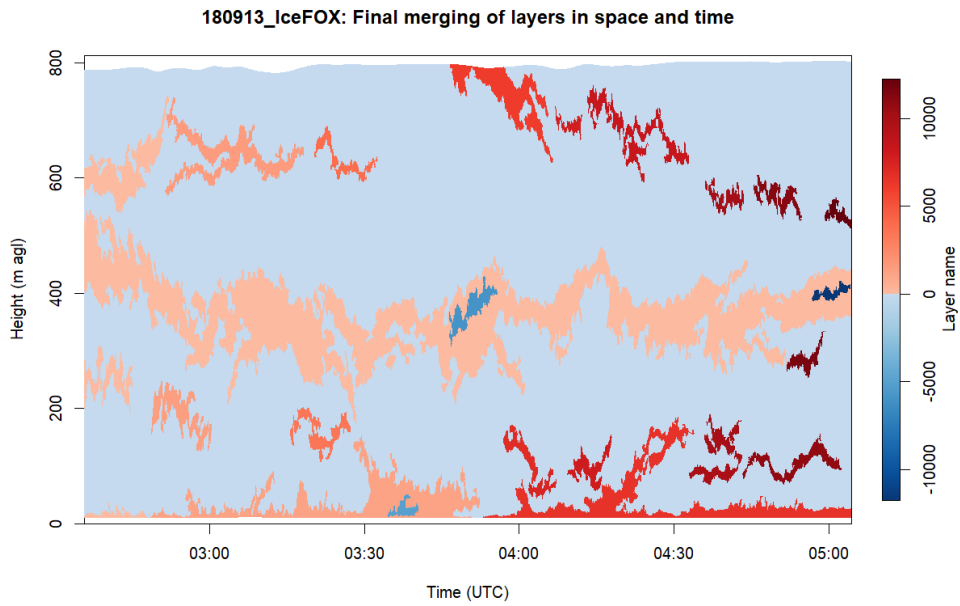


**Figure B.4** Sublayer detection, step 4: Final merging of neighboring layers in same stability class in space and time, shown for 180913. Positive and negative integers as layer names specify stable and non-stable layers, respectively, integer magnitude of layer names shows order of first occurrence of layers in the respective stability classes. For more information see 2.4.

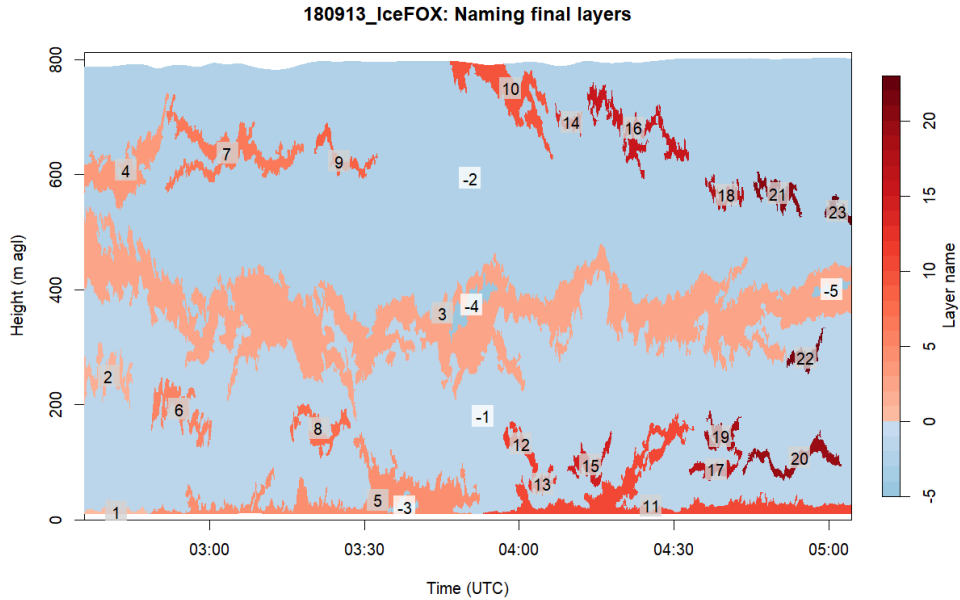


**Figure B.5** Sublayer detection, step 5: Renaming final layers to reduce the magnitude of integers in names, shown for 180913. Positive and negative integers as layer names specify stable and non-stable layers, respectively, integer magnitude of layer names shows order of first occurrence of layers in the respective stability classes. For more information see 2.4.

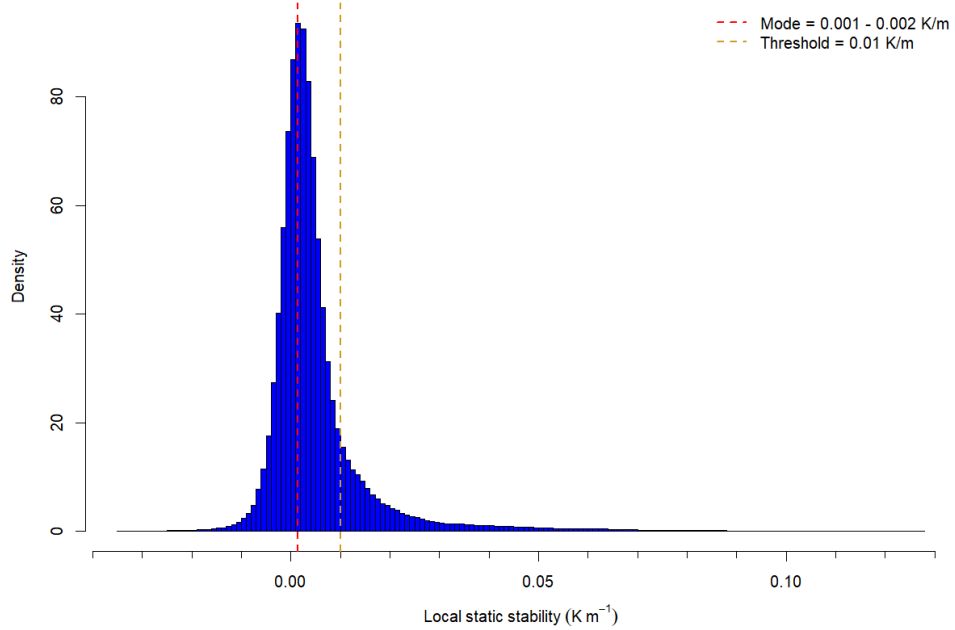


**Figure B.6** Histogram of local static stability for the entire atmospheric profile of 180910, including mode and chosen threshold for distinguishing between non-stable and stable (or temperature inversion) conditions for the layer detection.

### C. Multiresolution decomposition

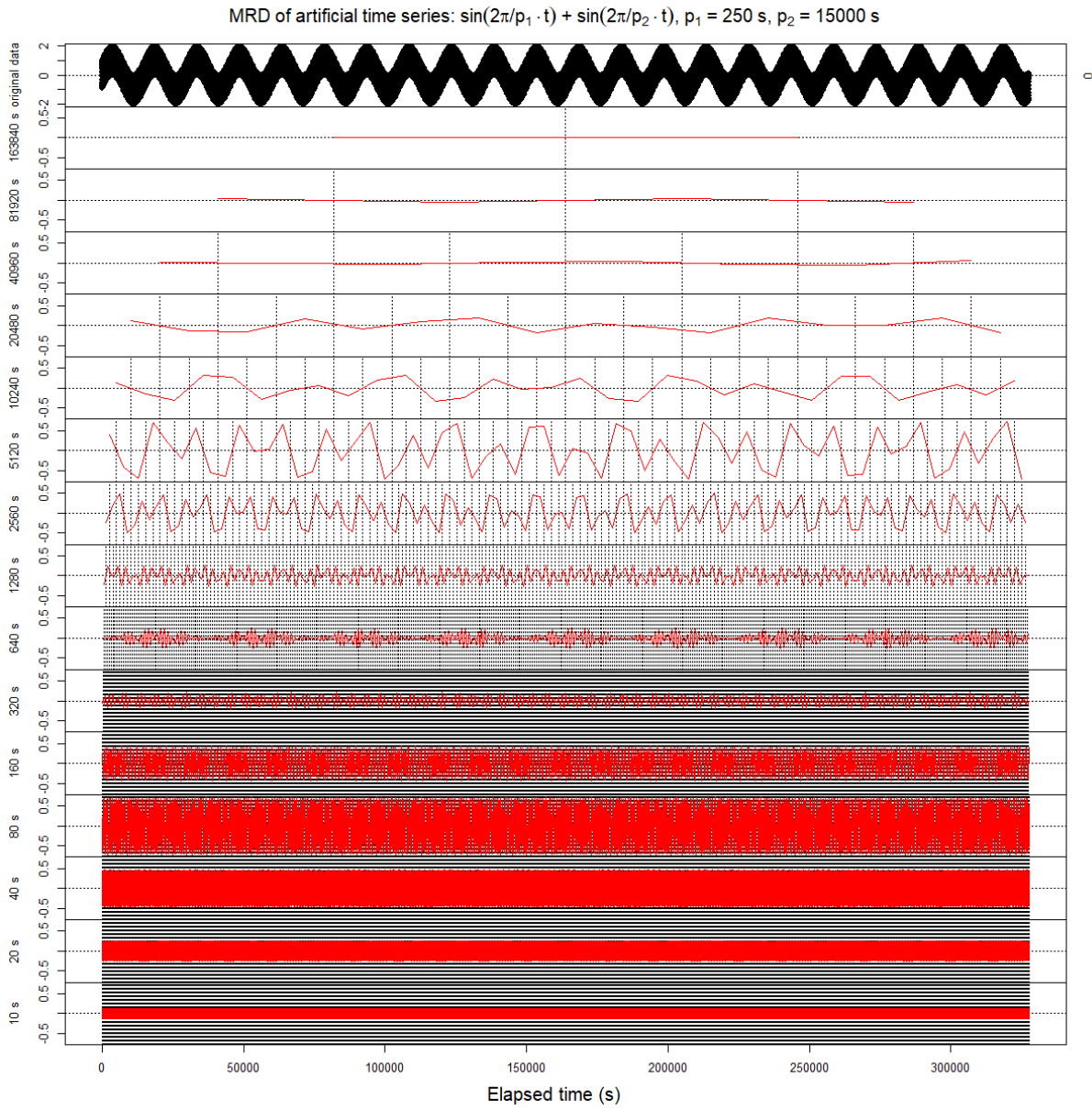


**Figure C.1** Exemplary multiresolution decomposition of an artificial sinusoidal time series. The original series, shown at the top, is decomposed into successive modes with decreasing dyadic length until the original data resolution of 10 s is reached. For more information see 2.5.

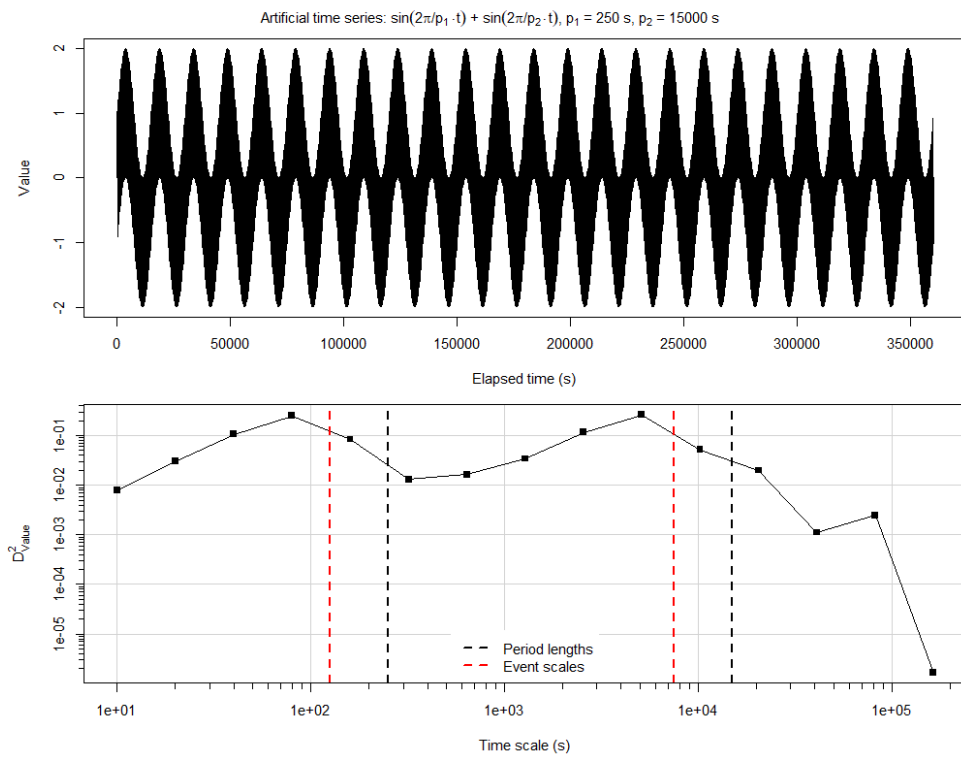


**Figure C.2** Artificial sinusoidal time series and variance spectrum of its multiresolution decomposition (see also Fig. C.1). Time scales of the two peaks in variance ( $D_{value}^2$ ) correspond to event scales (half period lengths) of the respective sine functions defining the time series.

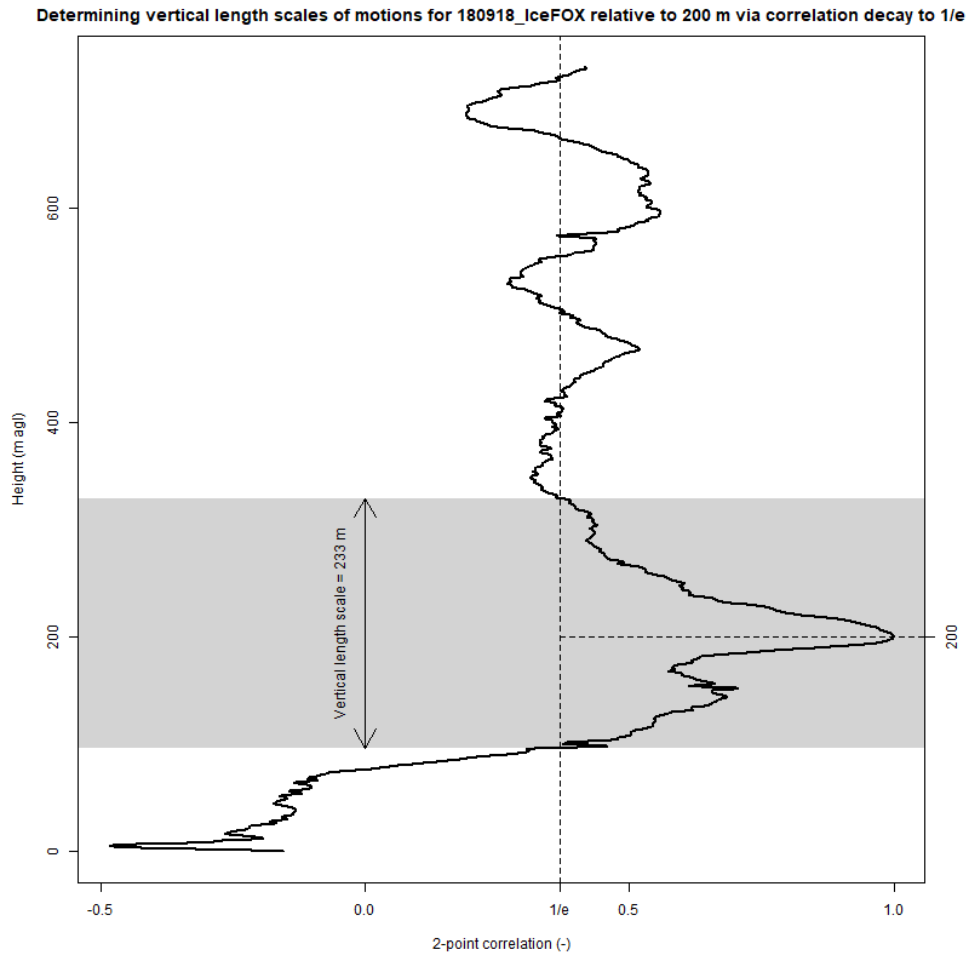


**Figure C.3** Example for the calculation of vertical scales of motions via correlation decay for the largest time scale (640 s) of 180918 at 200 m agl. The upper and lower end of the vertical extent of motions is defined by the first correlation below  $1/e$ , the vertical extent of motions, defined as vertical length scale  $L_v$ , is marked by a gray surface.

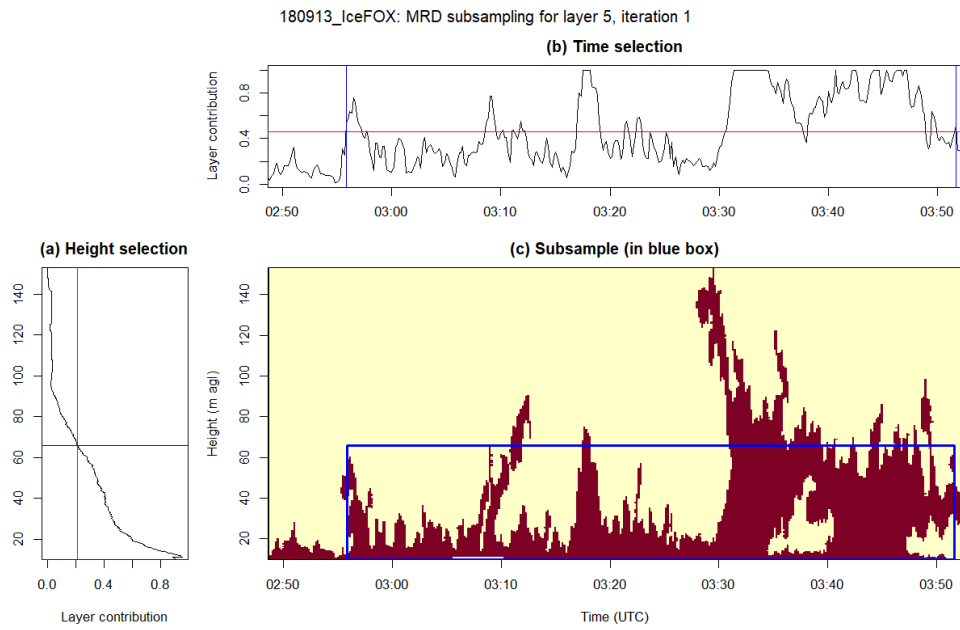


**Figure C.4** Subsampling sublayers for MRD calculation, step 1, shown for inversion layer “5” of 180913. (a) Spatial range with occurrence of layer contributions over time above average (red line) is selected (blue lines). (b) Temporal range with occurrence of layer contributions over space within the spatial subsample above average (red line) is selected (blue lines). (c) Subsample ( $S_{s1,t1}$  in 2.5.3) is defined using the chosen spatial and temporal ranges.

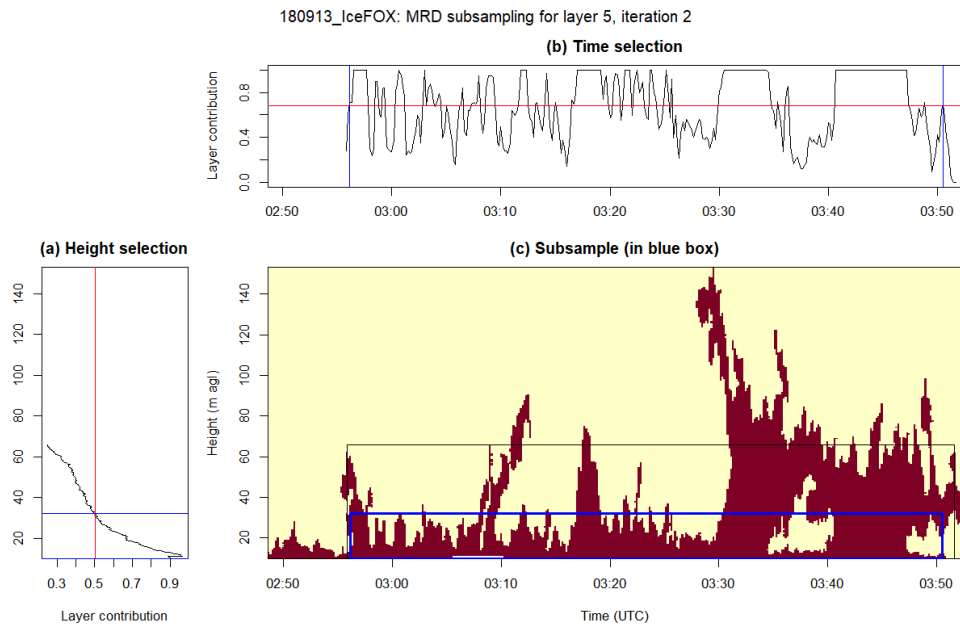


**Figure C.5** Subsampling sublayers for MRD calculation, step 2, shown for inversion layer “5” of 180913. Approach is identical to the one shown in Fig. C.4, except that the output from there is used as initial sample here, making this step a second iteration. Resulting subsample corresponds to  $S_{s2,t2}$  in 2.5.3.

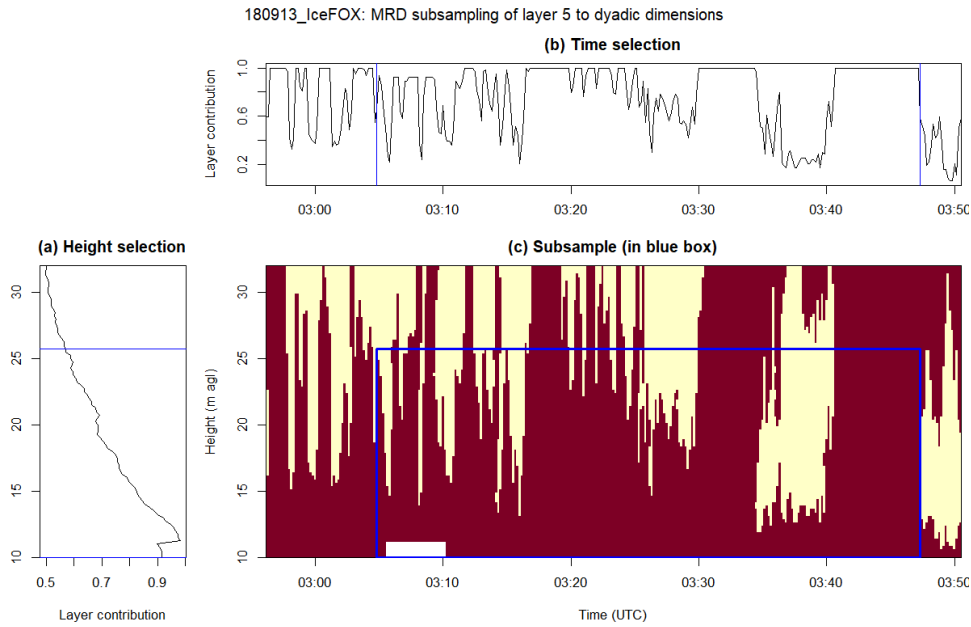


**Figure C.6** Subsampling sublayers for MRD calculation, step 3, shown for inversion layer “5” of 180913. (a) Spatial range with largest fitting dyadic length and maximum layer contribution is selected (blue lines). (b) Temporal range with largest fitting dyadic length and maximum layer contribution within the dyadic spatial subsample is selected (blue lines). (c) Subsample ( $S_{sd,td}$  in 2.5.3) from the input subsample (entire dimensional extent of (c)) is defined using the chosen spatial and temporal ranges.

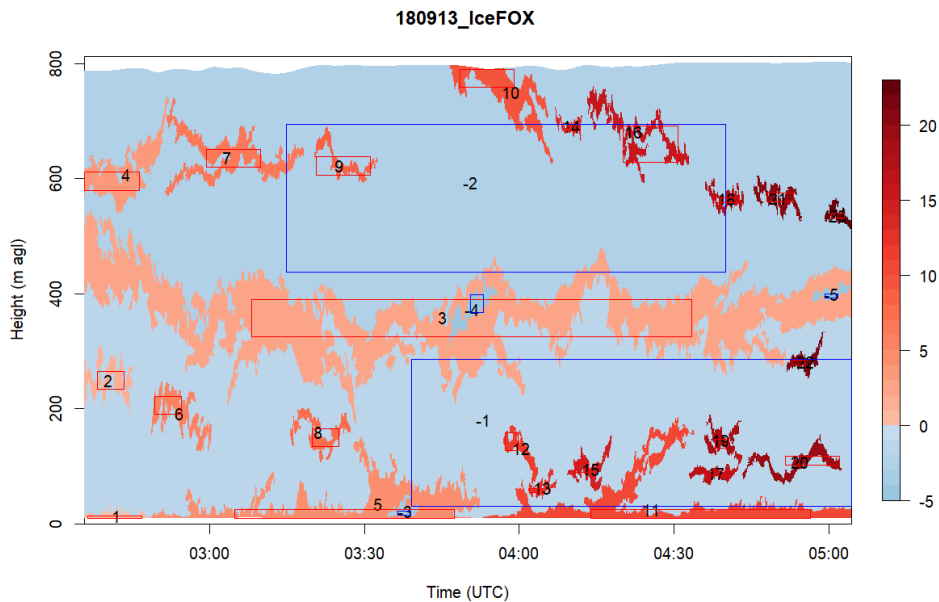


**Figure C.7** Results of the routine for subsampling sublayers for MRD calculation for 180913. Positive and negative integers as sublayer names specify inversion layers and non-inversion layers, respectively, integer magnitude of sublayer names shows order of first occurrence of layers in the respective stability classes. Red and blue rectangles mark final subsamples of inversion layers and non-inversion layers, respectively.

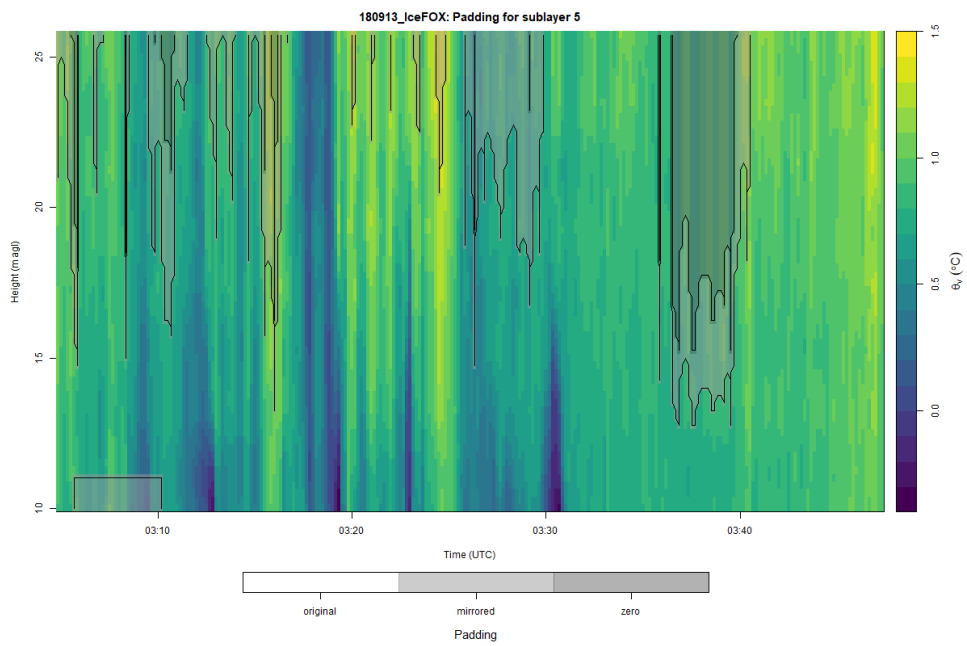


**Figure C.8** Padding approach for MRD in space on sublayers, shown for inversion layer “5” of 180913. Data in the spatiotemporal subsample of the sublayer ( $S_{sd,td}$  in 2.5.3) which were outside the spatial range of the sublayer for a given time step were discarded. Gaps were then filled by linear interpolation in space (only 180916), mirroring data in space and temperature, and finally zero-padding. Note that this padding routine was not used in the results.

## D. Additional results

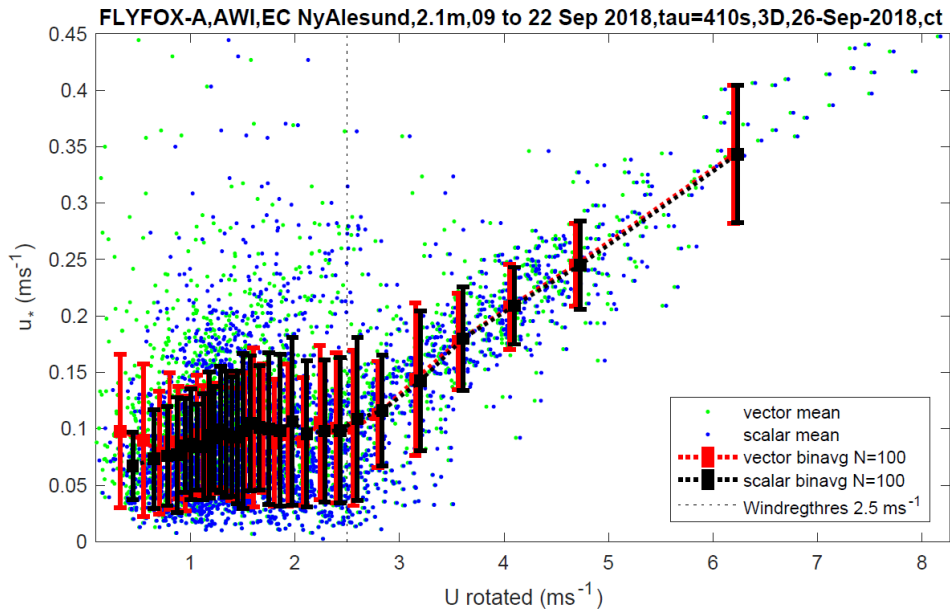


**Figure D.1** Defining strong-wind and weak-wind regimes at 2 m agl following the hockey stick approach by Sun et al. (2012): The relationship between friction velocity  $u_*$  and rotated horizontal wind speed  $U$  becomes linear for  $U > 2.5 \text{ ms}^{-1}$ , marking strong turbulence. This threshold is used to distinguish between weak and strong wind regime.

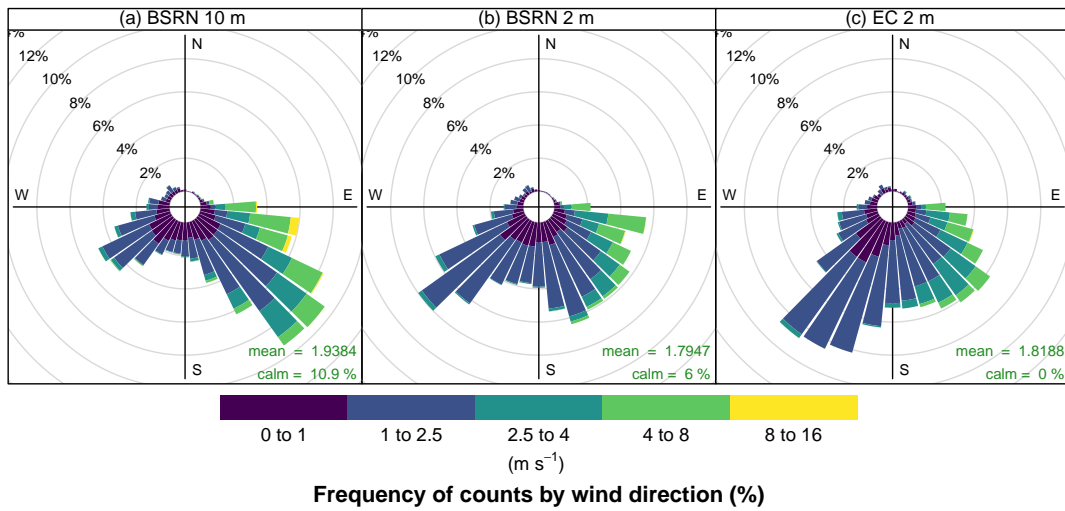


**Figure D.2** Wind roses of surface-based recordings from September 10 to September 21, 2018. (a)-(b) BSRN tower measurements at 10 m agl and 2 m agl, respectively. (c) Ultrasonic anemometer measurements at the Eddy Covariance system.

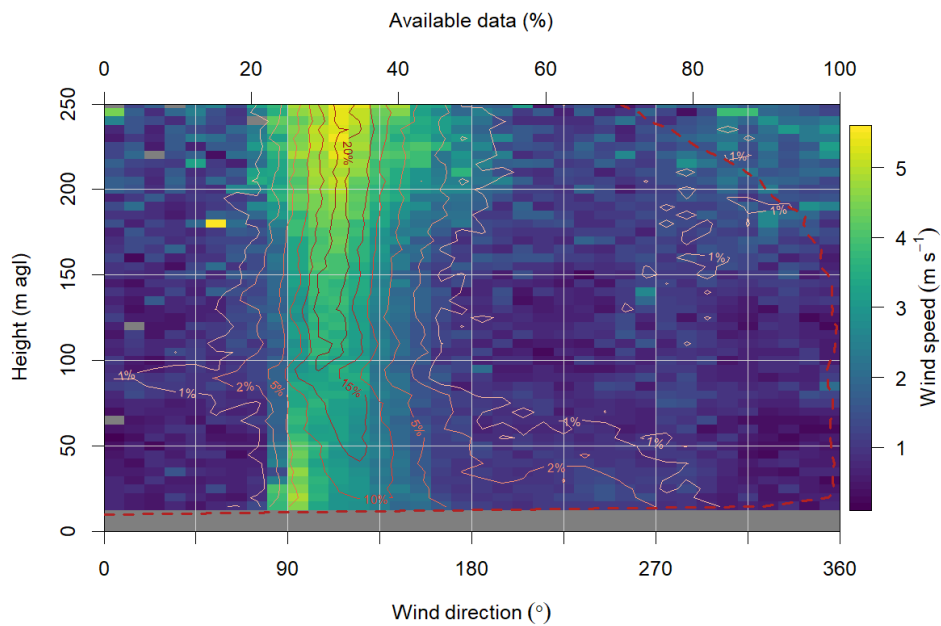


**Figure D.3** Mean horizontal wind speeds depending on wind direction and height, taken from all SODAR recordings between September 12 and September 21. Colored contour lines display probability density of wind directions for individual measurement heights.

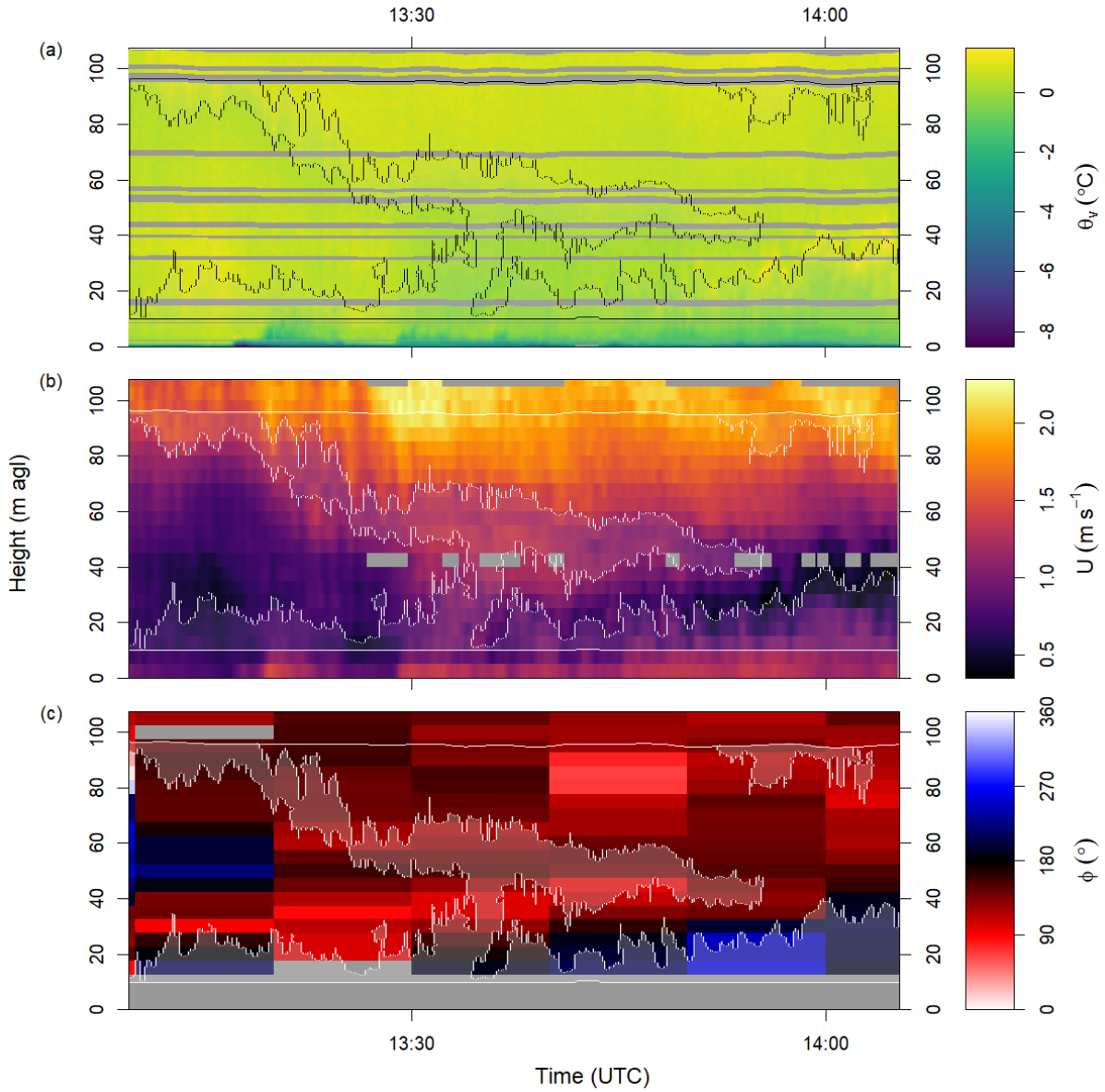


**Figure D.4** Instantaneous atmospheric profiles from the 180916 fiber-optic experiment within the height range of the FireFOX setup; black and white lines indicate borders between inversion layers and non-inversion layers, or the outer border of layer detection; inversion layers are overlain with light gray. (a) Virtual potential temperatures  $\theta_v$  from fiber-optic recordings. (b) Wind speed  $U$  from fiber-optic measurements, averaged to spatial resolution of 5 m. (c) Wind direction  $\phi$  recorded with SODAR.

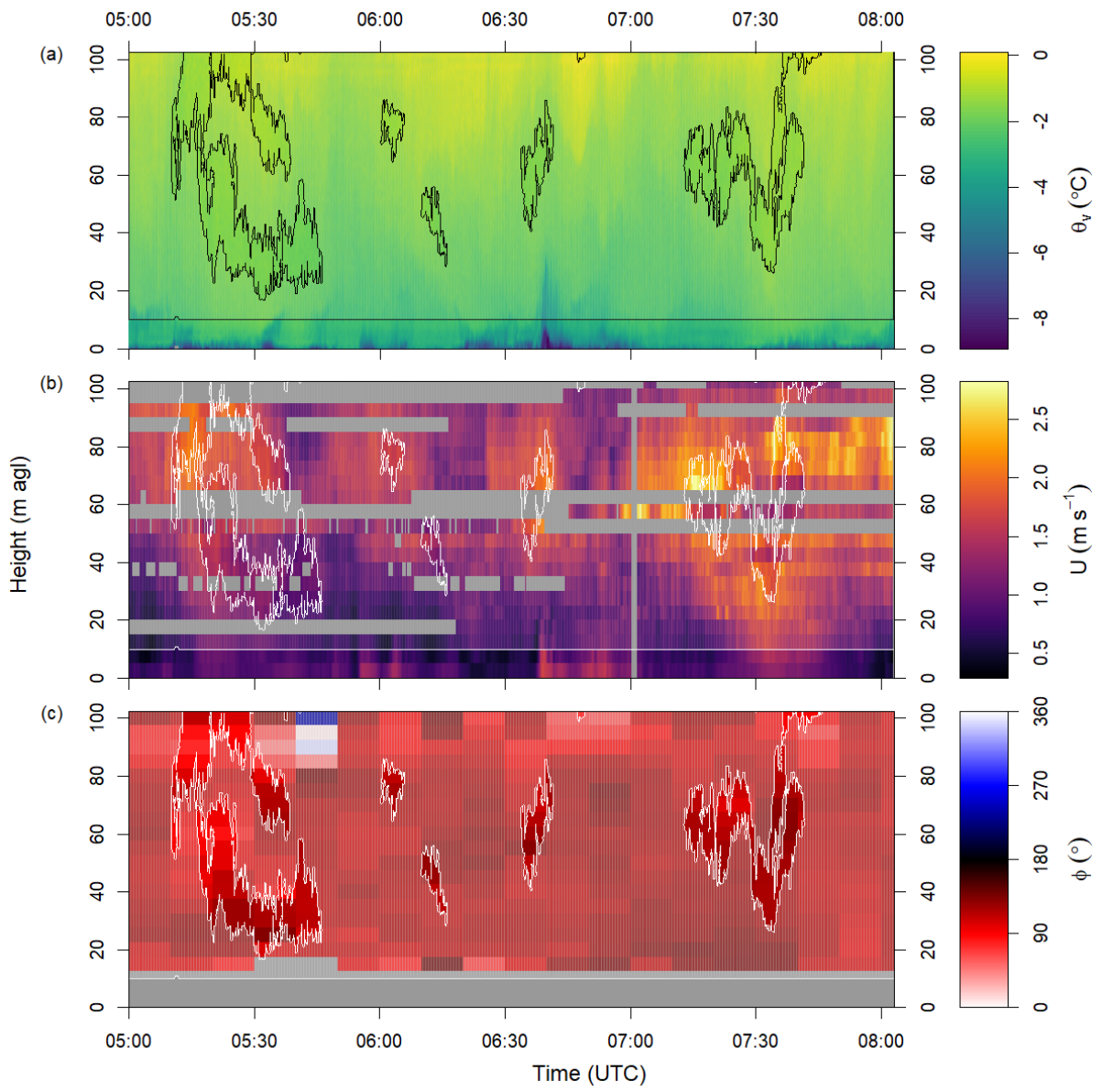


**Figure D.5** Same as Fig. D.4, but for the 180918 experiment.

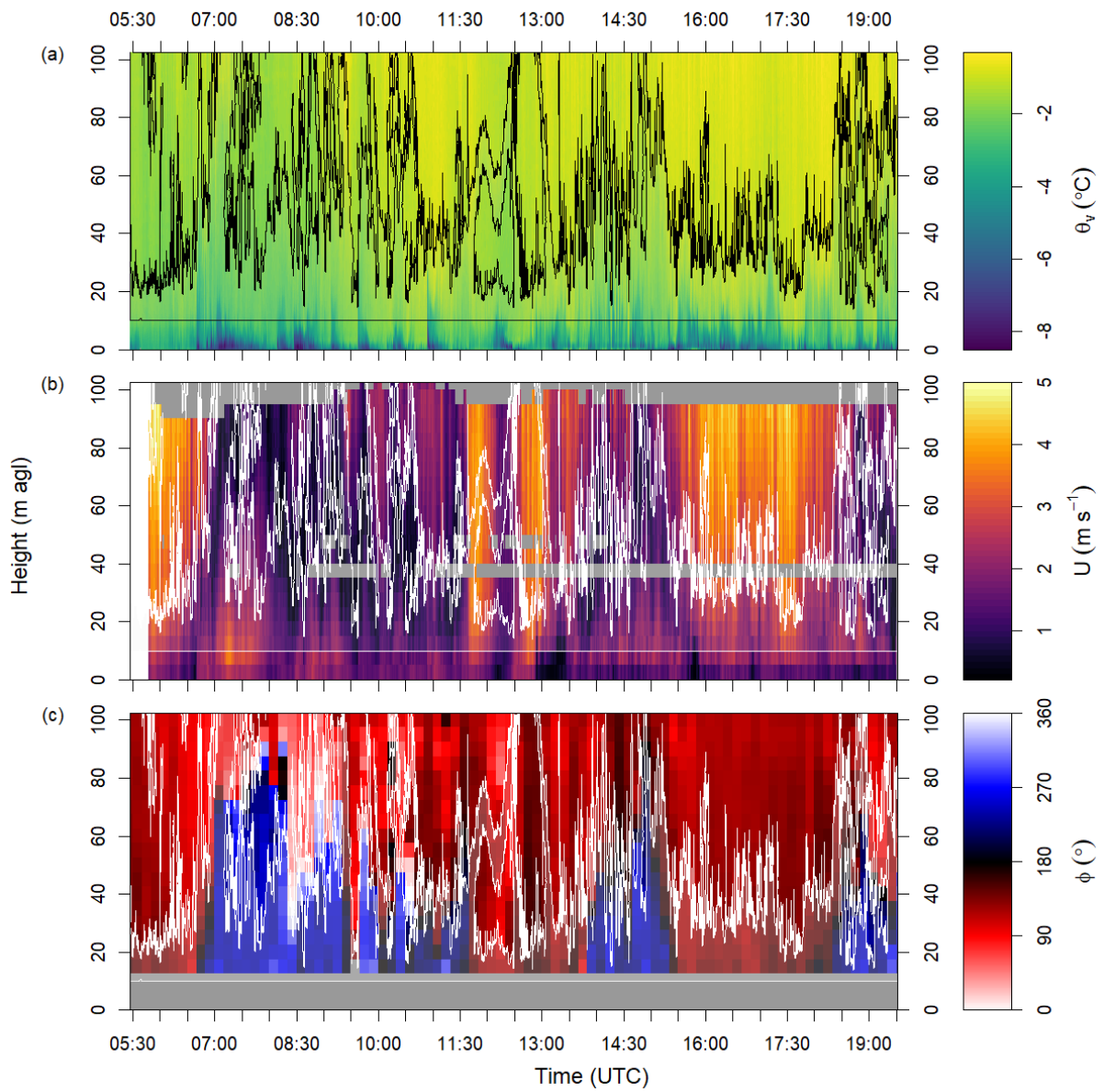
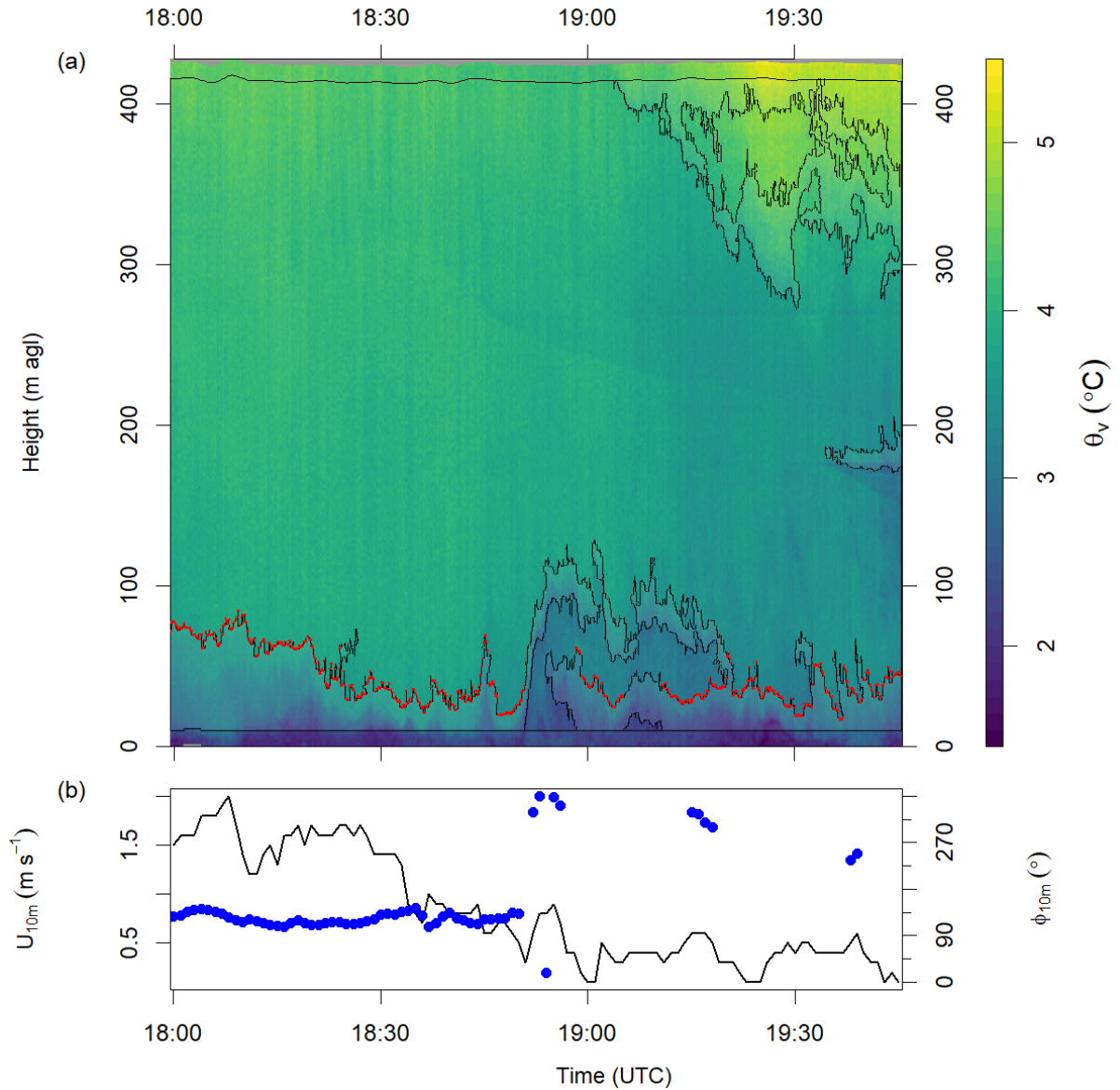


Figure D.6 Same as Fig. D.4, but for the 180921 experiment.



**Figure D.7** Instantaneous atmospheric profiles from the 180910 fiber-optic experiment. (a) Virtual potential temperatures  $\theta_v$  from fiber-optic recordings; black lines indicate borders between inversion layers and non-inversion layers, or the outer border of layer detection; inversion layers are overlain with light gray; red dots signify estimated surface-based inversion height. (b) Wind speed  $U_{10m}$  (lines) and direction  $\phi_{10m}$  (dots) at 10 m agl on the BSRN tower.

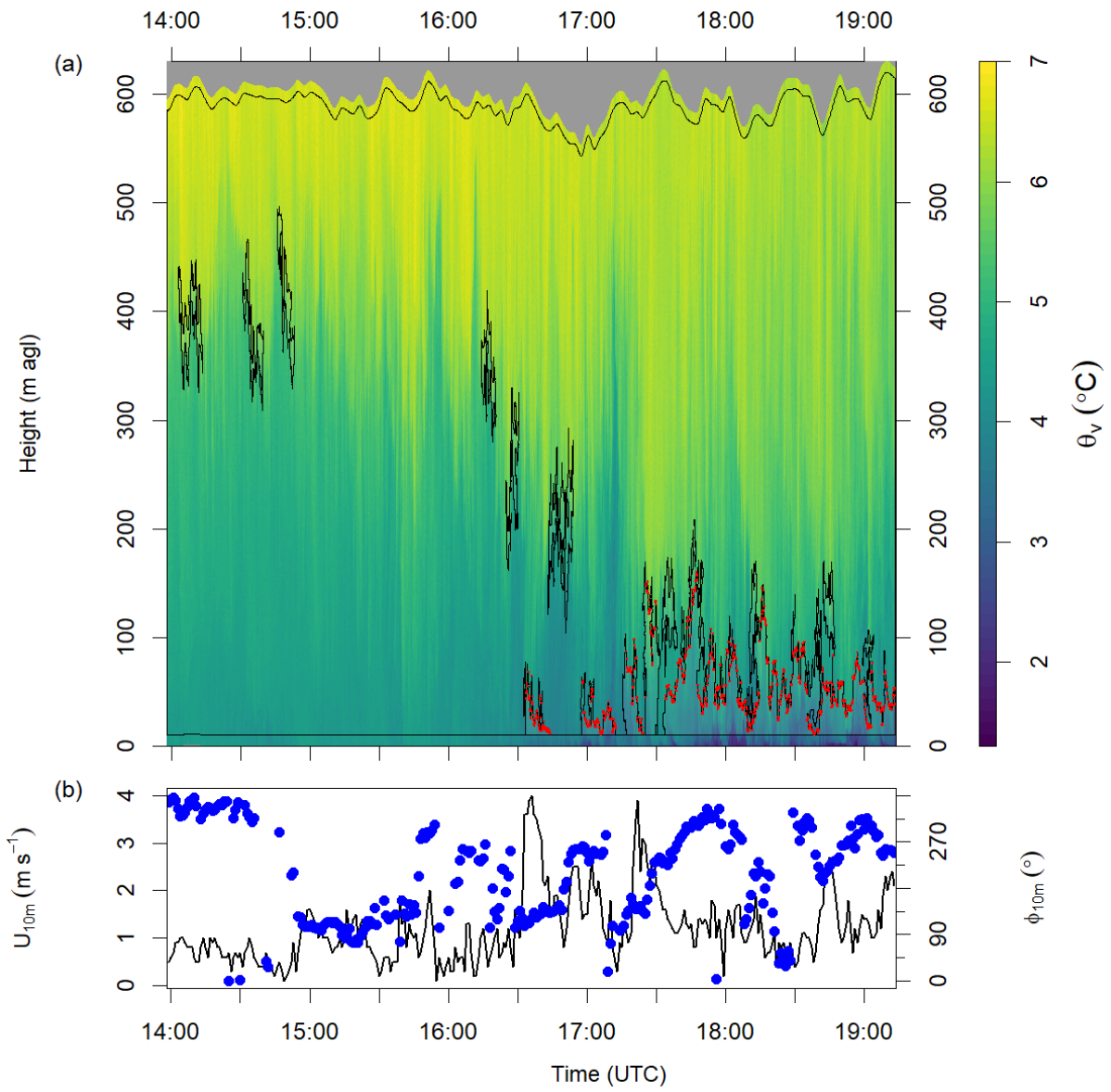
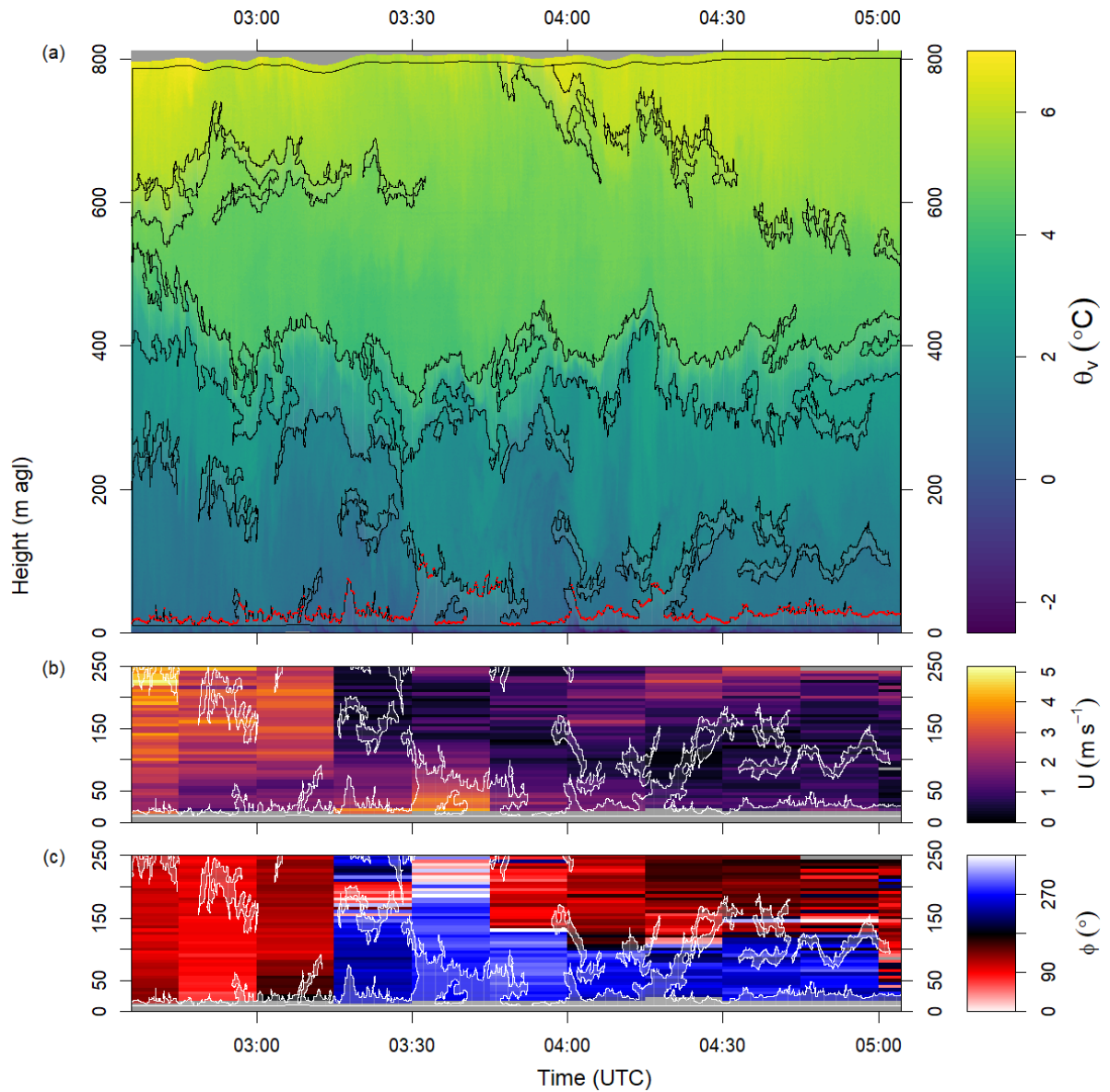


Figure D.8 Same as Fig. D.7, but for the 180911 experiment.



**Figure D.9** Instantaneous atmospheric profiles from the 180913 fiber-optic experiment; black or white lines indicate borders between inversion layers and non-inversion layers, or the outer border of layer detection; inversion layers are overlain with light gray. (a) Virtual potential temperatures  $\theta_v$  from fiber-optic recordings; red dots signify estimated surface-based inversion height. (b) Wind speed  $U$  and (c) direction  $\phi$  recorded with SODAR.

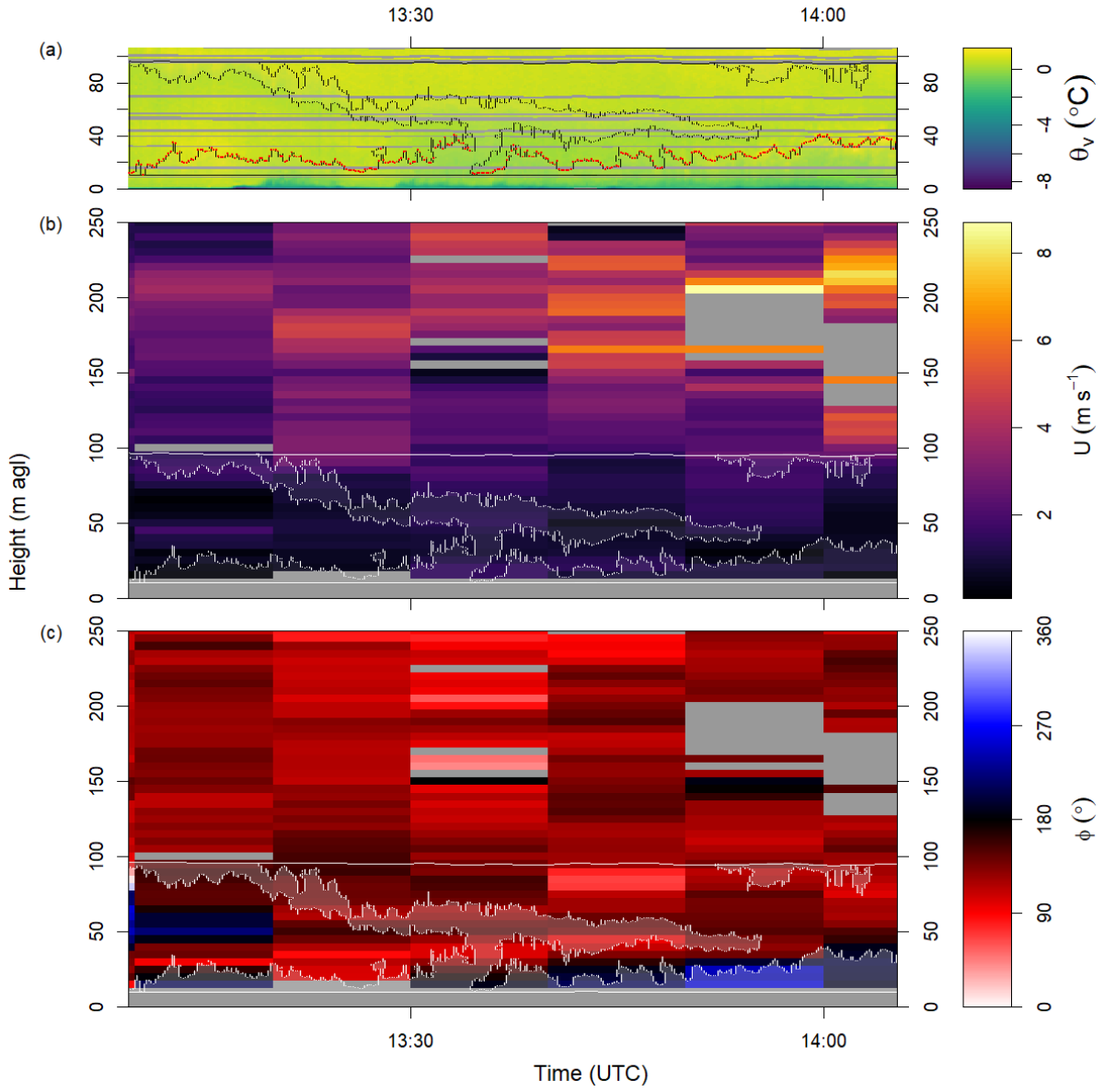
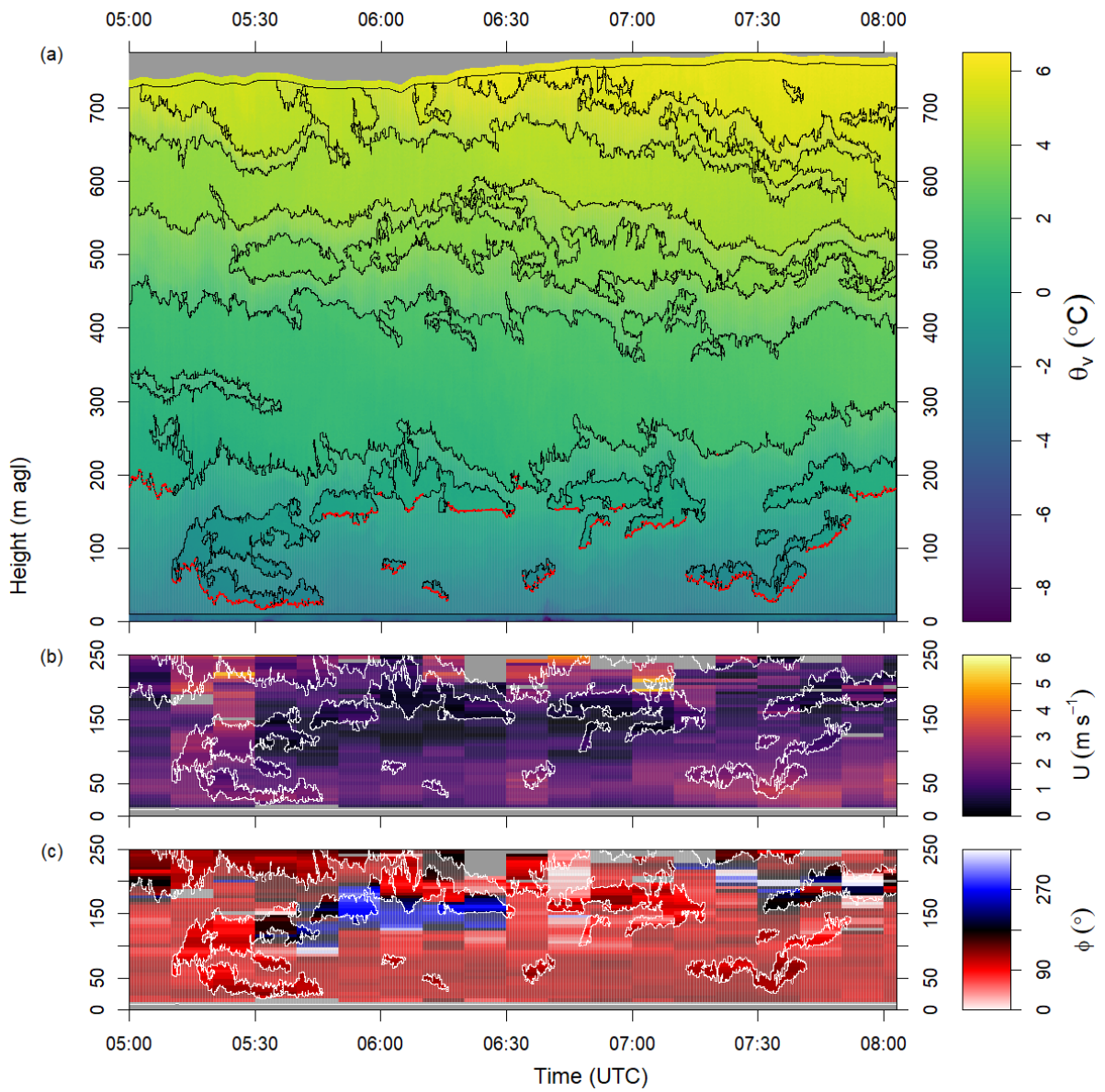


Figure D.10 Same as Fig. D.9, but for the 180916 experiment.



**Figure D.11** Same as Fig. D.9, but for the 180918 experiment.

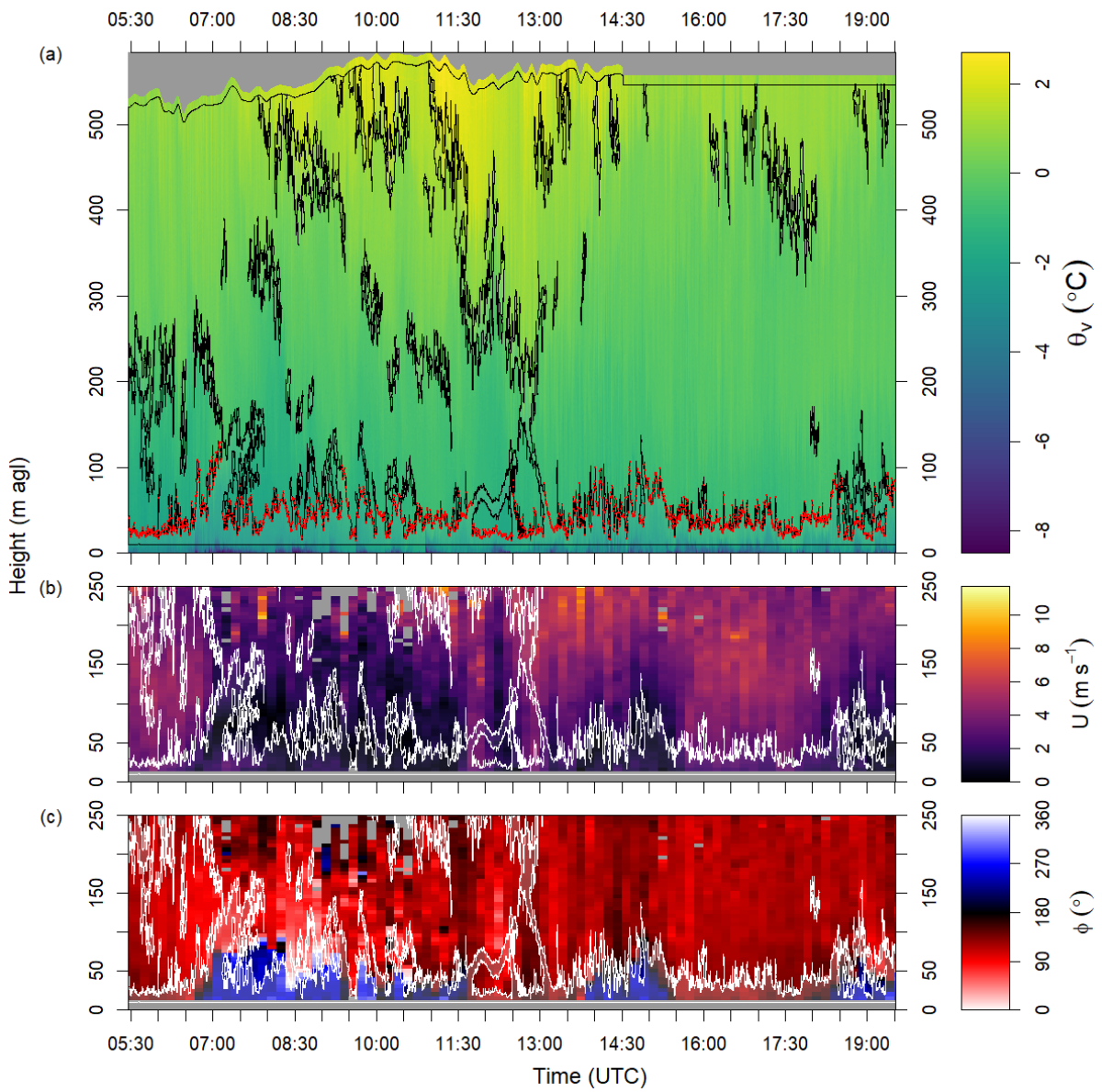
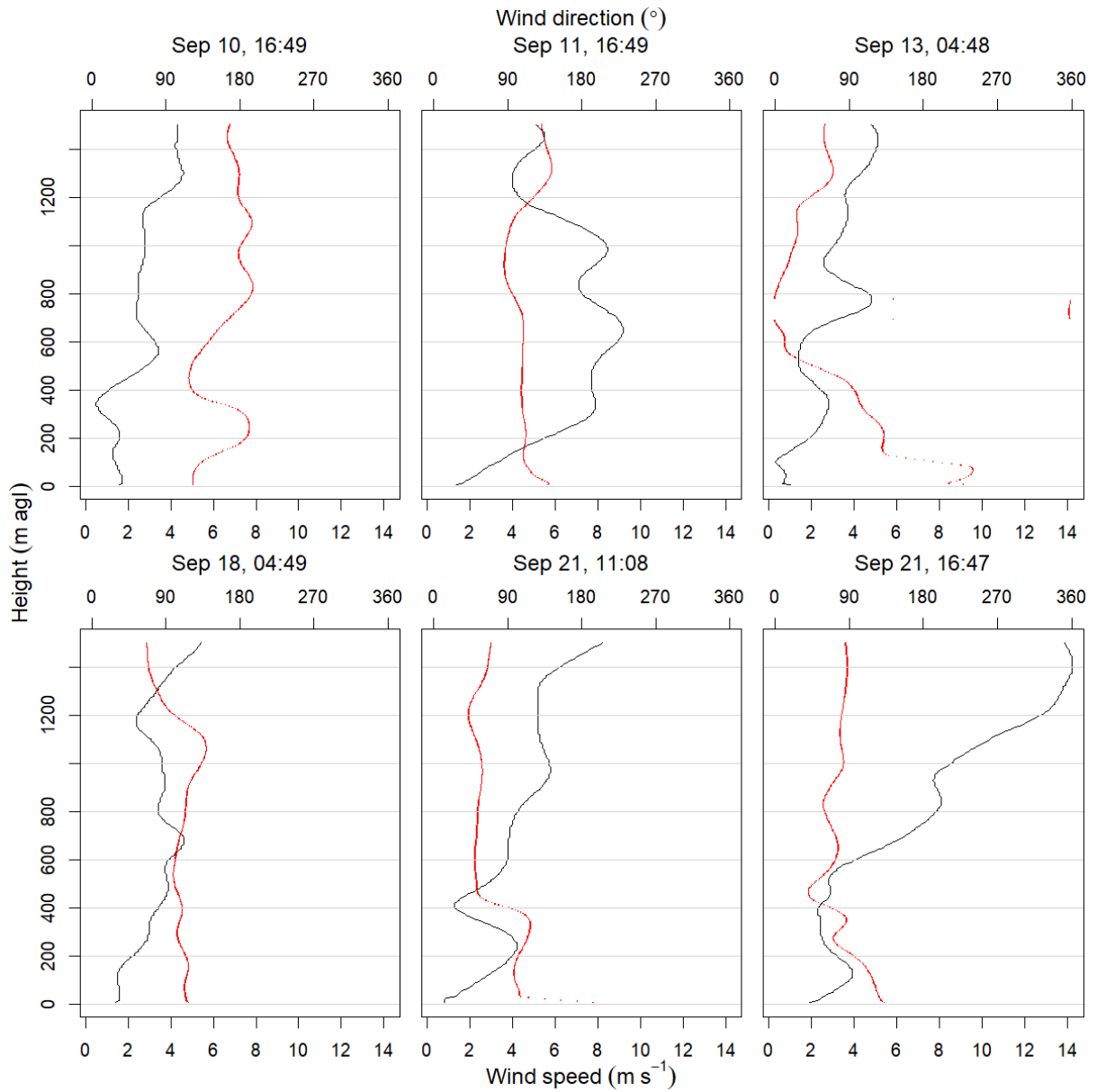


Figure D.12 Same as Fig. D.9, but for the 180921 experiment.



**Figure D.13** Selected wind profiles from radiosoundings during or shortly previous to fiber-optic experiments, with launch time of radiosondes given in UTC. Black lines and red dots show wind speed and wind direction, respectively.

## Declaration of Authorship

I hereby declare that writing the master thesis

*“Vertical structure of the lower polar troposphere observed in temperature and wind profiles from fiber-optic distributed sensing on a tethered balloon over Ny-Ålesund, Svalbard, the Arctic”*

has been my own independent and unaided effort. All direct and indirect sources and resources that I used for this thesis are indicated as references. The thesis has never been submitted for the achievement of an academical degree, nor published in any other way.

Bayreuth, February 24, 2021

---

Tobias Linhardt